University of Naples “Federico II”

DOCTOR OF PHILOSOPHY
IN
PHYSICS

Cycle: XXX
Coordinator: Prof. Salvatore Capozziello

BINARY AND TERNARY QUASIFISSION INDUCED BY SHELL EFFECTS AT NEAR BARRIER ENERGY IN HEAVY NUCLEAR SYSTEMS

Scientific Sector: FIS / 04

Candidate
Md Ashaduzzaman

Supervisor
Prof. Emanuele Vardaci

Years: 2014-2017
Department of Physics “Ettore Pancini”, Naples, Italy

UNIVERSITY OF NAPLES “FEDERICO II”
DEPARTMENT OF PHYSICS “ETTORE PANCINI”

The undersigned hereby certifies that he has read and recommend to the program of Physics for acceptance a thesis entitled “**Binary and ternary quasifission induced by shell effects at near barrier energy in heavy nuclear systems**” by **Md Ashaduzzaman** in fulfillment of the requirements for the degree of **Doctor of Philosophy**.

Dated: **31 October 2017**

Research Supervisor: ______________________________
Professor Emanuele Vardaci

UNIVERSITY OF NAPLES “FEDERICO II”

Date: **31 October 2017**

Author: **`Md Ashaduzzaman`**
Title: **Binary and ternary quasifission induced by shell effects at near barrier energy in heavy nuclear systems**
Department: **Department of Physics “Ettore Pancini”**
Degree: **Ph.D.**

Signature of Author

To my daughter, my angel, my princess

Aisha Binte Ashad

Contents

List of Tables viii

List of Figures x

Acknowledgements xv

List of Symbols xvii

List of Acronyms xviii

Abstract xx

Introduction 1

1 Nuclear Fission 4
- 1.1 Introduction 4
- 1.2 Evidence of TTF 6
  - 1.2.1 Energy Balance in TTF 10
  - 1.2.2 Barrier Height 11
- 1.3 Role of Potential Energy Surface 13
  - 1.3.1 Ternary Quasifission of heavy nuclear systems 15
- 1.4 Purpose of the thesis 26
  - 1.4.1 Observables and detection geometry 28
- 1.5 Outline of the thesis 34

2 Experimental Setup and DAQ system 36
- 2.1 Introduction 36
- 2.2 Detectors 38
  - 2.2.1 TOF Arm 38
  - 2.2.2 ΔE - E Telescopes 42
  - 2.2.3 Monitor Detectors 43

2.3 Signal Processing and Data Acquisition System 44
  2.3.1 Electronic Chain for CORSET 44
  2.3.2 Electronic Chain for ΔE - E Telescopes and Monitors . . 47
  2.3.3 Trigger for Acquisition System 48

3 Data Analysis **50**
3.1 Detector Calibration 50
  3.1.1 Flight Path Measurements 51
  3.1.2 Time-of-Flight (TOF) Measurements 52
  3.1.3 ΔE - E of Telescopes 55
3.2 Velocity Calculations 58
3.3 Mass-Energy Calculations 58
  3.3.1 Binary Reaction: Mass-TKE 58
  3.3.2 Ternary Reaction: Mass-TKE 59
3.4 Energy Loss Corrections 60

4 Experimental Results **62**
4.1 Binary Fission (Coincidences Arm0 - Arm3): velocity, mass and TKE distributions 63
4.2 Ternary Fission (Coincidences in Arm1 - Arm2): velocity distributions . . . 68
  4.2.1 Three body channel: velocity plots 70
  4.2.2 Three body channel: $^{40}Ar + {}^{208}Pb$ system 71
  4.2.3 Three body channel: $^{37}Cl + {}^{208}Pb$ and $^{40}Ar + {}^{205}Tl$ systems . . . 72
4.3 Data from ΔE-E telescopes 74
4.4 Closing remarks 76

Conclusions and Perspectives **78**

A Direct Ternary Fission **79**

B Features of the Setup **81**
B.1 CORSET arms 81
B.2 Telescopes 83
B.3 Monitors 83

C Calibration Parameter **85**
C.1 Position Calibration: 85
C.2 Time-of-Flight Calibration: 85
C.3 Energy Calibration: 88

D Potential Energy Calculation: Three Cluster Model **89**

E Mass Distributions of Ternary Fission **94**

F Sequential Ternary Fission **96**

Bibliography **104**

Scientific activities and products during the PhD training **115**

List of Tables

1.1 Major features of some TTF reaction channels. 27

1.2 Major entrance channel features of the reactions. 28

2.1 CORSET Parameters connected to TDC. 46

2.2 Telescopes and Monitors connected with ADC. 48

3.1 Main parameters used to calculate fight paths. 52

3.2 Parameters of elastic scattered Cl and Pb in Arm0. 55

4.1 Measurements run during the experiment. 62

4.2 Table of the tripartitions accessed by the system $^{40}Ar + {}^{208}Pb$ at 193 and 230 MeV. The expected energy of the third (heaviest) fragment is also given for the lab angle $\theta_{lab} = 154.5°$. 74

4.3 Table of the tripartitions accessed by the systems $^{37}Cl + {}^{208}Pb$ and $^{40}Ar + {}^{205}Tl$. The expected energy of the third (heaviest) fragment is also given for the angle $\theta_{lab} = 154.5°$. 75

4.4 Ratio between Ternary and Binary events for each reaction. 77

B.1 Main parameters of four CORSET arms. 82

B.2 Major features of the E - ΔE Telescopes. 84

B.3 Major features of the Monitor Detectors. 84

C.1 Position Calibration points of CORSET arms for *Cl+Pb* reaction. 86

C.2 Position Calibration points of CORSET arms for *Ar+Tl* reaction. 86

C.3 Position Calibration points of CORSET arms for *Ar+Pb* reaction. 87

C.4 Position calibration parameters of four CORSET arms. 87
C.5 TOF calibration parameters of CORSET arms for three reactions. 88
C.6 Calibration points for E detector. 88
C.7 Calibration points for ΔE detector. 88
C.8 Calibration parameters for E and ΔE detectors. 88

D.1 Ternary fragmentation potential between the three fragments decaying in collinear and triangular (equatorial) configuration for ^{245}Es and ^{248}Fm nuclei. 91

List of Figures

1.1 Schematic representation of ternary fission processes. 5

1.2 (Color online) Contour maps (in logarithmic scale, the steps between colors are approximately a factor 2.5) of the mass-mass distribution of the collinear fragments, detected in coincidence in the two opposite arms of the FOBOS spectrometer (from [10]). 6

1.3 (a) Fragments kinetic energy distribution and (b) Light-mass fragment distribution from TTF and BF (from [23, 26]). 8

1.4 Decay energy of an ideal, electrically charged liquid drop as a function of fissionability parameter χ and of the value of Z^2/A (from [45]). 10

1.5 Barrier heights (in units of MeV) for the fission of nuclei along the β stability valley as a function of temperature and mass number (from [52]). 12

1.6 (a) Driving potential for the nuclear system formed in $^{48}Ca+^{248}Cm$ collision (from [53]). The solid lines with arrows show schematically (without fluctuations) the quasi-fission trajectories going to the lead and tin valleys. The dashed curves correspond to fusion (CN formation) and fission processes. (b) Mass-TKE distribution of reaction fragments in collision of ^{48}Ca with ^{248}Cm at 203 MeV center-of-mass energy (from [66]). 13

1.7 Potential energy surface as a function of charge number of ternary fission of ^{252}Cf (from [60]). 14

1.8 Landscape of the potential energy surface for three-body clusterization of ^{248}Cm (from [53]). 16

1.9 Landscape of potential energy of three body configurations formed in collision of $^{238}U +^{238} U$ (from [63]). 16

1.10 Mass-TKE distributions of fragments at energies above the Coulomb barrier. From left to right the entrance channel mass asymmetry decreases, and the Coulomb factor Z_1Z_2 increases. Solid curves in the average TKE and its variance are the expectation for CNF (from [69]). 20

1.11 Mass-TKE of the correlated fission fragments from the reactions ^{12}C + ^{204}Pb (left panels) and ^{48}Ca + ^{168}Er (right panels) as a function of fragment mass M: a) and c) show the two-dimensional matrices (M,TKE); b) and d) show the integrated mass distributions. Solid curves are Gaussian fits to the symmetric (central) components and open circles (right-hand panel only) correspond to the extracted asymmetric contribution (from [86]). 21

1.12 Potential energy as function of mass asymmetry and elongation of composite system ^{216}Ra (from [87]). 22

1.13 Top: Mass-TKE distributions for the reactions ^{36}S, ^{48}Ca, ^{64}Ni + ^{238}U at energies close to the Coulomb barrier; bottom: open circles are mass distributions for fission-like fragments inside the contour line on Mass-TKE matrices and solid lines are the driving potentials as a function of mass (from [90]). 24

1.14 Mass distributions for fission-like fragments formed in the reactions ^{26}Mg + ^{248}Cm and ^{36}S + ^{238}U at energy below the Coulomb barrier. Red curves are fusion fission components estimated from TKE analysis, blue curves are QF components (from [92]). 25

1.15 Two body kinematics plot for symmetric fission: (a) for composite system ^{245}Es produced by first two reactions and (b) for composite system ^{248}Fm produced by third reactions. 29

1.16 Proposed detection geometry for the binary decay. 29

1.17 Three body kinematics plot of three body decay of interest for $^{37}Cl + ^{208}Pb \rightarrow$ ^{132}Sn + ^{65}Cu + ^{48}Ca case. 30

1.18 Proposed detection geometry for the ternary decay. 30

1.19 Angular correlation of three (^{132}Sn, ^{65}Cu, $and^{48}Ca$) fragments in terms of ^{48}Ca energy. 31
1.20 Possible double kinematics energy solution for ^{132}Sn and ^{65}Cu for a fixed energy of ^{48}Ca. The angles are refereed to the lab reference frame. 32
1.21 Velocity diagram for a 3-body sequential fission. 33
1.22 Angular correlations for a specific 3-body sequential fission. 33

2.1 Complete experimental setup inside scattering chamber. 37
2.2 Layout of the experimental setup. 38
2.3 A CORSET arm consists of a Start and a Stop detectors. 39
2.4 Picture and schematic diagram of the start detector with an electrostatic mirror. 40
2.5 Schematic diagram of the MCP-based position-sensitive stop detector. . . . 41
2.6 Six E - ΔE Telescopes used in the backward beam direction. 43
2.7 Three monitor detectors placed in front of the setup. 43
2.8 Block Diagram of the CORSET. 45
2.9 Block Diagram of the E - ΔE Telescopes and Monitors. 47
2.10 Block Diagram of the trigger logic. 48

3.1 Position of the calibration points on the foil layer of MCP. 50
3.2 schematic diagram of the MCP of stop detector when fragment hits at point P. 51
3.3 Schematic representation of TAC connected with time calibrator. 53
3.4 Peaks for TOF_0 from elastic scattering between Cl + Pb in Arm0. 54
3.5 The decay series of ^{226}Ra (from [108]). 55
3.6 Alpha energy raw spectra: (a) for E detector and (b) for ΔE detector. 56
3.7 E-ΔE matrix of raw data from alpha source. 57
3.8 Alpha energy calibrated spectra: (a) for E detector and (b) for ΔE detector. . 57
3.9 E-ΔE matrix of calibrated data from alpha source. 58

4.1 An example of a reconstructed 2D velocity plot for coincidences in Arm0 and Arm3. 63

4.2 Mass-TKE distributions for the binary products measured in full momentum transfer in all reactions under study. Only events within the limits $0.90 < V_{||}/V_{c.m.} < 1.1$ and 0.90 cm/ns $< V_{\perp} < 1.1$ cm/ns are considered. See text for details. 64
4.3 Velocity diagrams: (a) for binary events with full momentum transfer; (b) and (c) for the case of sequential fission of TLF (from [109]). 65
4.4 $V_{\perp}$ vs. $V_{||}/V_{c.m.}$ distributions for all reactions. 65
4.5 Mass distributions for all reactions. 66
4.6 TKE distribution for all the reaction studied. The solid lines show the prediction from Viola systematics. The maximum values are normalized to the experimental values which are slightly different because of the energy resolution of the spectrometer. 67
4.7 2D velocity plot for coincidences between Arm1 and Arm2. V_A is the velocity in one arm and V_B in the other arm. 68
4.8 $V_{\perp}$ vs. $V_{||}/V_{c.m.}$ distributions for all reactions for coincidences between Arm1 and Arm2. 69
4.9 Velocity distributions for all reactions for coincidences between Arm1 and Arm2. The lines are the kinematics loci occupied by the selected tripartions in case of a TTF. 70
4.10 Velocity distributions for the reactions $^{40}Ar + {}^{208}Pb$ along with kinematics calculations for selected tripartitions. 71
4.11 Velocity distributions for the reactions $^{37}Cl + {}^{208}Pb$ (top row) and $^{40}Ar + {}^{205}Tl$ at 195 MeV along with kinematics calculations for selected tripartitions. . . 73
4.12 Energy spectra of the fragments stopping in the ΔE telescope at $\theta_{lab} = 154.5°$. 75

B.1 Angle coverage in terms of beam direction on the stop detector from the target. 82
B.2 Flight path of the fragments on the stop detector. 83

D.1 Potential energy surface as a function of charge number of ternary fission of ^{242}Cf for two different arrangements. 92

D.2 (Color online) The total ternary fragmentation potential as a function of the orientation angle is presented for three different fragment combinations in three different arrangements for the angular momentum $l = 0\hbar$ and $40\hbar$. . . 93

F.1 Initial two body decay in the laboratory and centre of mass frame of reference. 96
F.2 Simplified initial two body decay in the laboratory and centre of mass frame of reference. 99
F.3 Kinematics plot for 3 body sequential fission. 100
F.4 Simplified centre of mass frame of reference of final interacting system for 2nd fragment. 101
F.5 Simplified centre of mass frame of reference of final interacting system for 3rd fragment. 102

Acknowledgements

*First and foremost, all the praises to almighty **ALLAH**, who gave me opportunity for higher study and to reach at the final step of my PhD program.*

*Then, my heartiest thanks, gratitude, and acknowledgments are for my honorable supervisor **Professor Emanuele Vardaci**. I thank him for his continuous support, patience, and motivations during my Ph.D study and research. He worked hard and showed great patience to help me to finalize the thesis. Moreover, his enthusiasm and immense knowledge encouraged me to learn how to do research. He always motivated me and suggested to try again and again to overcome the situation whenever I would have been stuck up in a point. In the course of my PhD journey, he helped me to get many chances to visit different well known laboratories in different countries and to acquire valuable knowledge for experimental works. To me, he is not only a supervisor but also like a father since he always stood beside me in all my personal and family problems. Above all, I am very much grateful for his immense help in solving my financial problems at the very beginning of my stay in Italy.*

*After that, I must express my deepest thanks and appreciation for my two dear colleagues, **Daniele Quero** and **Alessandro Pulcini**, for their kind endless help. I am extremely grateful for their assistance in the preparation of JYFL Experiment and in data analysis. In fact, my thesis work would not have been successfully done without their selfless helps. I always found them very cordial at any difficulty. My special thanks goes to Daniele Quero for his continuous support in the data analysis. I would like to acknowledge my other colleague, **Dr. Prasanta Kumar Rath** for his continuous support and for being ready to help me at any time during his stay in Napoli. I am enormously grateful to **Dr. Antonio Di Nitto** for important corrections and suggestions on thesis. My thanks also to my other colleagues, Pierluigi Casolaro, Bartolomeo De Canditiis, and Federico Davide for their friendly behavior to adjust in a completely new work place.*

*I would like to express my gratitude to **Prof. Giovanni La Rana** (director, Istituto Nazionale di Fisica Nucleare (INFN) section of Naples) for providing me the hospitality and the access to the INFN facilities. He has always encouraged me by giving his valuable advice and wanted to be updated about the research progress. My thankfulness further goes*

to ***Prof. Leonardo Merola*** *(director, Department of Physics "Ettore Pancini", University of Naples "Federico II"), for providing financial support to attend conferences, schools and experiments held outside Napoli. I am also giving my thanks and gratitude to my PhD coordinator* ***Prof. Salvatore Capozziello****, who was always cordial to me and was ready to assist for any kind of problem regarding doctoral school. I can not forget to thank* ***"European Nuclear Science and Applications Research (ENSAR)-2"*** *project for the financial support during my stay for attending experiments held in JYFL and IPN-Orsay. I would also like to thank the* ***JYFL*** *Accelerator Laboratory scientific director* ***Prof. Ari Jokinen*** *and staff for providing us good beams and a cordial environment during the experiment.*

I should specially thank our PhD secretary ***Mr. Guido Celentano****, who is unbelievably helpful for foreign students. During PhD study, I had to go outside Italy many times and every time he helped me for solving all bureaucratic tasks. Besides these, he was always ready to help for any kind of personal problems. In short, I have never seen so much cordial and helpful person in my entire life. I need to be grateful to* ***Dr. Luigi Campajola****, who was very sincere in his teaching. He was kind enough and always tried his best to make familiar me with all experimental instruments in Tandem Accelerator lab. I would like to show my sincere gratitude, warmth and appreciation to* ***Professor Renato Fedele*** *and* ***Dr. Iaia Masullo****. These two persons were like as my family members in every need. I will never forget their support during all difficulties I faced here.*

I have to say about ***Professor Dewan Abdul Quadir*** *(chairman, department of Physics, Uttara University, Bangladesh), who was a very cordial person during my job period in that university. He allowed me so much time to collect Visa to attend this PhD program.*

From where life begun, ***my mother****, she was very supportive during PhD study as usual. In fact, to have such friendly mother in life, will make all problems so easy to solve. Another person, my brother 'Mamun', who was also helpful in all aspects of life. Thank you so much my dear brother. I like to thank all members of my in laws house, especially 'Lovely apu' for being supportive all the time who filled up the lacking of having an elder sister in my life.*

Last but not the least, from the core of my heart I express my thanks and love for the most important person in my life, my dear wife ***Dr. Tahmina Akhter*** *who is my main source of inspiration for higher study abroad. She supported to make my life so beautiful in every aspects. By the grace of Almighty Allah, she gave me the best gift one can expect, my daughter* ***Aisha Binte Ashad****. I can not imagine how I could survive without them. Life is beautiful with you two, for all Jazak Allah Khair my dear!*

Md Ashaduzzaman
31 October 2017, Naples, Italy

List of Symbols

σ – Cross-section

α – Exit channel mass asymmetry

α_0 – Entrance channel mass asymmetry

χ_{BG} – Businaro-Gallone mass asymmetry

σ_M^2 – Variance of Gaussian shape of Mass distribution

σ_{TKE}^2 – Variance of Gaussian shape of TKE distribution

χ – Nuclear fissility

χ_m – Mean fissility parameter

χ_{eff} – Effective fissility parameter

E^* – Excitation energy

E_C^0 – Coulomb energy

E_S^0 – Surface tension

C – Light velocity

n – Number of fission fragments

$V_{\|}$, V_{par} – Projection of velocity onto beam direction

$V_{\perp}$, V_{per} – Projection of velocity perpendicular to beam direction

ϑ_{gr}^{lab} – Gzazing angle in laboratoty coordinate system

V_B – Potential barrier

$2D$ – Two dimentional

$2V$ – Two-Velocity

List of Acronyms

ADC	Analog-to-Digital Converter
BE	Binding Energy
BF	Binary Fission
CFD	Constant Fraction Discriminator
CM	Centre of Mass
CN	Compound Nucleus
CNF	Compound Nucleus Fission
CCT	Collinear Cluster Tripartition
CORSET	CORrelation SETup
DAQ	Data AcQuisition
DI	Deep Inelastic
ER	Evaporation Residue
FF	Fusion Fission
FMT	Full Momentum Transfer
FWHM	Full Width at Half Maximum
HF	Heavy Fragment
HV	High Voltage
JYFL	Jyväskylän Yliopiston Fysiikan Laitos
LDM	Liquid Drop Model
LF	Light Fragment
LCP	Light Charged Particle
LRA	Long Range Alpha
MCP	Micro Channel Plate

MD	Monitor Detector
PES	Potential Energy Surface
PLF	Projectile Like Fragment
QF	Quasi Fission
QFasym	Quasi Fission-Asymmetric
QFsym	QuasiFission-Symmetric
SHE	Super-Heavy Element
SP	StoP
ST	STart
TAC	Time-to-Amplitude Converter
TDC	Time-to-Digital Converter
TF	Ternary Fission
TKE	Total Kinetic Energy
TKE_{avg}	Average Total Kinetic Energy
TLF	Target Like Fragment
TOF	Time-Of-Flight
TP	Ternary Particle
TTF	True Ternary Fission

Abstract

The study of the true ternary fission (simultaneous decay in three fragments of similar mass) with formation of a heavy third fragment due to strong shell effects has received new interest among nuclear physicists. It is a very rare process which has been studied both theoretically and experimentally since several decades, but still it is quite far from proper understanding.

This PhD thesis concerns with the experimental observation of true ternary decay in three reactions. Specifically, $^{37}Cl + ^{208}Pb$ at 195 MeV, $^{40}Ar + ^{205}Tl$ at 193 MeV and $^{40}Ar + ^{208}Pb$ at 193 and 230 MeV reactions were studied at the K130 Cyclotron accelerator of the University of Jyväskylä, Finland. The first two reactions populating the same compound nucleus were investigated for possible entrance channel effects, whereas for the last system, ^{40}Ar + ^{208}Pb, two different bombarding energies have been provided to investigate the effect of excitation energy of the compound system. Four time-of-flight (TOF) arms coupled with six $\Delta E - E$ telescopes of silicon detectors and a beam monitoring system constitute the complete experimental setup. Two-dimensional velocity coincidence maps were built from TOF arms. The presence of cluster patterns in the two-velocity maps for all the reactions is the main observation of this work. Another outcome of the present investigation is the consistent overlap between the tripartitions that reproduce the data in the companion reactions ^{37}Cl + ^{208}Pb and ^{40}Ar + ^{205}Tl, and in the reactions ^{40}Ar + ^{208}Pb at 193 and 230 MeV. These two findings give support to the occurrence of the simultaneous three-body decay. The comparison between the rate for binary and ternary decays has also been achieved by calculating the ratio of such events corrected for the efficiency. These ratios are quite striking because in spontaneous fission the simultaneous ternary decay is several orders of magnitude less abundant. In the case of ^{37}Cl + ^{208}Pb and ^{40}Ar + ^{205}Tl, true ternary fission is even from 2 to 4 times more abundant than binary fission.

Introduction

The breakup of a nucleus into three fragments is known as ternary fission. This nomenclature has been used for cases where the third fragment is a light nucleus having mass up to A = 30. The breakup into three nearly-equal mass fragments (true ternary fission, TTF) has been recently reported in the spontaneous fission of ^{252}Cf. The three fragments have strong connection with shell closures, namely have a magic number of protons or neutrons or both. For heavier nuclei, ternary fission could be more likely, well confirming the pioneering experimental work. Furthermore, ternary fission could be extremely important in the r-process nucleosynthesis being expected to be competitive with β delayed fission for heavy nuclei in the range of $Z^2/A > 30.5$.

Shell effects may significantly reduce the ternary fission barriers, even for oblate deformations of very heavy nuclei. It is easy to verify that with increasing mass number of the heavy nucleus, more and more possibilities for its division in three magic nuclei appear. However, an in-depth study of this topic has not been performed yet, and the question about a possibility for a simultaneous three-body decay of heavy nuclei remains unanswered both in theory and in experiment.

The branching ratio of ternary decay with respect to binary fission (BF) is a matter of controversy and since ternary fission is an exotic process, theoretical and experimental understanding is not completely achieved. The study of ternary fission would further help us to understand the configuration of the nucleus at scission and would provide important information on the role of the structure of the emerging fragments.

This thesis work is based on an experimental program aimed at exploring the production of ternary decays, which are triggered by shell effects, in reactions induced at energies around the Coulomb barrier. Ternary fission could indeed be more probable (and reachable) if a combination of three fragments, all having a shell closure, would be allowed by the multidimensional potential surface, or if the nucleus would live in states where a configuration with three clusters is allowed.

The experimental program is devoted to the detection of all fragments to rebuild the total mass from the kinematics. Using this concept, an experiment was carried out with three reactions at the K130 Cyclotron accelerator of the University of Jyväskylä, Finland, also known as JYFL (Jyväskylän Yliopiston Fysiikan Laitos). The setup consisted of four arms of the CORSET TOF spectrometer coupled with six $\Delta E - E$ Telescopes. In particular, the binary and ternary decays of three reactions, namely ^{37}Cl + ^{208}Pb, ^{40}Ar + ^{205}Tl and ^{40}Ar + ^{208}Pb were studied.

The observables of choice for these types of reactions are the velocity vectors of the fragments. Taking into account the two and three body in-plane kinematics, binary fragments were detected in the forward direction by placing two time-of-flight arms symmetrically around the beam at the folding angle for symmetric decay and following TKE Viola systematics. Asymmetric decays are still detected considering detector openings. For the ternary decay case, two fragments are detected at forward angles, at a folding angle smaller than the one of the symmetric fission, and the third fragment at a backward angle. It is important to remark that both arms in the forward hemisphere are at the same angle with respect to the beam, on opposite sides, because this establishes a strong constraint on the 3-body kinematics to eliminate the overlap with sequential fission events. By taking advantage of the 3-body kinematics, a coincidence between three detectors, two in the forward and one in the backward, is considered as a candidate event for the ternary decay. In fact, by measuring 1) the velocity vectors of the two fragments in the forward hemisphere and 2)the energy and the average angle of the backward emitted fragments, the masses of the three fragments can be extracted. With this triple coincidence geometry, it is possible to exclude triple coincidences from possible sequential fission, namely, three bodies in the final state as a consequence of two sequential binary decays. Furthermore, it is important to perform the study with several reactions in order to investigate the importance of the entrance channel which favors the decay.

Chapter 1

Nuclear Fission

1.1 Introduction

The process of nuclear fission, namely the division of a nucleus in two lighter nuclei, was first observed by O. Hahn and F. Strassmann in 1938 by chemical analysis while irradiating natural uranium with thermal neutrons [1, 2]. In the same year of fission discovery, Meitner and Frisch [3] explained the process qualitatively within the framework of the liquid drop model (LDM) [4]. This process can take place either by nuclear reaction or spontaneously.

Nuclear fission is predominantly a binary process. The two newly produced nuclei, also known as primary fragments, can be excited and evaporate neutrons. This process gives rise to the so called secondary fragments of the primary binary splitting. Along with the appearance of two fragments in the final state, a third light fragment, known as ternary particle (TP), can be produced in one out of hundreds spontaneous fission binary events. This process is known as ternary fission (TF). Indeed, the three fragments of TF can be the consequence of a simultaneous breakup (direct mode) or a sequential decay (cascade mode). These possibilities are schematically shown in Fig. 1.1 and are defined as it follows:

Spontaneous (Simultaneous or Direct) Ternary Fission

The decay of a nucleus into three fragments in one step is known as direct ternary fission [5]. A schematic representation of this process is given in Fig. 1.1a, where a fissioning nucleus decays into fragments A_1, A_2, and A_3.

Sequential Ternary Fission

A heavy nucleus may decay into three fragments in two steps. The first step is the asymmetrical binary decay consisting of one light and one heavy fragment. When the heavy fragment has a sufficiently high excitation energy, it may, in turn, decay into two fragments, within a time scale of 10^{-20} seconds [5]. A schematic representation of this process is given in Fig. 1.1b. Also in this case there are three fragments in the final state.

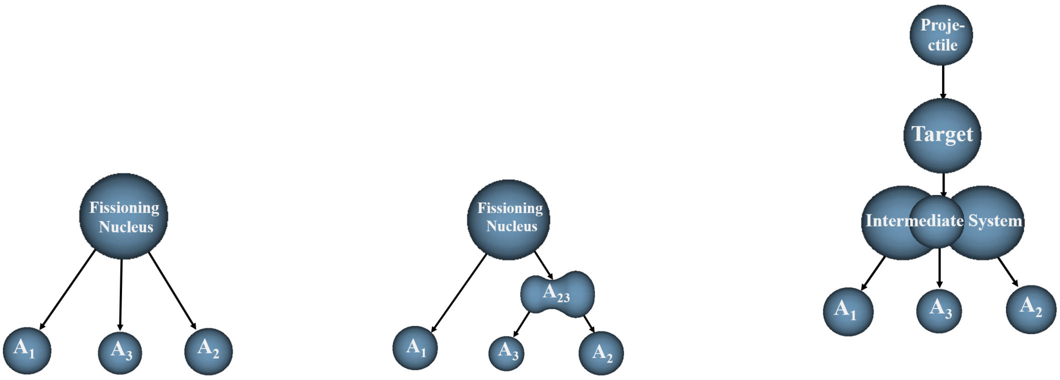

(a) Spontaneous *(b) Sequential* *(c) Induced*

Figure 1.1: Schematic representation of ternary fission processes.

Induced Ternary Fission

Direct and sequential ternary fission can occur both spontaneously or as a result of a collision between heavy nuclei. In an induced ternary fission, three fragments are produced from an intermediate nucleus. A schematic representation of this process is given in Fig. 1.1c. As it will be discussed later on, not necessarily TF may proceed through a compound nucleus stage.

The formation of three nearly equal mass fragments ($A_1 \simeq A_2 \simeq A_3$) during these processes is known as true ternary fission (TTF) [6]. TF has been observed experimentally and occurs with much smaller probability ($\sim 10^{-3}$) compared to the binary fission (BF). In the TF, mostly alpha particles are emitted as ternary particles with the largest probability in the direction perpendicular to the binary fission axis [7, 8]. This supports the idea that the third fragment appears from fluctuations in the neck region [6, 9].

1.2 Evidence of TTF

Recently, it has been claimed that TTF has been observed experimentally as a spontaneous decay of ^{252}Cf and in the case of ^{235}U bombarded with neutrons [10–13], using the missing mass method and a double time-of-flight (TOF) spectrometer. These experiments have been performed at the FOBOS setup [14]. It is claimed that, as predicted in many theoretical studies [15, 16], TTF decay occurs dominantly in a collinear geometry when the three fragments have strong connections with shell closures. It was therefore called collinear cluster tripartition (CCT). Figure 1.2 shows the two-dimensional mass distribution ($M_2 - M_1$) of the two detected masses of the coincident fragments during these two experiments.

Figure 1.2a is for the case of spontaneous fission of ^{252}Cf, where the center line for the measured total mass ($M_s = M_1 + M_2 = 225\ amu$) is shown as a border line separating events from normal BF. The symbols 1 and 2 are used to mark the conventional BF events.

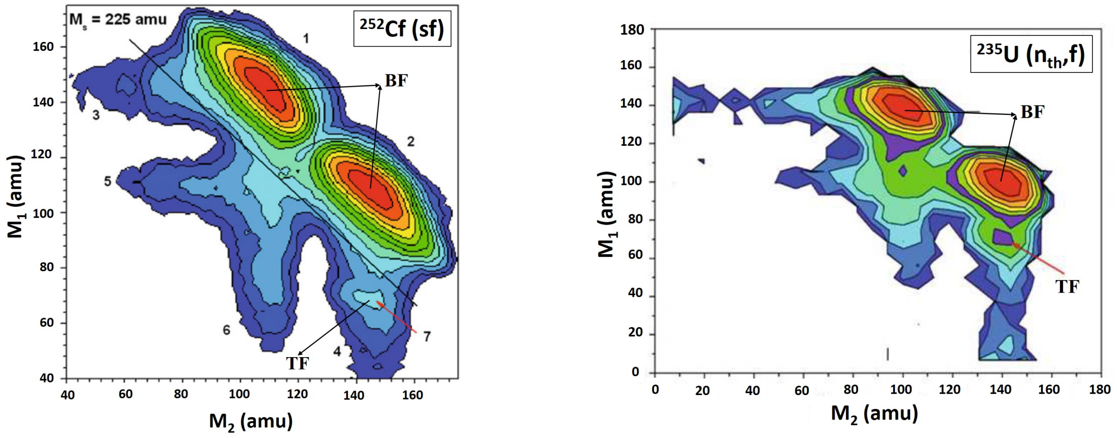

(a) Spontaneous decay of ^{252}Cf *(b)* ^{235}U *bombarded with neutrons*

Figure 1.2: (Color online) Contour maps (in logarithmic scale, the steps between colors are approximately a factor 2.5) of the mass-mass distribution of the collinear fragments, detected in coincidence in the two opposite arms of the FOBOS spectrometer (from [10]).

The tails (marks 3 - 6) in the distribution indicate the scattering of fragments on both the foils and on the grid edges of the stop avalanche counters and the ionization chambers. Noticeably, a bump exists on the mark 7, on top of the tail 4. The bump is located in a region corresponding to a large missing mass that indicates cluster tripartition in which three fragments with comparable masses and with magic numbers of protons ($Z_1 = 50$, $Z_2 = 28$, and $Z_3 = 20$) are observed. Therefore, the spontaneous TTF channel observed as collinear cluster tripartition (CCT) [10, 17] having masses close to the magic (^{132}Sn, ^{70}Ni, and ^{48}Ca) isotopes, has a probability of not less than 4×10^{-3} with respect to BF. This is larger than the known TF accompanied by light charged particles (LCPs).
A bump similar to that marked by an arrow in Fig. 1.2a is again well pronounced as shown in Fig. 1.2b for the case of $^{235}U(n_{th}, f)$. The yield of the events in the bump is (5.1 ± 0.4) × 10^{-3} relative to the total number of fission events detected. For this case, the authors also concluded to observe the same CCT in the induced reaction $^{235}U(n_{th}, f)$. The extensive search for TTF as CCT on these experiments was performed by the group of D. Kamanin [18]. It was found that the TTF is a rather probable channel with the yield ratio to the binary one of about 10^{-4}. CCT was much earlier associated with some of detected two-body events in the reaction $^{40}Ar +^{238} U$ [19].

A much earlier result was published by Rosen and Hudson [20] in 1950 for the induced fission of ^{235}U by thermal neutrons. They determined the frequency of TTF relative to the frequency of BF by using a triple ionization chamber and coincidence counting method. They reported the frequency of TTF to be 6.7±3.0 per 10^6 binary fission in ^{235}U.

In 1961, Muga *et al.* investigated spontaneous TTF of ^{252}Cf [21–23] and thermal neutron induced TTF of Uranium and Plutonium [22–26]. They photographed the tracks of three fragments emitted in the spontaneous TTF of ^{252}Cf using a nuclear emulsion technique [21]. Later, using three semiconductor detectors arranged in a symmetric position (120^0) around a fission source in coincidence, they reported ternary yield of the order of 1.1×10^{-6} per binary fission event of ^{252}Cf [22]. A detailed study of *Cf*, *Pu*, and *U* nuclei has been performed by them in 1967 [23, 26], where they showed the energy spectra (shown in Fig. 1.3a) of individual fragments for both TTF and BF. Two peaks in the spectra of lightest mass fragment (shown in Fig. 1.3b) were observed. Those were the evidence of light mass fragment production in or near the range $30 - 40\,amu$ and $50 - 60\,amu$ of $^{240,242}Pu^*$ [24]

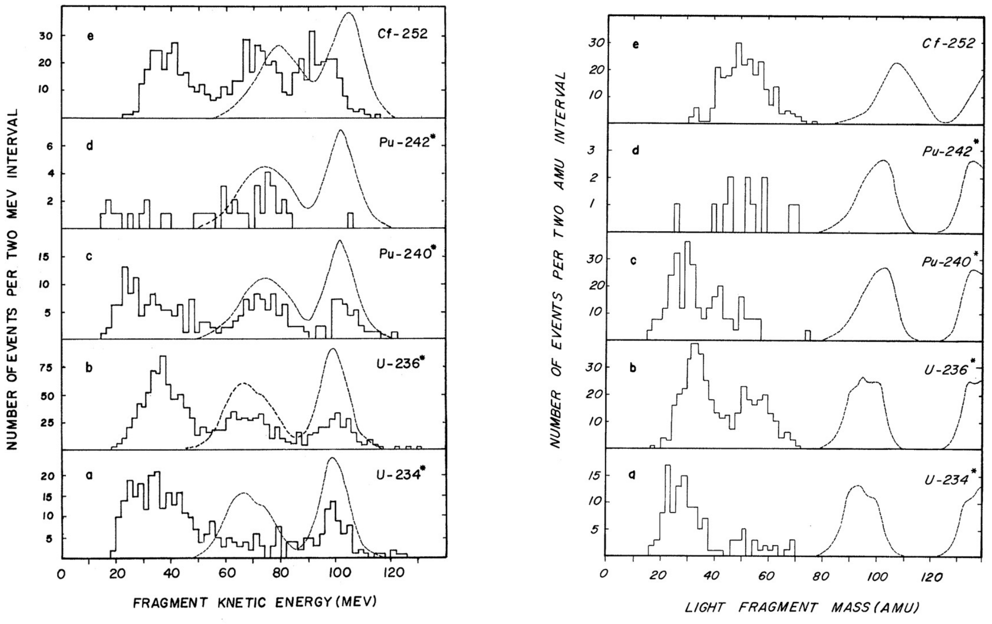

(a) Broken line represents the ternary events and dashed line represents the binary events

(b) Dashed line represents the ternary events and Broken line represents the ternary events

Figure 1.3: (a) Fragments kinetic energy distribution and (b) Light-mass fragment distribution from TTF and BF (from [23, 26]).

The cross section for both BF ($3.0 \pm 0.4\,b$) and TTF (1/30 of that for BF) was measured by Fleischer *et al.* [27] for the reaction $Ar + Th$. Iyer and Cobble [28] showed the existence of a TTF in the induced fission of ^{238}U by intermediate-energy (20-120 MeV) helium ions by measuring the absolute cross section of the fragments ^{24}Na, ^{28}Mg, ^{31}S, ^{38}S, ^{47}Ca, ^{56}Mn, and ^{56}Ni. They also showed that the probability of TTF increases with the increase in the excitation energy of the parent nucleus. A high TTF to binary ratio of $4.3 \pm 0.7\%$ was measured by Becker *et al.* [29] for the case of uranium irradiated with 540 MeV *Fe* ions.

They also reported that TTF increases with excitation energy and with projectiles heavier than Ar. Schall *et al.* [30] have searched with position sensitive ionization chambers for a spontaneous TTF of ^{252}Cf and from the few events registered with relative angles around $\theta = 120°$ in the laboratory reference frame, they deduced an upper limit of 8×10^{-8} per binary fission. Stoenner *et al.* [31] deduced upper limits for the yields of Ar which are reported to be three to seven orders of magnitude lower than those expected from thermal-neutron induced ternary fission of ^{235}U as described by Muga [23, 25, 26]. Vater *et al.* experimentally deduced the ratio of TTF to BF to be (2.4 ± 1%) in the reaction of uranium with 414 MeV Ar-ions [32].

From the very beginning of the discovery of binary nuclear fission [1, 2], the liquid drop model (LDM) [4] was used to interpret this new phenomena of TTF. Present [33, 34] pointed out as early as 1941 that a heavy nucleus surprisingly fissions into two fragments rather than into three or more, even though division into three or more fragments would release more energy (for details see section 1.2.1).

It is reported in [7] that a third light fragment, such as an α particle was produced in 90% of the cases of TF, a heavier helium in 9%, and a particle with $Z > 2$ in less than 1% in spontaneous fission. The probability of TF is found to decrease exponentially with the increase of the TP mass [7]. The nomenclature of TF has been used for cases [7, 30] where the third fragment is a light nucleus up to mass $A = 30$. The spontaneous emission of the third fragment in the fission decay of heavy radioactive nuclei has been measured with a large variety of light-charged ternary particles like $^{1,2,3}H$, $^{3,4,5,6,8}He$, ^{10}Be, and ^{14}C. They have been observed in coincidence with the main fission fragments, in a direction perpendicular to the fission axis [35–39]. Even heavier ternary particles like $^{14-18}C$, $^{16-18}N$, $^{20-22}O$, $^{20-25}F$, $^{21,23-25,27,28}Ne$, $^{24,25,27,28,30}Na$, $^{27,28,30,31,32}Mg$, $^{30,32,33}Al$, and $^{32-35}Si$ have been observed [20, 27–29, 40–44]. In the neutron-induced fission of ^{242}Am, ternary events with the isotopes of F, Ne, Na, Mg, Al, and Si as ternary particles have been observed by Gönnenwein *et al.* [41]. In another experiment by Köster *et al.* [42], the yields and energy distributions for the isotopes of hydrogen to silicon as ternary particles were reported. The energy distribution and yields for various isotopes of lithium to silicon as ternary particles have been reported by Tsekhanovich *et al.* [44]. This experiment also puts an upper limit of 1×10^{-8} on the range of the yields for the heavier ternary particles like ^{39}P and ^{40}S.

1.2.1 Energy Balance in TTF

The energy released in multiple breakups was calculated by several physicists at the time of TF discovery, for example Meiter and Frisch [3]. It was found that the amount of energy release was quite large (200 - 205 MeV) due to high binding energy (BE) per nucleon (BE/A). Theoretically, it was pointed out by Present [34] in 1941 that Uranium tripartition would release about 20 MeV more energy than the binary one. The decay energy for fission of a nucleus into n about equally sized fragments and its dependence on Z^2/A parameter (which is related to the fissility parameter χ, see definition 1.3.1 later on), has been calculated by Swiatecki [45] for different values of n. The results of Ref. [45] (shown in Fig. 1.4) can be summarized as it follows:

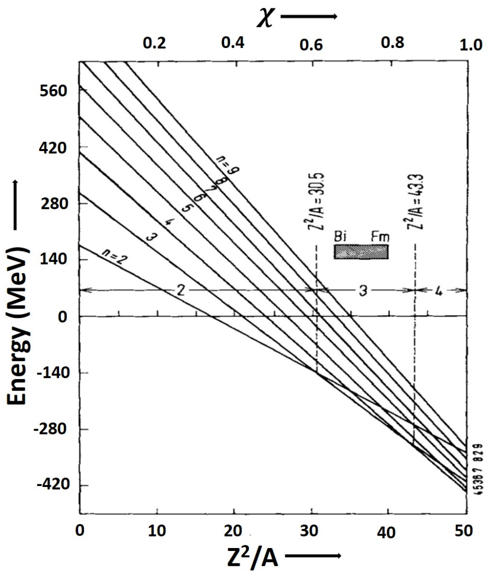

Figure 1.4: Decay energy of an ideal, electrically charged liquid drop as a function of fissionability parameter χ and of the value of Z^2/A (from [45]).

1. if $Z^2/A < 30.5$, binary fission (BF) is energetically more favorable than all other fission processes;
2. if $30.5 < Z^2/A < 43.3$ (elements from ^{83}Bi to ^{100}Fm), TF is energetically more favorable than other processes;
3. if $Z^2/A > 43.3$, multiple fission becomes more and more energetic, meaning that fission into four fragments releases the largest amount of energy.

A tripartition ($n = 3$) into equal masses becomes exothermic for $\chi \geq 0.426$ and from $\chi = 0.611$ onward, its energy gain is greater than the BF case. With increasing charge of the nucleus, fission into even more fragments becomes energetically favorable. It is important to remark that this conclusion involves only the initial and final states of the fission process and gives no information about the barriers or fission probabilities, nor on the decay mode or time scale.

1.2.2 Barrier Height

Multi-fragment fission is a rare process because not only the energy balance but also the height of the fission barrier is responsible for determining the yields of the process. A more detailed analysis of the saddle and scission shapes were undertaken by Diehl and Greiner [46]. On the basis of a two-center shell model [47] and a three-center shell model [48–50], they built potential energy surfaces (PES) vs. different shape parameters. With a more complex parametrization of the shapes they showed that it is possible to study the paths in the PES bringing to prolate (collinear) or oblate (equilateral) configurations of the three nascent fragments, and to provide an explanation of the lower ternary decay probability. In short, TF path is double-humped, and the second barrier (second saddle) is more than three times higher than the liquid-drop barriers for the BF path. An increase in the charge leads to a gradual reduction of the second barrier which eventually disappears. At this point the choice of the fission mode depends on dynamical effects. However, for heavier nuclei, the barriers for TF are only slightly higher than the case of BF [46]. Hence nuclear tripartition could be more likely which well confirms the pioneering experimental work by Fleischer *et al* [27]. For this reason, TF is also an extremely important ingredient of the r-process nucleosynthesis being competitive with β-delayed fission [51] for heavy nuclei in the range of $Z^2/A > 30.5$.

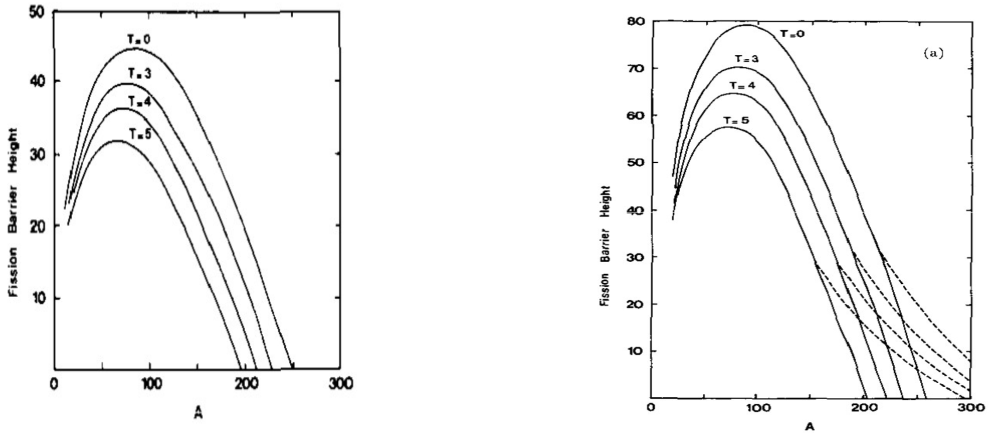

(a) Binary fission

(b) Ternary fission

Figure 1.5: Barrier heights (in units of MeV) for the fission of nuclei along the β stability valley as a function of temperature and mass number (from [52]).

Later on, barrier height calculations for BF and TF were also performed by Royer and Mignen [52] within the rotational LDM at finite temperatures and including the nuclear proximity energy as a function of the temperature of the nucleus. Fig. 1.5 shows that in the mass region around 200, barrier height of BF is about 20 MeV for zero temperature, whereas for TF barrier height is about two times higher. For larger masses, both barriers reach gradually similar values as in [46]. With increasing temperature, all fission barriers decrease because the main temperature effect is to reduce the surface tension of the rotating drop. An early study on TF within the more sophisticated three-center shell model [48] shows that shell closures play a very important role and may significantly reduce the ternary fission barriers even for oblate deformations of very heavy nuclei. Shell closures may favor TTF, with respect to BF, in cases where combinations of fragments having a magic number of neutrons or protons are possible.

1.3 Role of Potential Energy Surface

It has been demonstrated that in heavy ion collisions at energies around the Coulomb barrier shell effects have a strong influence upon the evolution of heavy nuclear systems. If the time evolution of the nuclear system during a reaction is represented in terms of the time evolution of some collective variables connected by a driving multidimensional potential, the nuclear

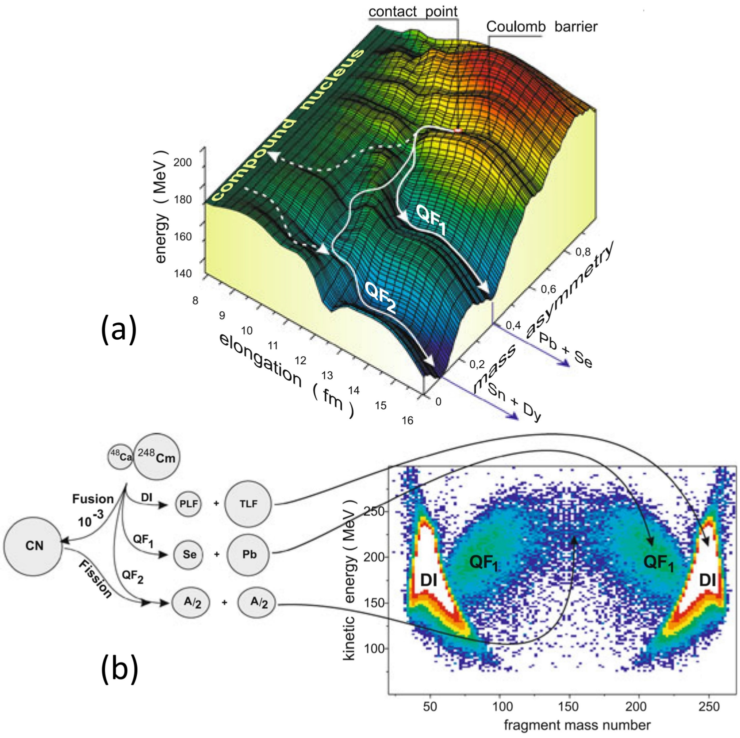

Figure 1.6: (a) Driving potential for the nuclear system formed in ^{48}Ca+^{248}Cm collision (from [53]). The solid lines with arrows show schematically (without fluctuations) the quasi-fission trajectories going to the lead and tin valleys. The dashed curves correspond to fusion (CN formation) and fission processes. (b) Mass-TKE distribution of reaction fragments in collision of ^{48}Ca with ^{248}Cm at 203 MeV center-of-mass energy (from [66]).

dynamics is driven mainly by the multidimensional potential energy surface. The most relevant collective variables are the distance between the nuclear centers of the emerging fragments (elongation), surface deformations, mutual orientations of deformed nuclei and charge and mass asymmetries.

At low excitation energies the nuclear system creeps along the valleys of the potential energy caused by the nascent fragments magic structure. Starting from an injection point, namely, the entrance channel asymmetry and interaction energy, the nuclear system falls in the local minima of this potential surface and finally splashes out in the exit channels with formation of energetically favorable closed shell nuclei. The potential energy of any physical system is a key quantity which determines its properties and time evolution. For instance, in the case of $^{48}Ca +^{248} Cm$ reaction [53], PES can drive the nuclear system via fission and QF (shown in Fig. 1.6). The effect of the QF on the symmetric component can also be explained by the potential energy surface of this reaction.

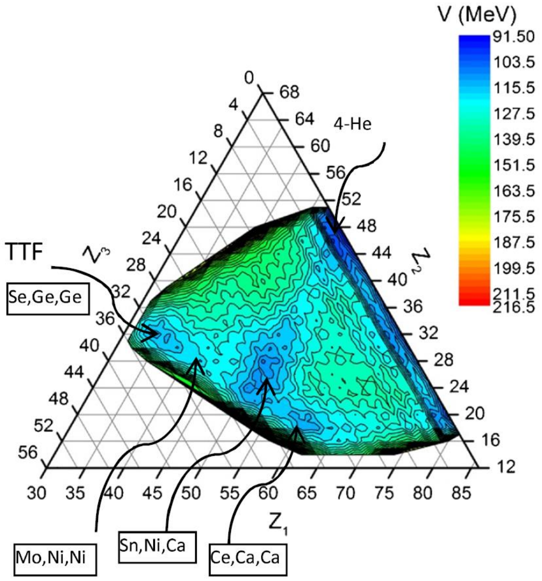

Figure 1.7: Potential energy surface as a function of charge number of ternary fission of ^{252}Cf *(from [60]).*

TTF has also been the subject of several recent theoretical studies concerning ^{252}Cf

[54, 55] based on PES calculated by a three cluster model (TCM) [54–61] (Details shown in Appendix D). The relative yields of all possible ternary fragmentations of ^{252}Cf satisfying the condition $A_1 \geq A_2 \geq A_3$ have been computed in equatorial and collinear configurations. As a consequence of strong shell effects, the potential shows minima when fragments are magic nuclei and it is shown in Fig. 1.7.

In particular, calculations reveal that the collinear configuration increases the probability of emission of heavy fragments like ^{48}Ca and its neighboring nuclei as the third fragment. The model indicates that the collinear configuration is the preferred one for the intermediate nuclei ^{48}Ca, ^{50}Ca, ^{54}Ti, and ^{60}Cr as the third fragment, whereas the equatorial configuration may be a preferred configuration for lighter nuclei.

1.3.1 Ternary Quasifission of heavy nuclear systems

Three-body decay may also be explored in quasifission (QF) if one takes advantage of the fact that this process is strongly influenced by the shell closure of the emerging fragments [62], namely by the PES of the nucleus built on the total number of protons and neutrons. The idea of TTF driven by shell effects was also proposed by Zagrebaev and Greiner [53].

On the basis of the potential surfaces built with a two-center shell model [47], it was shown that it is possible to explain an enormous set of experimental data on the Mass-TKE distributions of binary reactions between heavy nuclei leading to QF. At the same time it is possible to predict possible decay paths leading to three-body decay of fragments of close-by masses. These paths are only possible because of shell effects. A reported case is the one of ^{248}Cm [53], where potential energy of the three-body contact configuration is shown in Fig. 1.8. As it can be seen, this nucleus preferably decays in two (tin-like and palladium-like) fragments. The potential energy smoothly increases with increasing charge of the third nucleus and no other local deep minima appear on the potential energy surface. Though the combinations like *Te-O-Kr* or *Sn-O-Sr* are located not so high up on the potential energy surface (10-20 MeV), and they are quite reachable due to fluctuations at several tens of MeV

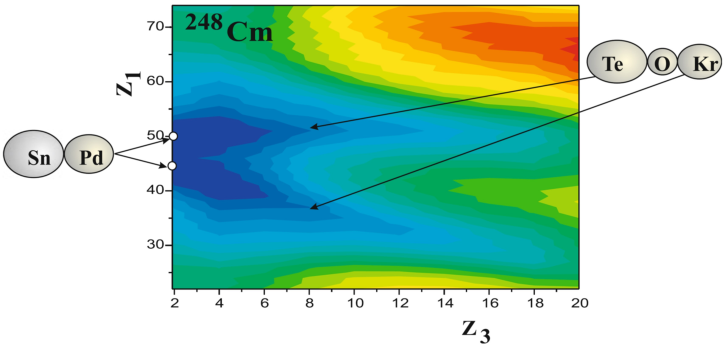

Figure 1.8: Landscape of the potential energy surface for three-body clusterization of ^{248}Cm *(from [53]).*

of excitation energy.

Furthermore, it is found that with increasing mass number of the heavy nucleus more and more possibilities for its clusterization appear [53]. Very recent calculations based on a macroscopic approach [50] show how a TTF path emerges from a proper shell correction on the top of a macroscopic liquid drop potential.

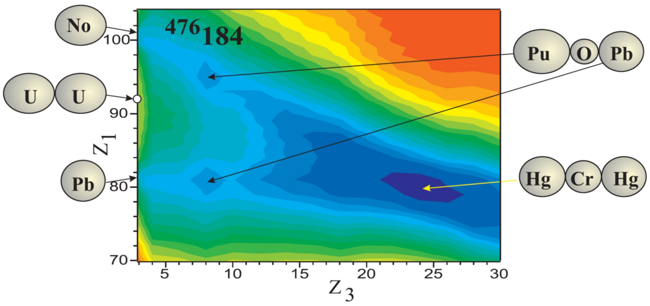

Figure 1.9: Landscape of potential energy of three body configurations formed in collision of $^{238}U + ^{238}U$ *(from [63]).*

TTF are also predicted for giant nuclear systems where no fusion is possible at all. If one considers that nuclear structure may significantly influence the nucleon flow in dissipative heavy ion collisions, the system ^{238}U + ^{238}U [63] may end up into three fragments in the final states because the PES drives the mass transfer. From Fig. 1.9 its possible to see that there are several minima in the potential energy and some of them corresponds to TTF. Even without forming a compound nucleus (CN), TTF might be possible if mass transfer is driven by shell effects. This process may be termed as three-body QF. In this giant system, shell effects significantly reduce the potential energy of the three-cluster configurations formed by two strongly bound lead like fragments and one oxygen fragment caused by the $N = 126$ and $Z = 82$ nuclear shells. Other than this, there is another minima in the PES which indicate TTF as a Hg, Cr, and Hg fragments is also caused by the $N = 126$ and $Z = 82$ nuclear shells.

The mechanism of QF [64–66] can be an effective pathway to induce TTF. A clear picture of the process and what enhances or hinders it, is needed to be discussed. It is important to explain the properties of QF as a heavy ion reaction mechanism, since by using these properties, we aim at populating the PES valley corresponding to a three-body decay in the final stage. Among all the reaction channels, complete fusion and QF are competing processes [67–70]. QF is the strong counteracting binary process which is a transitional mechanism between deep inelastic collisions [71] (formation of projectile-like and target-like fragments) and complete fusion. During the QF process, the composite system separates in two main fragments without forming a CN. Even though the Coulomb barrier is overcome (intermediate stage), QF is the most important mechanism that prevents the formation of super heavy element (SHE) in the fusion of heavy nuclei. Three criteria are widely used to identify the presence or onset of QF:

- **Charge product of reaction partners** Z_1Z_2 (Coulomb factor) which is related to Coulomb barrier in the entrance channel. The threshold value of Z_1Z_2 for the appearance of QF is set to 1600 by the calculations of Swiatecki [72] and enough well verified experimentally (i.e., QF appears when $Z_1Z_2 > 1600$).

- **Entrance channel mass asymmetry**,

$$\alpha_0 = (A_{projectile} - A_{target})/(A_{projectile} + A_{target}),$$

where $A_{projectile}$ is the mass number of projectile and A_{target} is the mass number of target. With decreasing α_0, cross-section for QF increases. The estimate of mass asymmetry for the appearance of QF can be qualitatively given in the frame work of the Businaro-Gallone picture. According to this, QF appears for systems with entrance channel mass asymmetry lower than the Businaro-Gallone mass asymmetry (α_{BG}) defined as [73]:

$$\alpha_{BG} = 0, \quad when\ \chi_{CN} < 0.396$$

$$\alpha_{BG} = 1.12\sqrt{\frac{\chi_{CN} - 0.396}{\chi_{CN} - 0.156}}, \quad when\ \chi_{CN} > 0.396$$

where χ_{CN} is the fissility parameter which is defined as,

$$\chi_{CN} = \frac{E_c^0}{2E_s^0} = \frac{Z^2/A}{(2a_s/a_c)\left[1 - K\{(N-Z)/A\}^2\right]}, \tag{1.3.1}$$

where E_c^0 is Coulomb energy, E_s^0 is the surface tension, a_c and a_s are related to parameters E_c^0 and E_s^0 respectively, and K is the surface asymmetry constant.

- **Mean fissility parameter** (χ_m) which is defined as a linear combination between effective fissility parameter (χ_{eff}) and true fissility parameter (χ_{CN}) reflecting the stability of CN with respect to fission. The mean fissility parameter was mentioned in [74]:

$$\chi_m = 0.75\chi_{eff} + 0.25\chi_{CN}.$$

The effective fissility parameter is connected with repulsive and attractive forces in the entrance channel by the following relation [75]:

$$\chi_{eff} = \frac{4Z_1Z_2/\left\{A_1^{1/3}A_2^{1/3}\left(A_1^{1/3} + A_2^{1/3}\right)\right\}}{50.883\left\{1 - 1.7826\left(\frac{A_{CN}-2Z_{CN}}{A_{CN}}\right)^2\right\}}.$$

From the analysis of a large data set of mass-angle distributions of fission-like fragments obtained in the reaction with heavy ions [74] it has been found that the QF onsets for reactions with $\chi_m > 0.68$ and becomes dominant at $\chi_m > 0.765$.

Indeed the three mentioned criteria are not exhaustive. For instance, the ground state shapes of the interacting nuclei are not taken into account. Coulomb barrier and the distance between the centers of the colliding nuclei changes by the relative orientation of deformed nuclei. Also relative orientation leads to a change in the balance between repulsive and attractive forces. A higher formation probability of a CN is expected when two interacting nuclei touch each other by their lateral surfaces (near-side collisions); on the other hand, when nuclei touch each other by their poles (near-tip collisions), a higher QF probability is expected in the elongated configuration. For the first time, the impact of nuclear orientation effects on QF was noticed experimentally in the reactions with deformed nuclei $^{12}C + ^{232}Th$, $^{16}O + ^{238}U$ [76–78]. Later on, orientation effect was also widely studied in the reactions $^{48}Ca + ^{144,154}Sm$ [79, 80], $^{16}O + ^{238}U$, $^{30}Si + ^{238}U$, $^{34}S + ^{238}U$ [67, 81–84].

Signatures of QF: An example that highlights the relative contributions of CNF and QF to symmetric splitting is the work of Shen et al. [69]. The reactions ^{22}Ne+^{249}Cf, ^{26}Mg+^{248}Cm, $^{36}S +^{238} U$, and $^{58}Fe +^{208} Pb$ are supposed to form the nuclei $^{271-274}Hs$ starting from different entrance channel asymmetry. It is important to note that all reaction partners, except ^{208}Pb, are well deformed nuclei. In the reactions with deformed nuclei the PES strongly depends on the relative orientation of the reaction partners. Fig. 1.10 gives a clear progression of the Mass-TKE distribution shapes with decreasing entrance mass asymmetry and increasing Coulomb repulsion. It is clearly seen that even at similar CN excitation energies the Mass-TKE distributions are quite different for these reactions.

In the case of the reactions $^{22}Ne + ^{249}Cf$ and $^{26}Mg + ^{248}Cm$, the mass distributions have a near Gaussian shape with no evidence for asymmetric fission. The reactions are considered to be mainly CNF process.

For the $^{36}S + ^{238}U$ reaction the mass distributions of the fission like fragments change remarkably. This difference in mass distributions for the $^{26}Mg + ^{248}Cm$ and $^{36}S + ^{238}U$ reactions is connected with an increasing contribution of the QF process for the ^{36}S-induced reaction. At low excitation energies QF is the dominant process for the reaction $^{36}S + ^{238}U$.

At higher excitation energies the mass distribution becomes symmetric and similar to the reaction $^{26}Mg + {}^{248}Cm$ though due to a remaining trace of QF slightly wider. At energies below the Coulomb barrier the mass distributions of fission like fragments formed in this reaction are dominantly asymmetric.

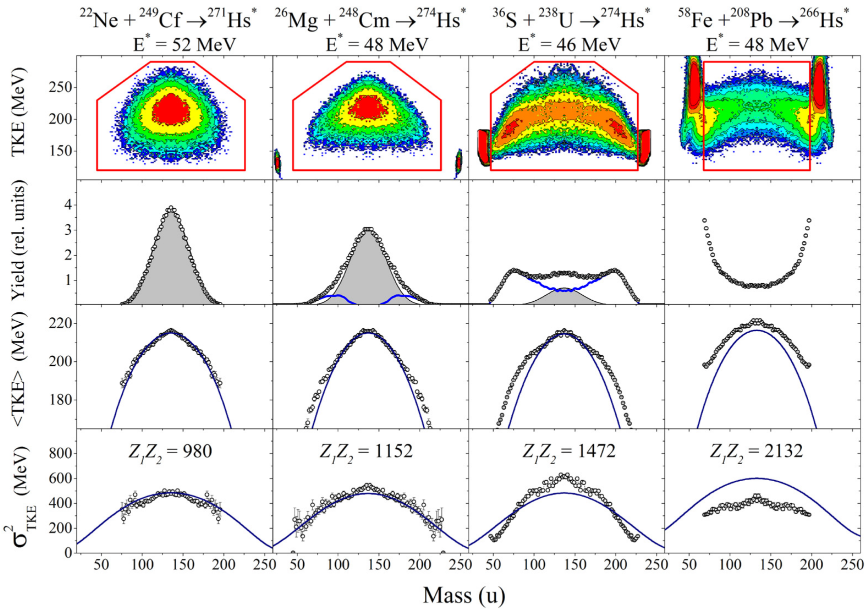

Figure 1.10: Mass-TKE distributions of fragments at energies above the Coulomb barrier. From left to right the entrance channel mass asymmetry decreases, and the Coulomb factor Z_1Z_2 increases. Solid curves in the average TKE and its variance are the expectation for CNF (from [69]).

In the case of the reaction $^{58}Fe + {}^{208}Pb$ the Mass-TKE distribution has a wide two-humped shape even at 48 MeV excitation energy. For this reaction the QF process dominates at energies below and above the Coulomb barrier. The large overlap between QF fragments, quasi-elastic and deep-inelastic events is observed due to the fact that one of the partners is doubly magic lead.

The progression in the Mass-TKE distribution, which makes one to invoke QF mechanism, is also reflected in the other two observables, the average TKE and the variance of the TKE distribution for a fixed mass split σ^2_{TKE}. Both these observables deviate from the expectation of the systematics based on CNF [85]. In particular, the deviations observed in the reaction ^{58}Fe + ^{208}Pb are a signature of the fact that QF process is dominant with respect to CNF in the full mass range.

Shell effects of QF: Shell closures in nuclei have a great impact in QF that can be confirmed by Mass-TKE distribution. The Mass-TKE distributions of two reactions ^{48}Ca + ^{168}Er and ^{12}C + ^{204}Pb leading to the same CN ^{216}Ra is shown in Fig. 1.11 [86]. Despite the excitation energy was around 40 MeV in both cases, the mass distribution of fragments obtained in the reaction ^{48}Ca + ^{168}Er shows two wide asymmetric shoulders. With the increase of excitation energy, the contribution to QF decreases. There is no asymmetric shoulders observed in the mass distributions of fission fragments formed in the reaction ^{12}C + ^{204}Pb.

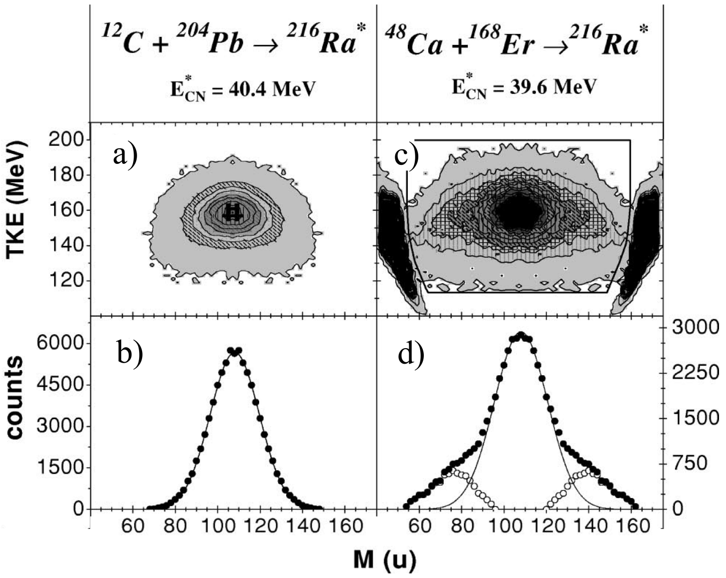

Figure 1.11: Mass-TKE of the correlated fission fragments from the reactions ^{12}C + ^{204}Pb *(left panels) and* ^{48}Ca + ^{168}Er *(right panels) as a function of fragment mass M: a) and c) show the two-dimensional matrices (M,TKE); b) and d) show the integrated mass distributions. Solid curves are Gaussian fits to the symmetric (central) components and open circles (right-hand panel only) correspond to the extracted asymmetric contribution (from [86]).*

Therefore, this asymmetric mode in the case of the reaction $^{48}Ca + {}^{168}Er$ is not due the formation of a CN after complete fusion, but might be the result of the QF process. In the fission fragment Mass-TKE distribution for the reaction with ^{48}Ca, shell effects are clearly seen.

It is possible to explain the contribution to the QF by the PES (Fig. 1.12) as calculated by Zagrebaev *et al.* [87], with a two-center shell model [47], as function of the mass asymmetry and elongation of the dinucleus. The two reactions correspond to two different entrance points in the PES. In the case of the ^{12}C, the contact point favors the path which leads to the CN that will fission symmetrically. In the case of the ^{48}Ca reaction, two optimal paths are possible, the symmetric one and the one that brings to a scission in the channel $^{132}Sn + {}^{84}Sr$ without forming a CN. This minimum in the PES is determined by the doubly magic ^{132}Sn. The mass distributions for two reactions are also shown in bottom-right corner. The two paths in the ^{48}Ca reaction result in the overlap of a symmetric peak and two asymmetric shoulders.

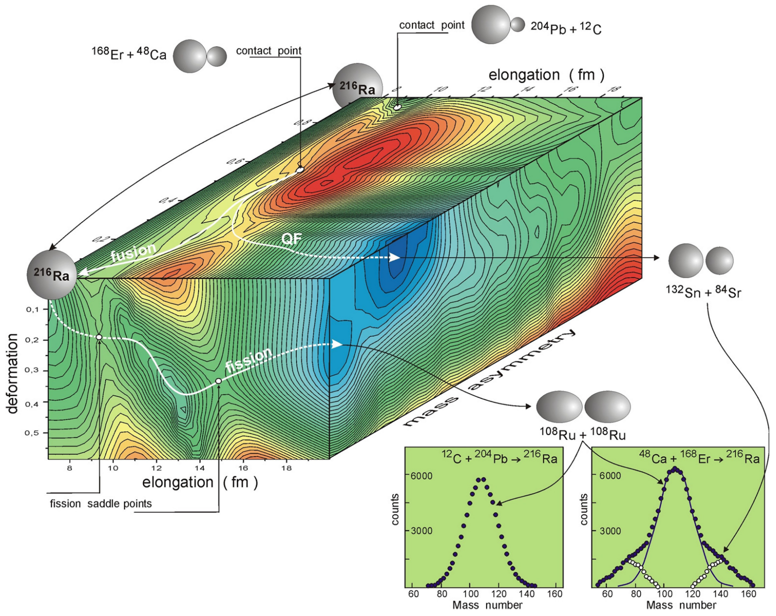

Figure 1.12: Potential energy as function of mass asymmetry and elongation of composite system ^{216}Ra (from [87]).

The importance of the shell effects still holds when heavier systems are considered. It is known that in superheavy composite systems QF mainly leads to the formation of asymmetric fragments with mass asymmetry ∼ 0.4 [88]. This type of QF process, the so-called asymmetric quasifission (QFasym), is characterized by asymmetric angular distributions in the center-of-mass system and thus fast reaction times ($\sim\ 10^{-21}s$) [68, 74]. The TKE for these fragments is observed to be higher than that for CNF and hence this process is colder than CNF. Due to this reason shell effects in QF are more pronounced [66].

Besides the asymmetric component, the symmetric component may be affected by the presence of the QF process. Consequently, the question of whether the symmetric fragments originate from CNF or QF processes (QFsym) arises (shown in Fig. 1.6). Furthermore, the angular distribution for all these mass-symmetric fragments is symmetric with respect to 90^0 in the center-of-mass system and the estimated reaction time is $\sim\ 10^{-20}s$, typical for CNF processes [68, 89]. The overlap of CNF and QF in the symmetric mass region constitutes an inescapable problem when the CNF cross section has to be estimated.

The fission fragments produced in the QFasym are strongly influenced by the nuclear shell closure. Generally, in heavy ion induced reaction, shell closure follow $Z = 82$ and $N = 126$ which is doubly magic ^{208}Pb nucleus. Fragments mass distribution of heavy ion reactions shows a wide two humped shape. The Mass-TKE distributions of binary fragments obtained in the reactions of ^{36}S, ^{48}Ca, ^{64}Ni ions with Uranium target at energies close to the Coulomb barrier were calculated in [90] and the results are shown in Fig. 1.13. The Coulomb factors (Z_1Z_2) for three reactions $^{36}S\ +\ ^{238}U$, $^{48}Ca\ +\ ^{238}U$ and $^{64}Ni\ +\ ^{238}U$ are 1472, 1840, and 2576 respectively. Mass-TKE distributions of three systems have typical wide two-humped shape caused by QF under the influence of closed shells with $Z = 82$ and $N = 50$, 126. In fact, as it was shown in Ref. [91], for the $^{48}Ca\ +\ ^{238}U$ reaction the maximum yield corresponds to fragments with masses 208u. The QFasym peak shifts to more symmetric masses for reaction with lighter projectiles [92]. On the other hand, for the heavier projectile ^{64}Ni the maximum yield of QFasym fragments corresponds to the heavy mass 215u [91]. The driving potentials at scission point calculated with NRV code [93] using the proximity model

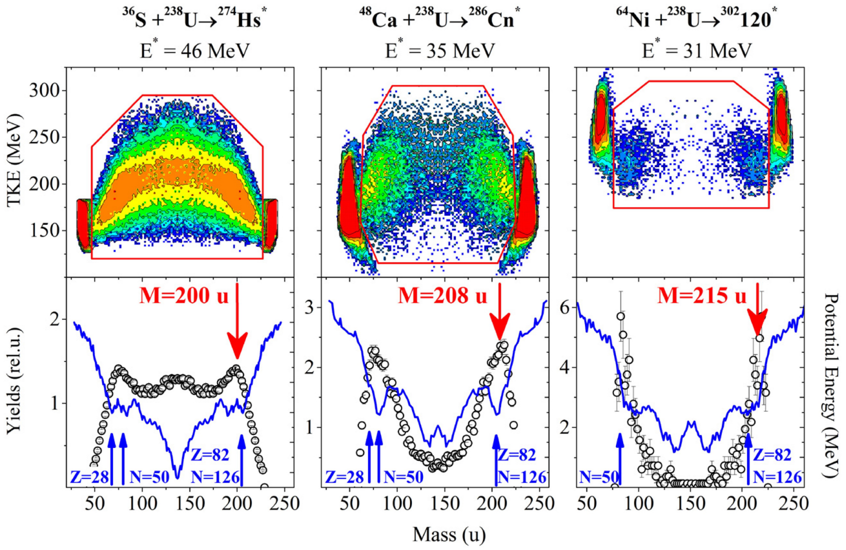

Figure 1.13: Top: Mass-TKE distributions for the reactions ^{36}S, ^{48}Ca, ^{64}Ni + ^{238}U *at energies close to the Coulomb barrier; bottom: open circles are mass distributions for fission-like fragments inside the contour line on Mass-TKE matrices and solid lines are the driving potentials as a function of mass (from [90]).*

together with experimental mass distributions are shown in the bottom panel of Fig. 1.13. It is clearly seen that the minimum of the driving potential corresponds to the maximum of the yield of QFasym fragments. The features of QFasym are essentially determined by the potential energy of the composite system whereas the feeding of the various valleys (namely, the relative contribution of QF to the capture cross section) mainly depends on the reaction entrance channel properties and on the dynamics. So, Fig. 1.13 reflects that shell effects truly play an important role in determining the fate of a binary reaction.

To have better explanation of entrance channel effect to formation of QFasym fragments, the mass distributions of fission-like fragments obtained in the reactions ^{36}S + ^{238}U and ^{26}Mg + ^{248}Cm having same CN $^{274}Hs^{*}$ are shown in Fig. 1.14. Despite of same CN, the position of the QFasym peaks changes [92] from 200u for ^{36}S + ^{238}U to 185u for ^{26}Mg + ^{248}Cm. According to the multimodal fission [94], the position of each mode determined by the nuclear shells is constant for specific CN and only the relative contribution of each mode varies in dependence of excitation energy which is dissimilar in this case. Thus, for

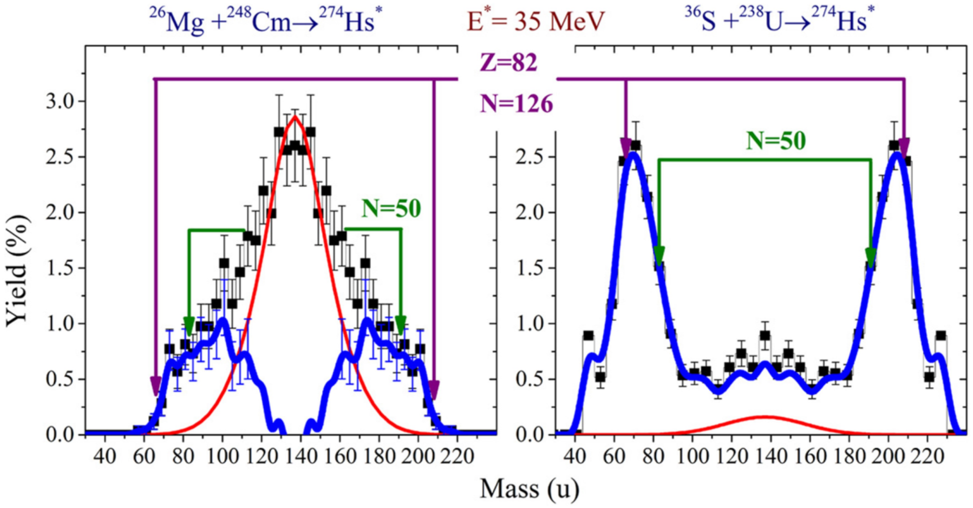

Figure 1.14: Mass distributions for fission-like fragments formed in the reactions ^{26}Mg + ^{248}Cm and ^{36}S + ^{238}U at energy below the Coulomb barrier. Red curves are fusion fission components estimated from TKE analysis, blue curves are QF components (from [92]).

more asymmetric reactions the Coulomb repulsion is expected to be smaller. For lighter projectiles this may lead to longer reaction times before separation for QFasym and thus to larger numbers of exchanged nucleons.

QF is still a subject of intense experimental investigation and a complete picture of this process is still lacking. Signatures of QF are found in different probes and a unique systematic behavior is still to emerge. QF arises with different characteristics in different observables depending also on the time scale [95]. Therefore measurement of Mass and TKE are the only way to distinguish between the two QF paths and to mitigate the risk to confuse the fusion cross section with a large part of the QF cross section. This point clarifies why it is so important to study Mass-TKE distribution for the QF process and its competition with CN formation. A reliable estimate of the fission cross section is in fact a decisive step in the search of the optimal reaction to produce superheavy elements.

From the discussion given above, it is clear that the PES can describe the output channels which are strongly connected with shell closure. Some of the minima in the PES can drive the system to TTF. It means that not necessarily the system will proceed through a formation of a CN. TTF can be produced without any fusion of the nuclei. This has been shown in Fig. 1.8 [53] and 1.9 [63].

1.4 Purpose of the thesis

This work is the first step of an experimental program set up to search for TTF induced by shell effects at near barrier energy. The program is inspired by the characteristics of QF that could drive the intermediate nuclear system to ternary decay at final stage without forming a compound nucleus. In almost all the previous works, people were looking for TTF in the spontaneous fission case. But nobody was completely successful in this search mission. Several works were done for neutron-induced ternary fission of ^{233}U, ^{235}U, ^{239}Pu, and ^{241}Pu [96–101]. On the other hand, a very few theoretical works [63] were done for 'heavy ion-induced' ternary fission, which seems to be a very favorable pathway for TTF. But there is no experimental work done in this regard yet.

Therefore the aim was to start an experimental program to explore the production of ternary decays in heavy ion-induced reactions at energies around the Coulomb barrier. In such reactions, the advantage is that it is possible to detect all the fragments and rebuild the total mass from the kinematics, with respect to the case of spontaneous fission [10].

Specifically, the study is focused on the binary and ternary decay of the following three reactions:

1. $^{37}Cl + {}^{208}Pb \rightarrow {}^{245}Es$,
2. $^{40}Ar + {}^{205}Tl \rightarrow {}^{245}Es$, and
3. $^{40}Ar + {}^{208}Pb \rightarrow {}^{248}Fm$.

For the above mentioned reactions, several shell closures may favor TTF. The potential energy has been calculated by TCM (shown in Appendix D) where fragments have shell closures. The calculated potential favors the possibility of observing TTF. Some of the possible

Reactions	A_1	A_2	A_3	$Q_{gg}\,MeV$	
				$Q_{gg}[^{37}Cl]\,MeV$	$Q_{gg}[^{40}Ar]\,MeV$
^{37}Cl + ^{208}Pb ^{40}Ar + ^{205}Tl	^{132}Sn	^{65}Cu	^{48}Ca	134.52	129.17
	^{119}Sb	^{78}Ni	^{48}Ca	114.32	108.97
	^{132}Sn	^{73}Cu	^{40}Ca	116.87	111.52
	^{127}Sb	^{78}Ni	^{40}Ca	102.17	96.82
	^{151}Eu	^{78}Ni	^{16}O	60.01	54.66
	^{181}Lu	^{48}Ca	^{16}O	40.25	34.90
	^{132}Sn	^{56}Ni	^{57}Sc	97.65	92.30
^{40}Ar + ^{208}Pb	^{132}Sn	^{68}Zn	^{48}Ca	133.99	
	^{122}Te	^{78}Ni	^{48}Ca	111.88	
	^{132}Sn	^{76}Zn	^{40}Ca	116.91	
	^{130}Te	^{78}Ni	^{40}Ca	99.54	
	^{154}Gd	^{78}Ni	^{16}O	55.78	
	^{184}Hf	^{48}Ca	^{16}O	33.68	
	^{132}Sn	^{56}Ni	^{60}Ti	95.99	

Table 1.1: Major features of some TTF reaction channels.

TTF channels are shown in Table 1.1. It is remarkable that these channels have large positive Q-values, the positive implication of which is the higher velocity and energy ranges in the lab frame.

The choice of the first two reactions is necessary to evaluate the importance of the entrance channel in favoring the mass transfer toward TTF. In reaction 1, the target is a double magic nucleus and in reaction 2, none of the partners of the second reaction is a magic nucleus. Shell effects should be also considered in relation to the reaction time: nucleon transfer may be more facilitated by starting from nuclei without shell closures, and the second reaction may be more suitable for short reaction times typical of QF or multinucleon transfer. In other words, the relation between reaction time and nucleons rearrangements is a crucial point. Thus, the comparison between the first two reactions of the production rate may provide further information on the transfer probability in relation to the characteristics of the entrance channel. The third reaction is analyzed for different lab energies to build an excitation function.

The branching ratio of TF with respect to BF is a matter of controversy and being TF an

Reactions	E_{lab} (MeV)	$E_{c.m.}$ (MeV)	V_B (MeV)	Q_{fusion} (MeV)	E^*_{CN} (MeV)	ϑ^{lab}_{gr} (deg)
$^{37}Cl + {}^{208}Pb$	195	165	154	-120	45	103
$^{40}Ar + {}^{205}Tl$	193	161	160	-125	36	133
$^{40}Ar + {}^{208}Pb$	193	162	162	-129	33	139
$^{40}Ar + {}^{208}Pb$	230	193	162	-129	64	77

Table 1.2: Major entrance channel features of the reactions.

exotic process, theoretical and experimental understanding is not completely achieved. Such a study may help us, with a proper comparisons with models, to understand the conditions of the nucleus at scission and to provide important information on the role of the structure of the emerging fragments.

Given the reactions above, the bombarding energy was chosen according to the Coulomb barrier expected for the specific entrance channel. Some of the main entrance channel features are summarized in Table 1.2

1.4.1 Observables and detection geometry

A. Binary Fragments Detection

The observables of choice for these reactions are the velocity vectors of the binary fragments. Considering the two-body in-plane kinematics in Fig. 1.15, we plan to detect two fragments in the forward directions by placing two time of flight arms symmetrically around the beam (at 65°) at the folding angle for symmetric decay, following TKE Viola systematics. Asymmetric decays are also detected considering detector openings.

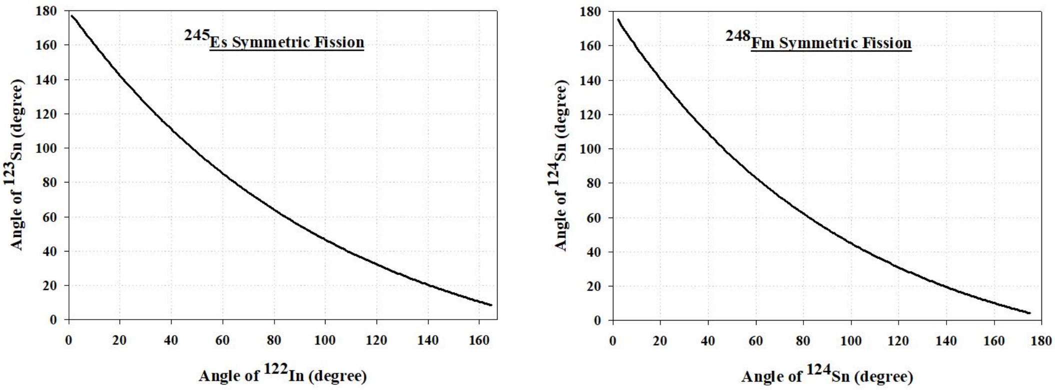

(a) *(b)*

Figure 1.15: Two body kinematics plot for symmetric fission: (a) for composite system ^{245}Es *produced by first two reactions and (b) for composite system* ^{248}Fm *produced by third reactions.*

The detection scheme of choice is shown in Fig. 1.16.

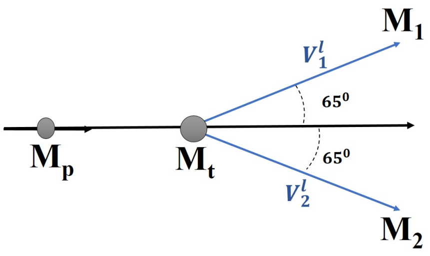

Figure 1.16: Proposed detection geometry for the binary decay.

B. Ternary Fragments Detection

Because of the types of detectors available, the observables of choice are the velocity vectors of two fragments and energy of the third one. Considering the three body in-plane kinematics in Fig. 1.17 (shown for first reaction), two fragments, with different masses, are detected at forward angles, at a folding angle smaller than the one of the symmetric fission, and the third fragment at the corresponding backward angle. It is important to remark that both arms in the forward hemisphere are placed at the same angle with respect to the beam, on the opposite side, because this establishes a strong constraint on the 3-body kinematics to eliminate overlap with sequential fission events (see later). Therefore, the detection scheme of choice is shown in Fig. 1.18. The kinematics calculation of direct ternary fission process are given in appendix A.

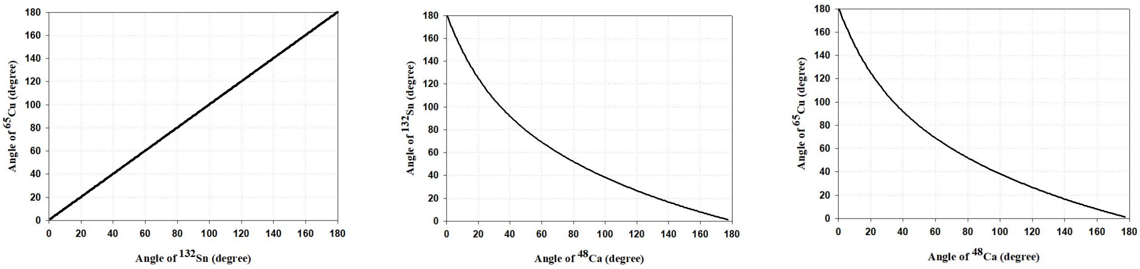

Figure 1.17: Three body kinematics plot of three body decay of interest for $^{37}Cl + {}^{208}Pb \rightarrow {}^{132}Sn + {}^{65}Cu + {}^{48}Ca$ *case.*

By taking advantage of the 3-body kinematics, events characterised by the coincidence between three detectors, two in the forward (at 40°) and one in the backward (at 100°), are considered candidate for a ternary decay. In fact, by measuring the velocity vectors of the two fragments in the forward hemisphere and the energy and the average angle of the backward emitted fragments we can extract an estimate of the masses of the three fragments.

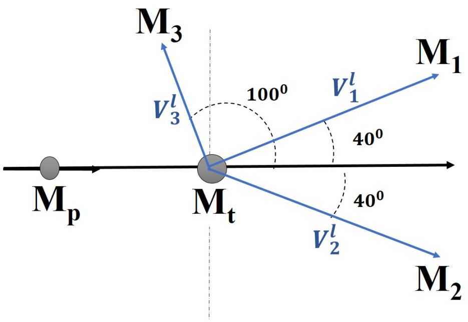

Figure 1.18: Proposed detection geometry for the ternary decay.

The triple coincidence geometry adopted can exclude all the ternary coincidences from the sequential fission (again three body in the final state) as it will be shown later. Furthermore, we can extract the branching ratio between the binary and ternary decay. A by-product of this setup is also the unknown mass distribution of ^{245}Es produced via two different entrance channels.

B.1 Energy and Angle Correlations:

It was very important to compute energy-angle correlations not only to setup correctly the dynamic ranges of the detectors, but also to avoid the overlap between direct (or simultaneous) breakup and sequential breakup. To our knowledge there are no data available on the energy of the fragments in 3-body decay except for the case in ref. [102] where an energy distribution peaked around 100 MeV for each of the three fragments was found in the reactions $^{40}Ar + {}^{238}U$ and $^{22}Ne + {}^{238}U$. Keeping this in mind and the large Q-value for tripartition in Table 1.1, we have computed the angular correlation between the fragments for various energies. The angular correlation of all three (^{132}Sn, ^{65}Cu, $and\,^{48}Ca$) fragments in terms of ^{48}Ca energy are plotted in Fig. 1.19.

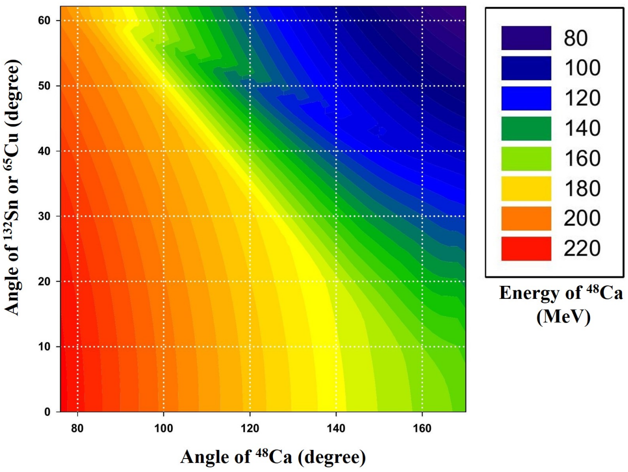

Figure 1.19: Angular correlation of three (^{132}Sn, ^{65}Cu, $and\,^{48}Ca$) fragments in terms of ^{48}Ca energy.

It is clear that ^{132}Sn and ^{65}Cu angles at 40^0 allow ^{48}Ca at different angles which are almost all in backward directions. Detection of ^{48}Ca at 100° results in an energy around 180

MeV. Therefore it is relatively easy to detect and identify the three fragments because of their high energy, which is also large enough to distinguish true ternary decay from all other three body decays, like the ones which involve α particles.

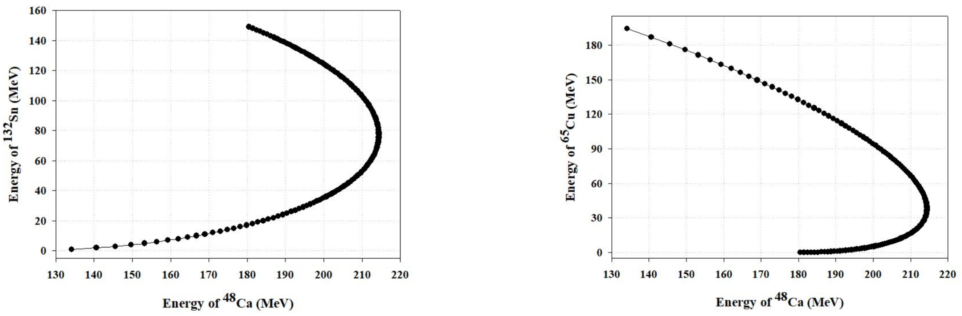

Figure 1.20: Possible double kinematics energy solution for ^{132}Sn and ^{65}Cu for a fixed energy of ^{48}Ca. The angles are refereed to the lab reference frame.

Anther important signature of a true three-body decay is the observation of multiple kinematics solutions. This is shown in Fig. 1.20. An optimal selection of detection geometry and dynamic ranges of the detectors are of great help to unequivocally identify a true three-body decay. This is the case of the geometry chosen in Fig. 1.18.

B.2 Sequential Three Body Decay:

The kinematics of a sequential 3-body decay is shown in Fig. 1.21. Because of the boost of the center of mass velocity the angular distribution is squeezed in the forward hemisphere.

From the diagram, 3-body sequential kinematics can be computed. For instance, first a two-body step into M_{23} and M_1 (^{113}In and ^{132}Sn) is supposed, and then in a second two-body step M_{23} (^{113}In) decays in M_2 and M_3 (^{65}Cu and ^{48}Ca). The angular correlations in this specific case are shown in Fig. 1.22. Without showing more plots, in all the cases explored there is no possibility that by kinematics or energy range a direct 3-body decay can be misidentified with a sequential one. The kinematics calculation of such process are given in appendix F.

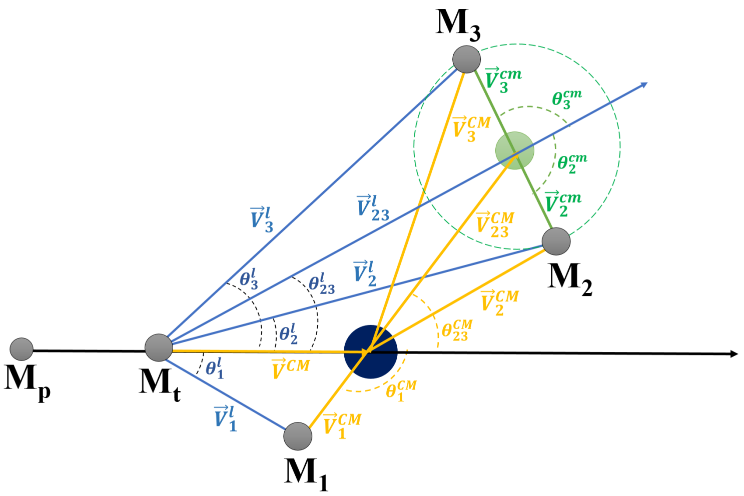

Figure 1.21: Velocity diagram for a 3-body sequential fission.

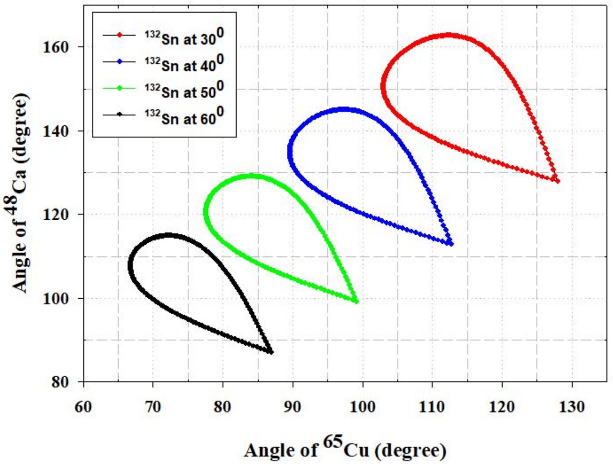

Figure 1.22: Angular correlations for a specific 3-body sequential fission.

Having in mind the mentioned kinematics relations, the plan is to use four TOF arms (two for binary at 65° and two for ternary decay at 40° on each side of the beam direction) from the 8π*LP*-CORSET setup [103] coupled with six 8π*LP* ΔE-E Telescopes. Telescopes were placed at the backward hemisphere, in-plane with the arms of the TOF spectrometer, three on each side of the beam, to cover the angular range between 100° and 160°. The high time and angular resolutions of the TOF spectrometers permitted the setting of a minimum TOF distance of (22 *cm*) that allows a mass resolution of 2-4 *amu* in the best operating conditions.

The working principle of the detectors used in the setup are illustrated in chapter 2 and the major features of the setup are given in appendix B. Besides that, Mass-Energy reconstruction for both binary (in section 3.3.1) and ternary fission (in section 3.3.2) are given in section 3.3.

1.5 Outline of the thesis

The thesis is structured according to the following scheme:

Chapter 2: Experimental Setup and DAQ system

It is mainly devoted to the experimental setup and data acquisition system. The working principle, data acquisition system, and features of actual setup of all detectors are discussed. At the end of the chapter, the method for mass-energy extraction is also given.

Chapter 3: Data Analysis

The procedure of detector calibration are explained for three different reactions. The first part is devoted to flight path and time-of-flight measurements. The methods of calculating masses, velocities, and Mass-energy distribution are also mentioned. The chapter ends by explaining the energy loss correction of the reaction fragments.

Chapter 4: Experimental Results

This chapter includes the most important experimental results in the binary and ternary channels.

Conclusions and Remarks:

Here the main results obtained are finally summarized. Highlights for future perspectives are also given.

Appendices:

Appendix A: The kinematics of direct ternary fission are presented.

Appendix B: All major features of the setup are explained briefly.

Appendix C: Calibration Parameters used to do data analysis are listed.

Appendix D: The potential energy are calculated for all conducted reactions for direct ternary fission case by using three cluster model.

Appendix E: The calculations for determining three masses in case of direct ternary fission are given.

Appendix F: The kinematics for sequential ternary fission are presented.

Chapter 2

Experimental Setup and DAQ system

2.1 Introduction

To study the dynamics of interaction between two heavy nuclei and the properties of collective motion of nucleons inside a nucleus, multidetector systems are typically used. In binary reactions, detection of both fragments provides the most important information about the interaction. Several methods have been used for fission fragments detection such as measuring the energies of coincident fragments (2E method) [104], measuring the velocities of coincident fragments (2V method), and measuring both energy and velocity of a single fragment (E-V method), measuring the energies and velocities of coincident fragments (2E-2V method). In the 2V method, the TOFs and positions of the two coincident fragments are measured. One important requirement is that the start detector of the TOF system must be so thin that the velocity of a detected particle flying through it varies within the narrowest limits. Ionization spark chambers having a much better energy resolution than semiconductor detectors are frequently used in measurements by the 2E method. However, these chambers are unsuitable for experiments with a charged particle beam due to a considerable increase in the background level and a high ionization of the working gas by bombarding particles. Gas-filled counters [105] have been also selected to perform these tasks. A drawback of gas-filled detector systems is that at least two thick foils are used in a start detector to isolate its gas volume from the vacuum volume of the reaction chamber. These foils lead to high energy losses, which needs to be corrected for, and multiple scattering of the detected particles with a consequential broadening of the position detected. The final result is usually a poor mass resolution.

By considering all the above mentioned setup and corresponding problems, the CORSET (CORelation SETup) [103] TOF spectrometer has been developed for detecting binary products. Four CORSET arms coupled with six ΔE - E Telescopes and beam monitoring system constitute the complete setup. The mounted experimental setup inside the scattering chamber is shown in Fig. 2.1. The schematic layout is shown in Fig. 2.2. The reasons for choosing such geometrical configurations were explained in the previous chapter in section 1.4.1.

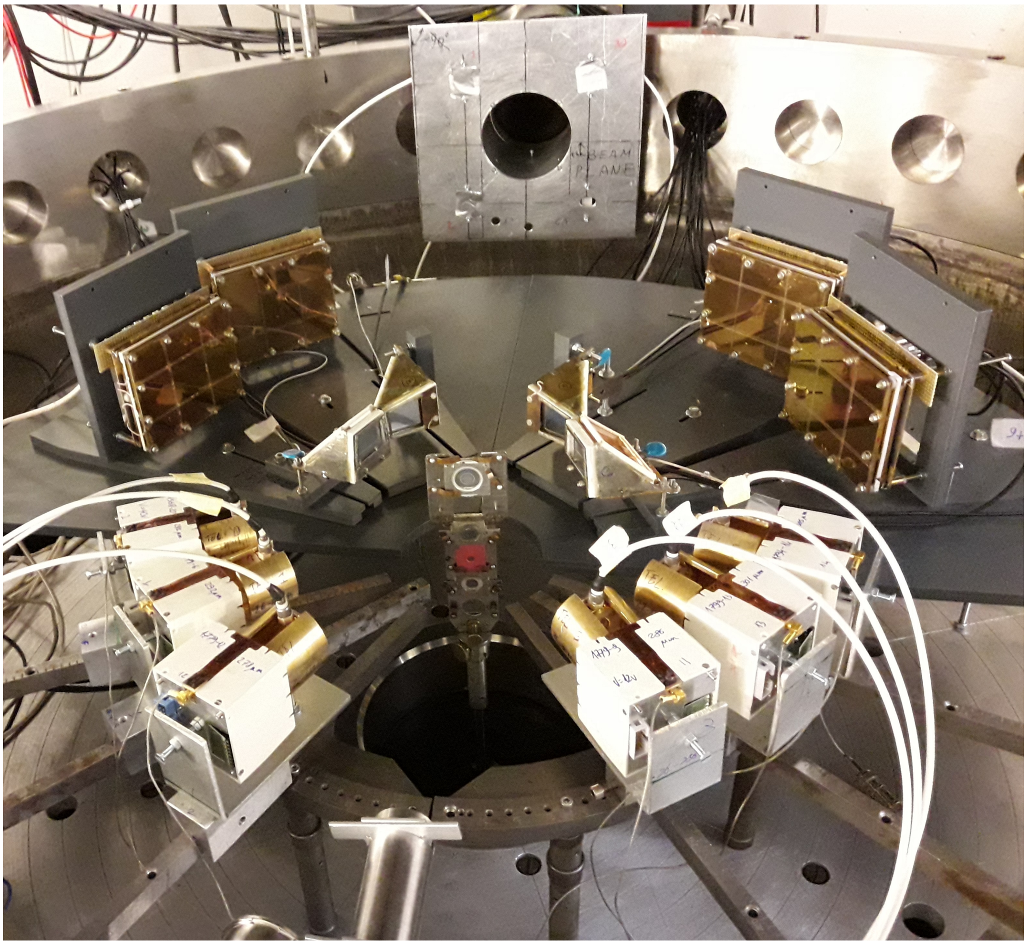

Figure 2.1: Complete experimental setup inside scattering chamber.

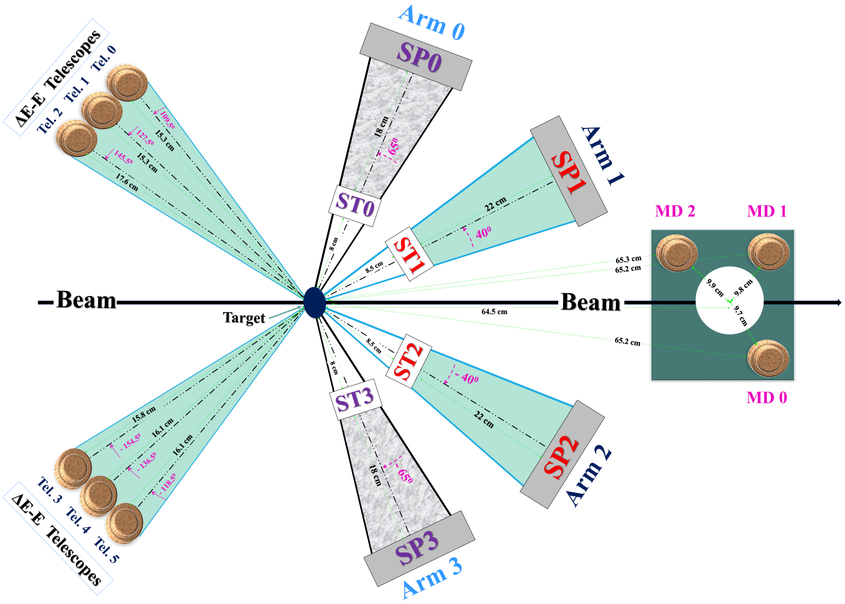

Figure 2.2: Layout of the experimental setup.

2.2 Detectors

The working principle of the TOF arm, particularly start and stop detectors, ΔE - E Telescopes, and beam monitoring system are briefly given below.

2.2.1 TOF Arm

Each TOF arm of the spectrometer consists of a compact Start detector (ST) and a position sensitive Stop detector (SP), both based on micro channel plates (MCP) (Fig. 2.3). Depending on the reaction under investigation, the arms can be positioned at different angles with respect to the beam axis. The distance between the start and stop detectors of each arm (the flight path) usually ranges from 10 to 25 cm, and the distance from the start detector to the target is usually around 3 to 5 cm. In the typical operating conditions, the time resolution is between 100 - 150 ps and the angular resolution is 0.3°. These time and angular resolutions

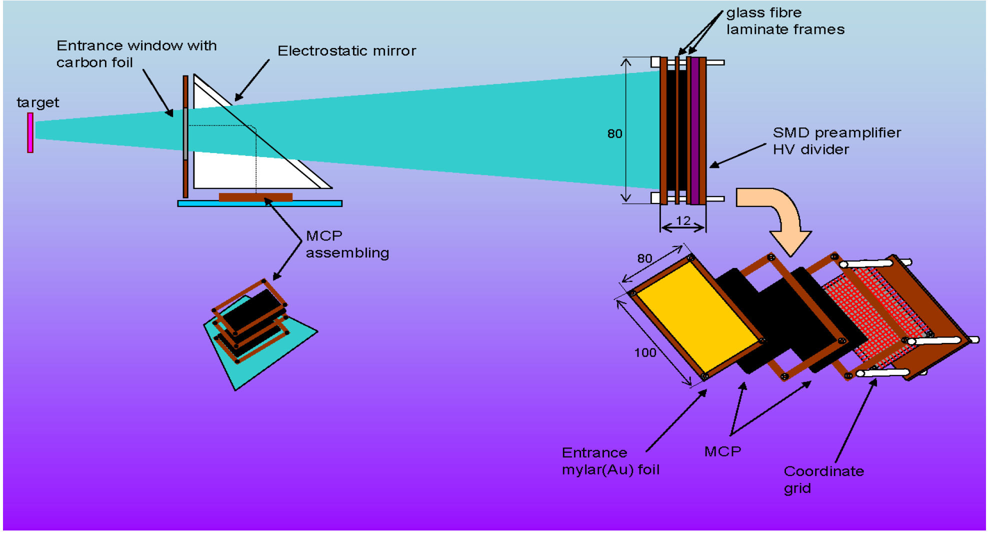

Figure 2.3: A CORSET arm consists of a Start and a Stop detectors.

of the spectrometers permit the setting of minimum time-of-flight (TOF) distance without significant deterioration of the mass resolution. With a TOF distance of 20 cm, it is possible to reach 2 to 3 amu of mass resolution.

By measuring the time of flight and the position hit by the ion on the stop detector it is possible to reconstruct the velocity vector of the impinging ion by using trivial geometrical transformations. Corrections are applied for the energy lost by the ion in the entrance window. Since the mass and charge of this ion is unknown, a recursive procedure is used by applying the two-body kinematics as explained later on. In any case, the thickness of the entrance foil of the start detector (see next section) is chosen so to make this correction negligible enough.

Start Detector with an Electrostatic Mirror

The start detector consists of a conversion foil, an accelerating grid, an electrostatic mirror, and a chevron assembly of two MCP [106]. The real image and schematic diagram of the detector is presented in Fig. 2.4. A Mylar foil (70-150 $\mu g/cm^2$ thick) sputtered with gold or aluminum (20-30 $\mu g/cm^2$ thick) is used as a electron conversion foil at the entrance of

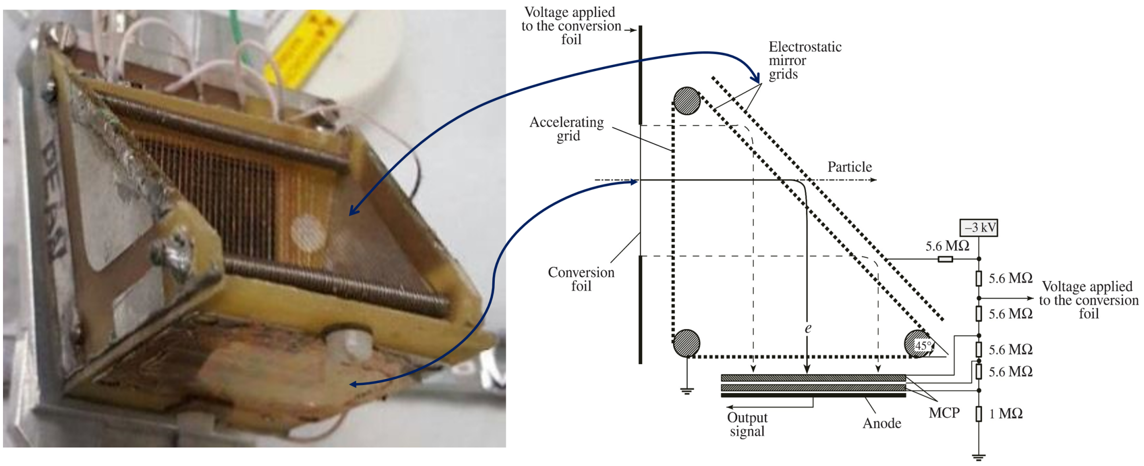

Figure 2.4: Picture and schematic diagram of the start detector with an electrostatic mirror.

the start detector. Mylar is sputtered for increasing the secondary yield of electrons. When the reaction fragments pass through the conversion foil they knock out electrons which are subsequently accelerated up to ~3 keV. Electrons are accelerated in the electric field between the foil and accelerating grid. Then these electrons are deflected by electrostatic mirror grid at 90° and finally they hit the chevron MCP assembly. Electrons generated from any points of the conversion foil passes the same distance up to the MCP assembly that makes the output signals position independent.

It is a matter of attention to consider that when fragments passes through the conversion foil, it may slightly change its velocity as well as direction. Therefore, one must take into account the energy lost by a particle in its passage through the conversion foil. Indeed the energy loss are usually around few MeV which is 2-5% of the initial energy, and the smearing in the particle direction due to multiple collisions with the atoms of the foil falls within the position resolution of the Stop detector and therefore it is usually neglected. A high voltage divider is used to supply the voltages for the MCP, the conversion foil, and the grids of the electrostatic mirror. All major features of start detectors used in the setup are given in section B.1 of Appendix B.

Position-Sensitive Stop Detector

The Stop detector consists of a conversion entrance foil, a chevron assembly of two MCPs [106], a coordinate system, and a printed circuit board with fast amplifiers for one timing signal and two coordinate signals. The photograph and schematic diagram of the detector are shown in Fig. 2.5. Mylar foil (70-150 $\mu g/cm^2$ thick) sputtered with gold or aluminum (30-40 $\mu g/cm^2$ thick) is used as a conversion foil. The operating voltage is applied to the plates by foil-clad glasscloth laminate frames with contact pads by which MCPs are attached. A high-voltage divider is used to supply the high voltage (~1 kV) to the MCPs and deliver the necessary potentials for the coordinate system and the conversion foil.

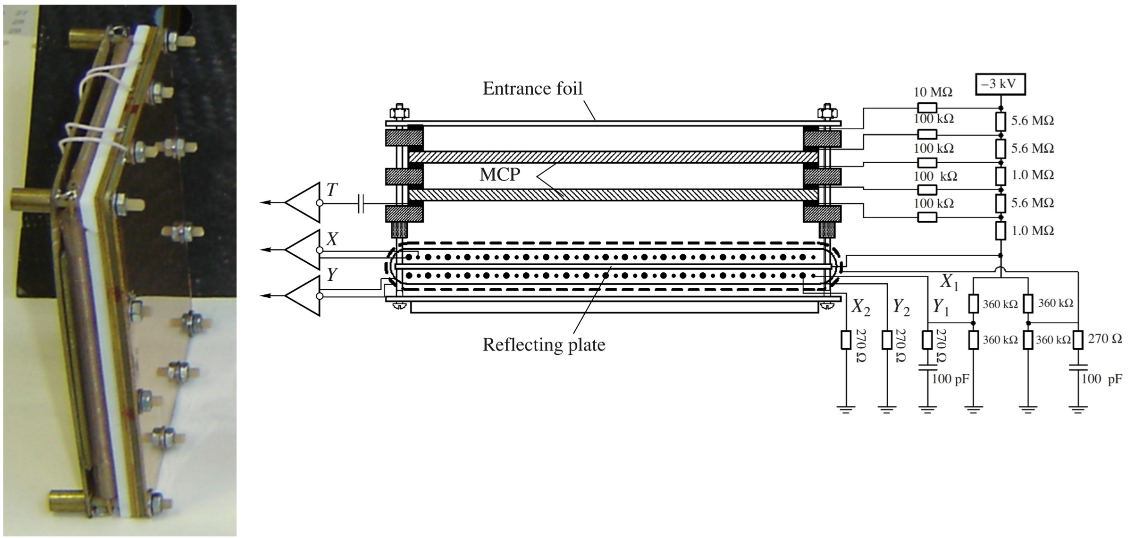

Figure 2.5: Schematic diagram of the MCP-based position-sensitive stop detector.

The coordinate system consists of two mutually perpendicular wires that act as delay lines. Each coordinate is composed of two independent delay lines shifted by 0.5 mm with respect to each other. The potentials applied to the delay lines are selected so that electrons escaping from the MCP are collected on only one of them. The other delay line (which does not collect electrons) is used to compensate for the interference of the fast timing signal from the exit surface of the MCP. The coordinate of a particles hit point at the detector is determined from the difference in the arrival time of the timing signal and the signal from the relevant delay line. The circuit design of the preamplifiers for two coordinate signals is similar to that in [107]. All major features of stop detectors used in the setup are given in section B.1 of Appendix B.

Micro Channel Plate (MCP): Micro channel plates are compact electron multipliers of high gain. They have been used in a wider range of particle and photon detection systems. It is an array of $10^4 - 10^7$ miniature electron multipliers channels oriented parallel to one another. The channels of each MCP are tilted (8° - 15°) against the MCP normal and the channels of successive MCPs are tilted to opposite directions. Such a configuration of two MCPs is called chevron configuration. All CORSET Start and Stop detectors have two MPCs in a chevron assembly [106] for increasing electron multiplication. The MCP used have a channel width of $15\mu m$, a channel-to-channel distance of $18\mu m$, and a thickness of 1 mm ± 0.1 mm.

2.2.2 ΔE - E Telescopes

For the detection of charged particles in the backward, the ΔE - E combination of surface barrier detector (SBD) was used. A thin SBD coupled with thick SBD makes a telescope that can allow to identify the particles by energy loss method. In a telescope, thin SBD are placed upstream the thick one. So particles first pass through thin detector and lose some energy (ΔE), for that this detector is mentioned as a ΔE detector. After passing through ΔE detector, particles stops in the thick detector (E-detector) which measures the residual energy (E). The detected particles can be identified by the two methods : the energy loss-residual energy (ΔE-E) and energy loss ΔE-Time(T) correlation plot. A series of ΔE - E Telescopes are shown in Fig. 2.6. All major features of ΔE - E Telescopes used in the setup are given in section B.2 of Appendix B.

Figure 2.6: Six E - ΔE Telescopes used in the backward beam direction.

2.2.3 Monitor Detectors

The surface-barrier detectors were used for monitoring the quality of the beam, its position on the target and to normalize the event numbers to cross section. SBD register beam ions that are elastically scattered by target nuclei. The detectors are conventionally installed in the order top-bottom- right-left, at angles of 90° with respect to each other and 8° – 17° with

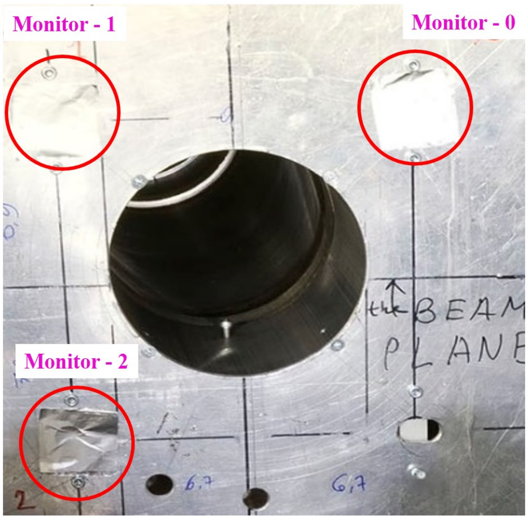

Figure 2.7: Three monitor detectors placed in front of the setup.

respect to the beam axis. Knowing the counting rates of elastically scattered ions for each of the detectors and comparing them to the values calculated from the Rutherford elastic scattering, one can extract the average point of incidence of the beam onto the target. Events from the monitoring detectors are recorded in parallel with all the other event types by a common data acquisition system. Measuring the counting rates and the energy spectra of scattered beam ions, it is possible to monitor both the beam position and energy. Three silicon detectors were used in the positions shown in Fig. 2.7. All major features of monitor detectors used in the setup are given in section B.3 of Appendix B.

2.3 Signal Processing and Data Acquisition System

2.3.1 Electronic Chain for CORSET

The block diagram of the four-arm TOF spectrometer is shown in Fig. 2.8. Each Start detector has two inputs (*+6V* and High Voltage (*HV*)) and one output (*St*). Each Stop detectors have three inputs (*-6V*, *+6V*, and High Voltage (*HV*)) and three outputs (*X*, *Y*, *Sp*).

All the timing and coordinate signals from the Start and Stop detectors (St_0, Sp_0, X_0, Y_0, St_1, Sp_1, X_1, Y_1, St_2, Sp_2, X_2, Y_2, St_3, Sp_3, X_3, and Y_3) are fed into constant-fraction discriminators (CFDs). After CFD, start and stop signals go to time-to-amplitude converters (TACs) and then to analog-to-digital converters (ADCs). The following time intervals were measured by using these TAC-ADC converters:

- TOF0: time intervals between the arrival of St_0 and Sp_0,
- TOF1: time intervals between the arrival of St_1 and Sp_1,
- TOF2: time intervals between the arrival of St_2 and Sp_2, and
- TOF3: time intervals between the arrival of St_3 and Sp_3.

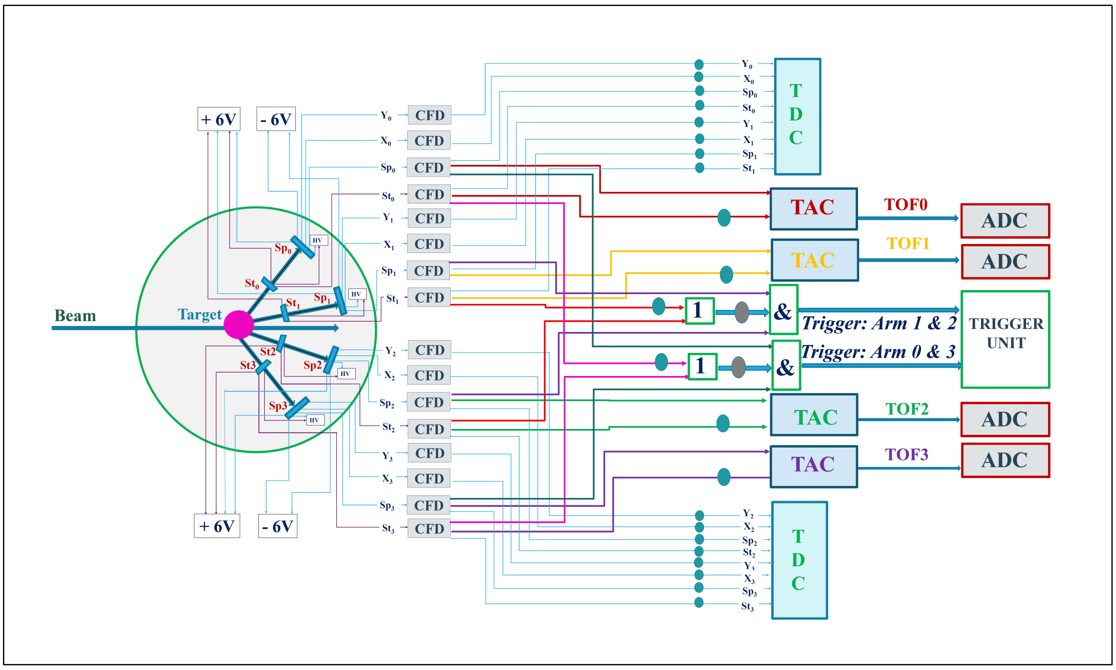

Figure 2.8: Block Diagram of the CORSET.

Furthermore, the following time intervals (not shown in Fig. 2.8) were also measured by the TAC-ADC converters:

- TOFL0: time intervals between the arrival of St_3 and Sp_0,
- TOFL1: time intervals between the arrival of St_2 and Sp_1,
- TOFL2: time intervals between the arrival of St_1 and Sp_2,
- TOFL3: time intervals between the arrival of St_0 and Sp_3,
- ΔT_{St03}: time intervals between the arrival of St_0 and St_3,
- ΔT_{St12}: time intervals between the arrival of St_1 and St_2,
- ΔT_{Sp03}: time intervals between the arrival of Sp_0 and Sp_3, and

- ΔT_{Sp12}: time intervals between the arrival of Sp_1 and Sp_2.

The start and stop signals (timing signals) as well as the coordinate signals, are independently transmitted via delay lines to a time-to-digital converter (TDC) that are in common start mode. The trigger signal acts as the start signal for the TDC. Once calibrated, the TDC output can be used to measure the time interval between any input signal.

Channel	Input	Channel	Input
0	SP0	9	SP3
1	X0	10	X3
2	Y0	11	Y3
3	SP1	12	ST0
4	X1	13	ST1
5	Y1	14	ST2
6	Sp2	15	ST3
7	X2	22	Trigger on Arm0 & 3
8	Y2	23	Trigger on Arm1 & 2

Table 2.1: CORSET Parameters connected to TDC.

In this way, the position of the particles can be measured as differences:

- X_0 = TDC_X_0 - TDC_Sp_0,
- Y_0 = TDC_Y_0 - TDC_Sp_0,
- X_1 = TDC_X_1 - TDC_Sp_1,
- Y_1 = TDC_Y_1 - TDC_Sp_1,
- X_2 = TDC_X_2 - TDC_Sp_2,
- Y_2 = TDC_Y_2 - TDC_Sp_2,

- X_3 = TDC_X_3 - TDC_Sp_3, and
- Y_3 = TDC_Y_3 - TDC_Sp_3.

The connection of start and stop signals (timing signals) as well as the coordinate signals and generated trigger connected with TDC are shown in Table 2.1.

2.3.2 Electronic Chain for ΔE - E Telescopes and Monitors

The block diagram of six ΔE - E telescopes and three monitors is shown in Fig. 2.9. The detector signals are fed into preamplifiers, then signals go to amplifiers. Each Amplifier generates two output signals, one is spectroscopic (slow) output and another is fast output. Then, all spectroscopic signals are fed into ADCs. The ADC gate, set to 12μs, considering the integration time constant of the spectroscopic amplifier, is generated by the master trigger signal (see later) via a dual timer module (not shown in Fig. 2.9).

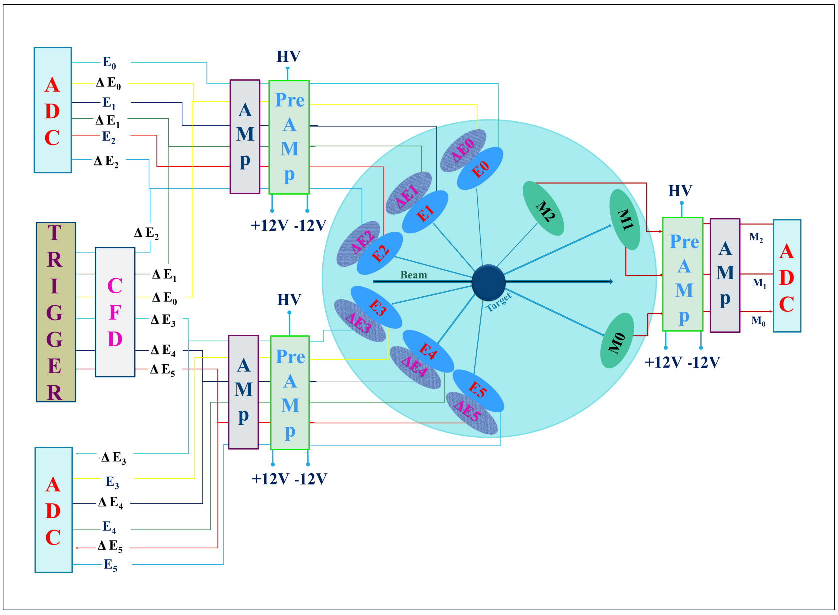

Figure 2.9: Block Diagram of the E - ΔE Telescopes and Monitors.

The connection of six ΔE - E telescopes and three monitors signals to the ADCs are shown in table 2.2.

Channel	Input	Channel	Input
0	ΔE0	8	E2
1	ΔE1	9	E3
2	ΔE2	10	E4
3	ΔE3	11	E5
4	ΔE4	12	Monitor 0
5	ΔE5	13	Monitor 1
6	E0	14	Monitor 2
7	E1		

Table 2.2: Telescopes and Monitors connected with ADC.

2.3.3 Trigger for Acquisition System

The trigger signals were generated by taking into account the expected physics cases. For binary reactions, we required the AND between Arm0 and Arm3. For the detection of two of the fragments produced in ternary decay, we required the AND between Arm1 and Arm2 keeping the ΔE-E telescopes as slaves in order to benefit of the larger solid angles of the arms. This with the aim to increment the statistics of two out of three fragment events.

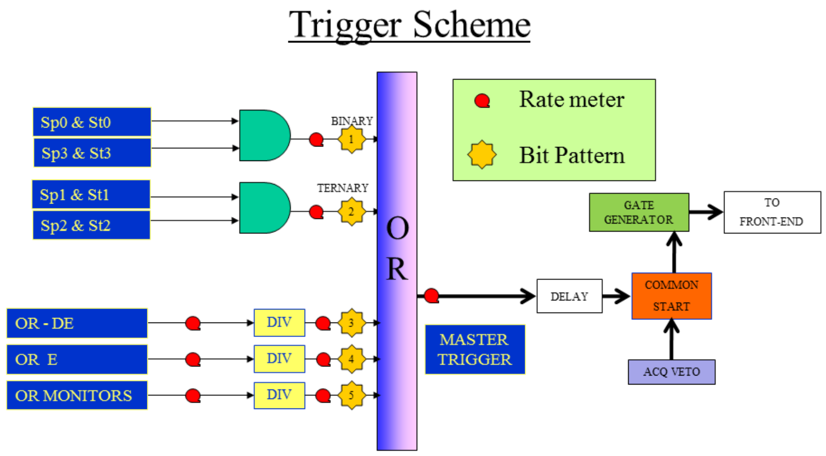

Figure 2.10: Block Diagram of the trigger logic.

Having this in mind, the block diagram of the trigger logic is given in Fig. 2.10. Fast outputs from each ΔE and E detectors act as a trigger for single measurements and as slave for coincidence events. The singles events (OR-ΔE, OR-E, OR- MONITORS) are downscaled to reduce their original rate much higher than the coincidence rate. The master trigger is sent to a fan out module to spread the signal across the front-end modules, namely the ADCs and TDCs. The ADC gates are generated from the master trigger signal via a gate generator device.

Chapter 3

Data Analysis

3.1 Detector Calibration

Micro channel plate based position sensitive stop detectors are used in CORSET arms to determine position information of the reaction fragments. From position and time-of-flight, the components of the velocity vector are obtained. The Stop detector provides time intervals that are converted to position (X_{mcp}, Y_{mcp}) of the point where fragments hit the detector after time and position calibration. To calibrate positions from the raw time signals, four plastic stripes are attached on the front foil (shown in Fig. 3.1). Considering the center of the foil as the origin point, the horizontal (X) edge goes from $+43\,mm$ to $-43\,mm$ and the vertical

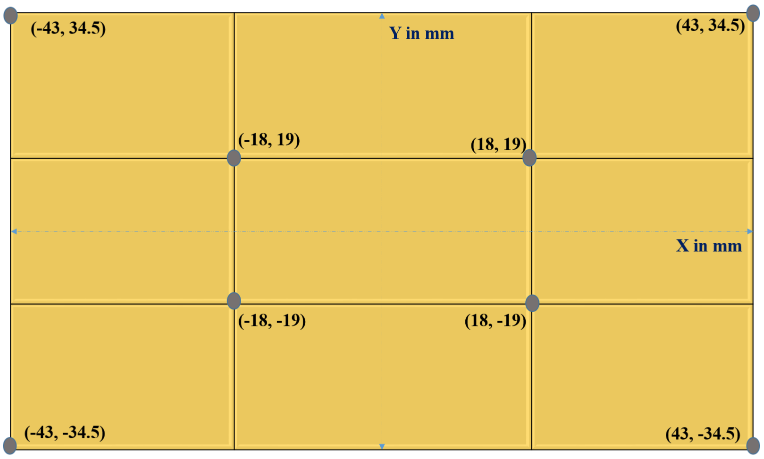

Figure 3.1: Position of the calibration points on the foil layer of MCP.

(Y) edge goes from +34.5 *mm* to −34.5 *mm*. In Fig. 3.1, there are eight known points (in *mm*) that can be correlated to the raw data. These points are same for all CORSET arms and the same calibration process is applied for all arms. All the calibration parameters (slopes and intercepts) are calculated by linear regression method are presented in Appendix C.

The expressions for calibrated positions are written in the following way:

$$\mathrm{X_{mcp}} = \mathrm{Slope\,(mm/ch)} \times \mathrm{Channel_X} + \mathrm{Intercept\,(mm)} \;\text{ and}$$

$$\mathrm{Y_{mcp}} = \mathrm{Slope\,(mm/ch)} \times \mathrm{Channel_Y} + \mathrm{Intercept\,(mm)}\,.$$

3.1.1 Flight Path Measurements

Let us consider that a reaction fragment hits at point P on the MCP of the stop detector (schematic representation given in Fig. 3.2). In the figure, L_{st} and L_{sp} are the distances of Start and Stop detectors from target. S_i is the flight path of the fragment between Start and Stop detectors (where $i = 1, 2, 3, ...$).

In order to obtain the velocity of each fragment flying in CORSET arms, it is necessary to compute the flight path of the fragments. Position-sensitive detectors provide the velocity vector and the trajectory length of the fragments in a lab reference frame in which the target

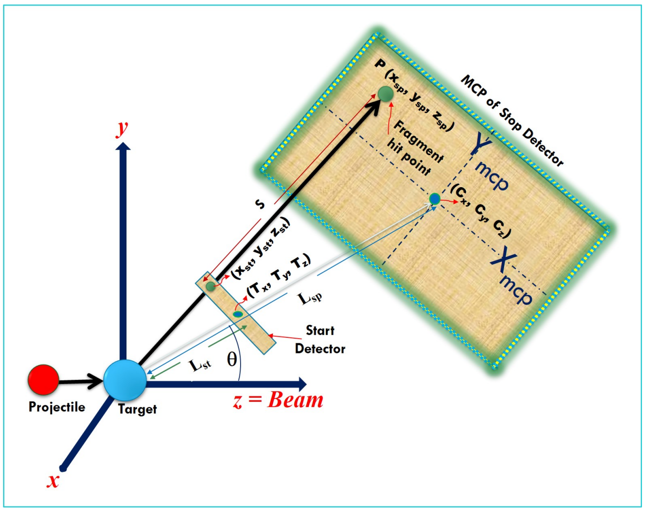

Figure 3.2: schematic diagram of the MCP of stop detector when fragment hits at point P.

Start detector center coordinates	(T_x, T_y, T_z)	$(0, L_{st}\, sin\theta_i, L_{st}\, cos\theta_i)$
Stop detector center coordinates	(C_x, C_y, C_z)	$(0, L_{sp}\, sin\theta_i, L_{sp}\, cos\theta_i)$

Table 3.1: Main parameters used to calculate fight paths.

is at the origin and the beam lies on the z axis. The x axis coincides with the vertical one and the y axis is set to obtain a right-handed reference frame. The main parameters used to obtain the position of the hit point (P) on the detectors are presented in Table 3.1. The position of the hit point on each Stop MCP is given by the following equations:

$$\begin{aligned} x_{sp} &= C_x + Y_{mcp}\,, \\ y_{sp} &= C_y + X_{mcp}\, cos\theta\,, \\ z_{sp} &= C_z + X_{mcp}\, sin\theta\,, \end{aligned}$$

where X_{mcp} and Y_{mcp} are the coordinates (calibrated) of the fragment onto the detecting surface; X_{mcp} is the horizontal position of the fragment on the MCP, Y_{mcp} is the vertical one. From the equation of the straight line between the center of the target and the hit point and the intersection with the start detector plane, it is possible to determinate the coordinates of the hit point on the start detector:

$$\begin{aligned} x_{st} &= \frac{T_x^2 + T_y^2}{T_x x_{sp} + T_y y_{sp}} x_{sp}\,, \\ y_{st} &= \frac{T_x^2 + T_y^2}{T_x x_{sp} + T_y y_{sp}} y_{sp}\,, \text{ and} \\ z_{st} &= \frac{T_x^2 + T_y^2}{T_x x_{sp} + T_y y_{sp}} z_{sp}\,. \end{aligned}$$

The flight path of the fragments is:

$$S_i = \sqrt{(x_{sp} - x_{st})^2 + (y_{sp} - y_{st})^2 + (z_{sp} - z_{st})^2}. \tag{3.1.1}$$

3.1.2 Time-of-Flight (TOF) Measurements

The Time-to-Amplitude-Converter (TAC) is used to measure the time interval between two pulses named the start and stop signals. The output is a signal whose height is proportional

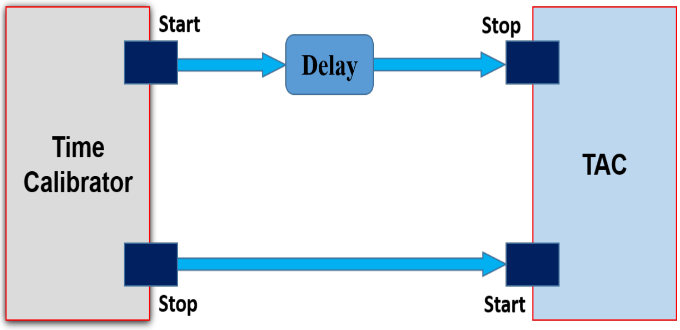

Figure 3.3: Schematic representation of TAC connected with time calibrator.

to the time interval between the start and the stop signals. Therefore, such a TAC output pulse need to be calibrated. To this aim, a time calibrator pulse generator is used. The two pulses that are fed to the TAC are the Start and the Stop output generated from the time calibrator. Generally, there are some delays added in order to avoid the mixing of rapid arrivals of signals, which later are converted to output pulses. Different delays (in *ns*) and corresponding output pulse (in channels, arbitrary units) yield the calibration parameters,

$$\text{slope (ns/ch)} = \text{delay / (difference in channel number)}\,. \tag{3.1.2}$$

With a time calibrator only the slope of the calibration straight line can be obtained. To obtain the intercept a physical event is necessary. For this purpose the elastic scattering peaks were used. The flight times are calculated by elastic kinematics and assigned to the elastic scattering peaks of each fragment from the measured event. To identify the elastic peaks to be assigned to the two elastically scattered ions (the projectile and the target) and their flight path length the two body kinematics is applied.

Let us consider the elastic scattering for the ^{37}Cl + ^{208}Pb reaction. At 195 MeV of beam energy, if Cl is deflected at laboratory angle $\theta_{lab} = 56.1^\circ$ with respect to the beam direction, Pb is deflected at laboratory angle $\theta_{lab} = 57.7^\circ$ on the opposite side of Cl. These angles are covered by the CORSET Arm0 and Arm3. As a result, Cl flies 27.1 cm and Pb flies 27.3 cm from the target when these are detected in CORSET Arm0 and Arm3, respectively. Hence,

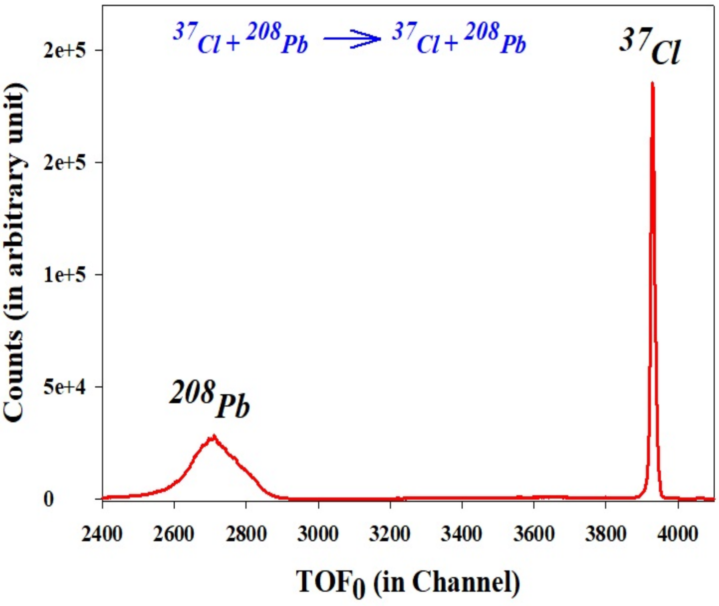

Figure 3.4: Peaks for TOF_0 from elastic scattering between Cl + Pb in Arm0.

the proper time (t_p) taken by the fragments (in *ns*) can be calculated by the relation,

$$t_p = \frac{\text{distance}}{0.98\ \sqrt{2E/M}},$$

where E and M are energy (in MeV) and mass (in amu), respectively, and 0.98 is a conversion factor. Therefore, the estimated proper times for *Cl* and *Pb* are 9.2 *ns* and 53.2 *ns*, respectively. It is clear that *Pb* takes longer time comparatively *Cl*. These two times are assigned to the raw time interval measured with the TAC (in channel number) and the calibration is now completed.

The elastic scattering peaks for *Cl* and *Pb* are shown in Fig. 3.4. It is important to note that the start and stop input signals of the TAC are fed in such a way that the start (stop) input corresponds to the signal Stop (Start) of each arm. This is because the rate of the Start signal is much bigger that the rate of the Stop signal. With this switch it is possible to avoid a large number of start without the stop, namely, reduce the dead time. For this method to work, it is necessary to delay the arm Start signal with respect to the Stop arm signal. The consequence is that the time scale is reversed, namely, faster fragments show larger time. In

Nuclei	Time (ns)	Channel (arb. unit)
Chlorine (Cl)	9.2	3929
Lead (Pb)	53.2	2706

Table 3.2: Parameters of elastic scattered Cl and Pb in Arm0.

other words, the time increases from right to left of the spectra. Therefore the leftmost peak indicates the longer time i.e., *Pb*; the rightmost peak indicates the shorter time i.e., *Cl*. The channel numbers and corresponding real times calculated for both fragments are shown in Table 3.2. The intercept parameter is calculated by linear regression method for the values of the Tables 3.2, where slope is used from equation 3.1.2. Similarly, calibration parameters are calculated for other CORSET arms. The calibration parameters of four CORSET arms for three different reactions are presented in Table C.5 of Appendix C. The expression for calibrated TOF for CORSET arms is:

$$\mathrm{TOF_i} = \mathrm{Slope\,(ns/ch)} \times \mathrm{Channel_{TOF}} + \mathrm{Intercept\,(ns)}\,. \tag{3.1.3}$$

3.1.3 ΔE - E of Telescopes

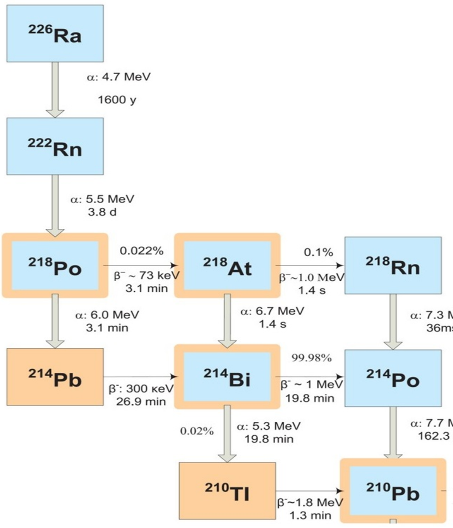

Figure 3.5: The decay series of ^{226}Ra (from [108]).

The most stable isotopes of Radium, alpha particle emitter, ^{226}Ra ($T_{1/2}$ = 1600 year), has been used for the energy calibration purpose. ^{226}Ra decays to stable nuclide ^{206}Pb through a chain of 13 α and β emitters [108]. From this decay chain, first four α decays have been considered for calibration (see Fig. 3.5).

The spectra obtained from ^{226}Ra source, detected at telescope 3 are presented in Fig. 3.6, where Silicon detectors having thicknesses 18.7 μm and 286 μm are placed as a ΔE and E detectors respectively (details in section B.2). When particles pass through ΔE detector, they loose some energy. With the residual energy, they are detected at E detector. So total energy of particles is the sum of energies detected by two detectors. The spectra of energy loss of α particles at ΔE detector are given at Fig. 3.6b. The spectra of the residual energy of α particles detected at E detector are given at Fig. 3.6a.

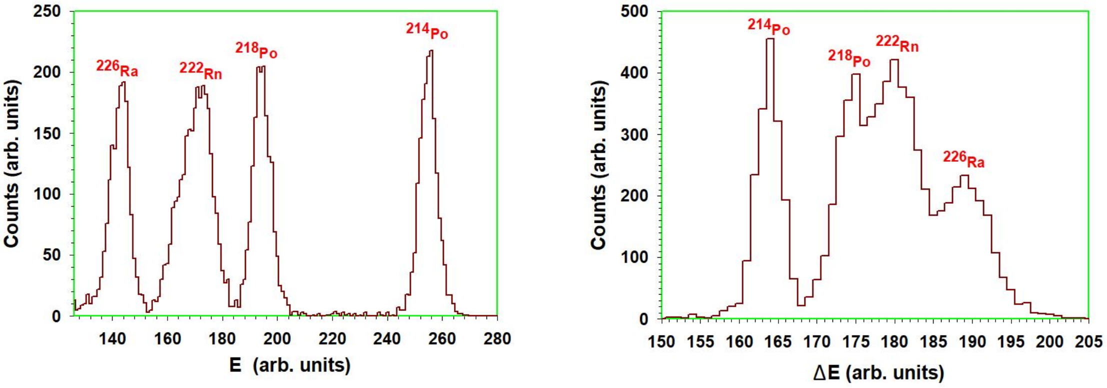

(a) *(b)*

Figure 3.6: Alpha energy raw spectra: (a) for E detector and (b) for ΔE detector.

In the spectrum, the emission peaks of Radium 226 (4.75 MeV), Radon 222 (5.45 MeV), Polonium 218 (5.95 MeV) and Polonium 214 (7.65 MeV) are indicated. The energies at detectors with associated channel numbers are given in Table C.6 and Table C.7 of Appendix C. The calibration parameters (slopes and intercept) are calculated by using linear regression method for the values of the table C.6 and C.7. The parameters are presented in the Table C.8 of Appendix C for two detectors of telescope 3.

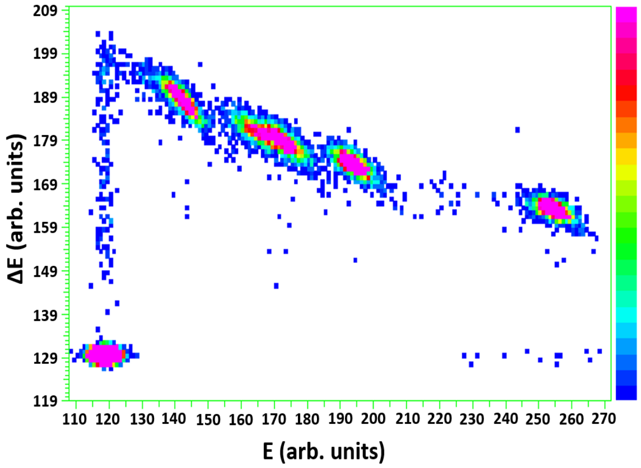

Figure 3.7: E-ΔE matrix of raw data from alpha source.

The expression for Energy calibration for Telescopes is:

$$E_i = \text{Slope}\,(\text{MeV/ch}) \times \text{Channel}_E + \text{Intercept}\,(\text{MeV})\,. \tag{3.1.4}$$

The calibrated energy spectra of α particles in E and ΔE detectors are shown in Fig. 3.8. Furthermore, the ΔE-E matrix of calibrated energy are presented in Fig. 3.9.

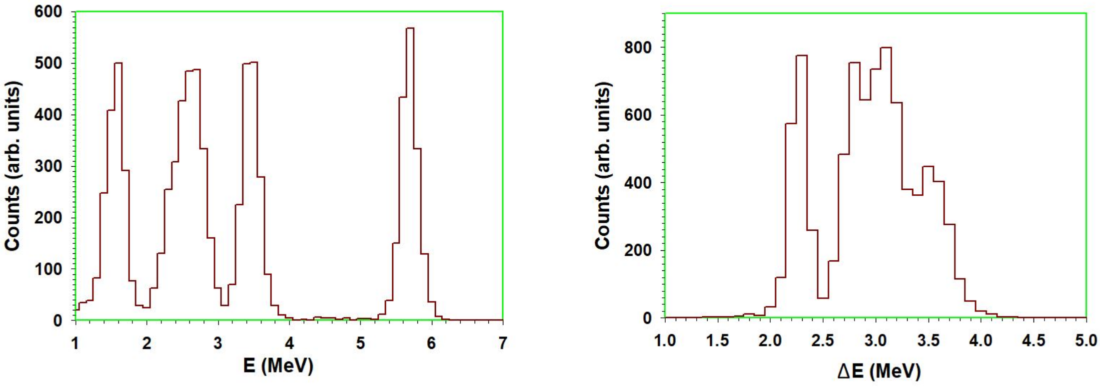

(a) *(b)*

Figure 3.8: Alpha energy calibrated spectra: (a) for E detector and (b) for ΔE detector.

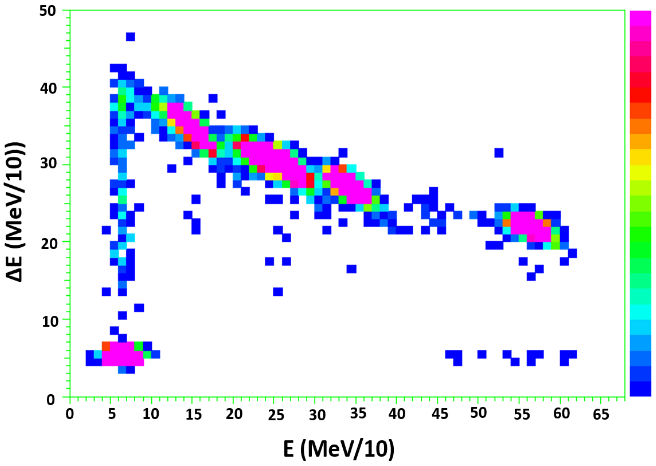

Figure 3.9: E-ΔE matrix of calibrated data from alpha source.

3.2 Velocity Calculations

The module of each fragment velocity vector detected in the TOF arms is given by:

$$V_i = \frac{S_i}{TOF_i}. \tag{3.2.1}$$

3.3 Mass-Energy Calculations

3.3.1 Binary Reaction: Mass-TKE

Analysis of experimental data was based on measuring the velocity vectors of two reaction products in the forward direction. To determine the mass and the energy of fission fragments, the momentum and mass conservation laws are used and provide the following expressions for the two masses:

$$M_1 = \frac{(M_p + M_t)V_2 sin\theta_2}{V_1 sin\theta_1 + V_2 sin\theta_2}, \tag{3.3.1}$$

$$M_2 = M_p + M_t - M_1, \tag{3.3.2}$$

Here V_1 and V_2 are the measured velocities of binary fragments 1 and 2 by two CORSET TOF arms placed in the forward (at laboratory angle $\theta_{lab} = 65°$) direction, respectively. M_p, M_t, M_1, and M_2 are the masses of projectile, target, fragment 1,and fragment 2 respectively. It is important to remark that because of eq. 3.3.2, M_1 and M_2 are the primary masses just after the splitting of the compound system in two fragments.

When masses are expressed in *amu* unit and velocities in *cm/ns* unit, the total kinetic energy (TKE), namely the sum of the energies of the two fragments in the center of mass system, is given by:

$$TKE = \sum_{i=1}^{2} E_{i,cm} = 0.52 \sum_{i=1}^{2} M_i V_{i,cm}^2, \tag{3.3.3}$$

where, TKE and $E_{i,cm}$ are in *MeV* unit, and 0.52 is a conversion factor.

$$V_{i,cm} = \left[V_i^2 + V_{cm}^2 - 2\, V_i\, V_{cm}\, cos\theta_i\right]^{1/2}, \text{and} \tag{3.3.4}$$

$$V_{cm} = \frac{\sqrt{2E_{lab}M_p}}{M_p + M_t}. \tag{3.3.5}$$

3.3.2 Ternary Reaction: Mass-TKE

In the present case only the planar geometry is considered. The energy and momentum conservation conditions onto the beam axis and the axis perpendicular to the beam direction give:

$$\begin{aligned} E_{lab} &= M_1 V_1^2 + M_2 V_2^2 + E_3 - M_p - M_t + M_1 + M_2 + M_3\,, \\ M_p V_p &= M_1 V_1\, cos\theta_1 + M_2 V_2\, cos\theta_2 + \sqrt{2M_3E_3}\, cos\theta_3\,, \; and \\ 0 &= M_1 V_1\, sin\theta_1 + M_2 V_2\, sin\theta_2 + \sqrt{2M_3E_3}\, sin\theta_3\,. \end{aligned}$$

There are 9 unknowns variables (θ_1, θ_2, θ_3, V_1, V_2, E_3, M_1, M_2, M_3) in the above 3 equations. By measuring 6 of them (θ_1, θ_2, θ_3, V_1, V_2, E_3), we obtain the 3 masses M_1, M_2, and M_3. V_1 and V_2 were calculated in coincidence by two CORSET TOF arms placed in the forward hemisphere (at laboratory angle $\theta_{lab} = 40°$) and E_3 was calculated from ΔE-E telescopes placed in the backward hemisphere at known angles. This method is enough to unequivocally identify a direct three body decay with a simple detection geometry and with a set of well known detectors of very high performance. The detailed calculation is given in Appendix E.

When masses are expressed in *amu* unit and velocities in *cm/ns* unit, the expression for total kinetic energy (TKE) becomes:

$$TKE = \sum_{i=1}^{3} E_{i,cm} = 0.52 \sum_{i=1}^{3} M_i V_{i,cm}^2, \tag{3.3.6}$$

where, TKE and $E_{i,cm}$ are in MeV units, and 0.52 is a conversion factor. $V_{i,cm}$ and V_{cm} were calculated by equations 3.3.4 and 3.3.5 respectively.

3.4 Energy Loss Corrections

A fragment that passes through a start detector looses some of its energy in the entrance foil. Some of its energy is lost also inside the target. Consequently, the velocity measurement does not correspond to its initial velocity for which the conservation laws are applied. In order to obtain the initial velocity a procedure for its reconstruction must be searched for, even considering that the energy lost depends also on the effective atomic number of the ion which is unknown. The iterative method extracts simultaneously the energy lost and the atomic number of the ion, and finally, the primary mass of both fragments.

The velocity $V_{1,2}^0$ (by equation 3.2.1) (first step) and mass (by equations 3.3.1 and 3.3.2) (second step) were extracted by flight path (equation 3.1.1) and TOF (equation 3.1.3) of the reaction fragments.

1. $V_{1,2}^0 = \frac{S_{1,2}}{TOF_{1,2}}$.
2. $M_1^i = \frac{(M_p+M_t)V_2^i sin\theta_2}{V_1^i sin\theta_1 + V_2^i sin\theta_2}$, and
   $M_2^i = M_p + M_t - M_1^i$.

After these two steps a correction for velocity and energy loss in both target and start detectors is applied.

3. At each step i, the correction applies recursively and $V^i_{1,2}$ are obtained by means of the correction:

$$V^{i+1}_{1,2} = V^0_{1,2} + \delta V^i_{1,2} \,. \tag{3.4.1}$$

The quantity $\delta V^i_{1,2}$ is related to the energy loss of the fragment passing through matter, using the Benton-Henke method, implicitly assuming that the trajectory is not modified and approximating the initial energy with the residual one. When a charged particle pass through an absorber, it looses an energy ΔE depending on its mass, charge and initial energy and thickness of the absorber:

$$\Delta E = E_i - E_f = 0.52\, M(V_i^2 - V_f^2)\,, \tag{3.4.2}$$

where $V_i - V_f = \delta V$, energy in *MeV*, mass in *amu*, and velocity are in *cm/ns* units. The solution of δV from equation 3.4.2 becomes:

$$\delta V = \sqrt{V_f^2 - \frac{\Delta E}{0.52M}} - V_f \,.$$

Once the correction $\delta V^i_{1,2}$ is evaluated, the velocity (eq. 3.4.1) is used in the kinematic formulas equations 3.3.1 and 3.3.2 to calculate a new approximation of the masses. This approximation $M^i_{1,2}$ is used as a starting value for the successive step, in which a new correction $\delta V^{i+1}_{1,2}$ is calculated and added always to $\delta V^0_{1,2}$.

4. The value of $\varepsilon = \mid M_1^{i+1} - M_1^i \mid$ is calculated, where M represents the mass calculated in each step.

This procedure is repeated from item (2) until $\varepsilon < 0.01$ that satisfies the required accuracy of determining the fragment mass.

Chapter 4

Experimental Results

In this chapter the main experimental results of the analysis up to the present point are given. Since the experiment was concluded only three months prior the submission of the thesis, the present analysis has to be considered as preliminary. Nevertheless, the present conclusions are quite reliable as far as the ternary direct decay is concerned. Since the most important aim of this thesis is to search for direct true ternary events, this chapter focuses on this specific search.

The reactions in Table 4.1 are those explored in the experiment at JYFL. A set of targets with different backing and thicknesses were used. The measurement runs have also different time duration because of several technical issues that prevented an adequate selection of beam time based on the expected cross sections.

Beam	E_{lab} (MeV)	Targets	Targets Thickness ($\mu g/cm^2$)	CN	Run	Time (hours)
^{37}Cl	195	$^{208}Pb + Al_2O_3$	127.5+40	^{245}Es	1-15	55
		$^{12}C +^{208} Pb +^{12} C$	15+250+5		16-29	
^{40}Ar	230	$^{12}C +^{208} Pb +^{12} C$	15+250+5	^{248}Fm	35-44	14
	193				45-48 58-59	6
^{40}Ar	193	$^{205}Tl +^{12} C$	100+50	^{245}Es	49-57 60	29

Table 4.1: Measurements run during the experiment.

4.1 Binary Fission (Coincidences Arm0 - Arm3): velocity, mass and TKE distributions

Velocities, energies and angles of the primary masses produced in the center-of-mass system of any two reaction products detected in coincidence were computed from the measured time-of-flights and angles by using the momentum and energy conservation laws with the assumption that the mass of the composite system is equal to $M_{target} + M_{projectile}$. Proper energy lost corrections were applied to account for the passage of the ions through the target and in the converter foils of the detectors. The overall mass and energy resolutions were taken as the FWHM, respectively, of the mass and energy spectra built on the elastic channel events. Under these conditions, the mass resolution of the spectrometer is ~4 u and the energy resolution is ~15 MeV. With reference to the used naming conventions, in this section the results of the application of this procedure to the data gathered with Arm0 and Arm3 in coincidence are discussed. These arms corresponds to the ones that are configured so to maximize the detection of the fusion-fission channel. The raw TOF-TOF plots, after time and position calibrations, turn into the typical velocity plots of which the one in Fig. 4.1 is an example. Fig. 4.2 shows instead the Mass-TKE distributions of the primary binary events

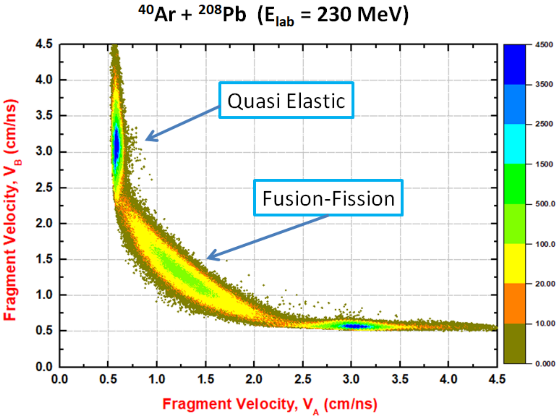

Figure 4.1: An example of a reconstructed 2D velocity plot for coincidences in Arm0 and Arm3.

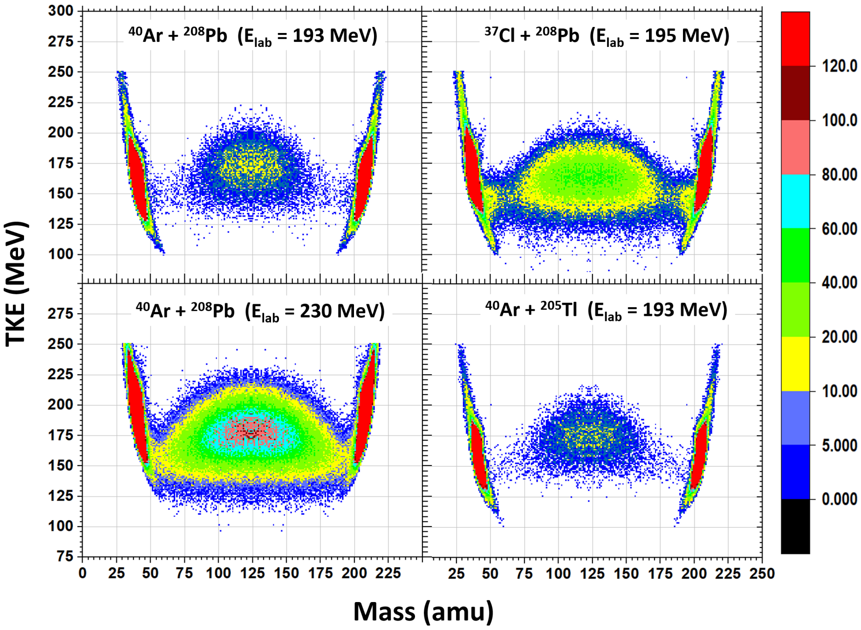

Figure 4.2: Mass-TKE distributions for the binary products measured in full momentum transfer in all reactions under study. Only events within the limits 0.90 < $V_{\parallel}/V_{c.m.}$ *< 1.1 and 0.90 cm/ns <* $V_{\perp}$ *< 1.1 cm/ns are considered. See text for details.*

converted from the plot as in Fig. 4.1 for all reactions. The case of $^{37}Cl\ +\ ^{208}Pb$ at 195 MeV and $^{40}Ar\ +\ ^{205}Tl$ at 193 MeV are supposed to produce the compound nucleus ^{245}Es. The reaction products with masses near to those of the projectile and target give raise to elastic, quasielastic and deep-inelastic events. In between there are the totally relaxed, full momentum transfer events, i.e., as fission (or fission-like) fragments. It is important to remark that sequential fission (the fission of the heavy target-like fragment after the primary two-body interaction) can pollute the true two-body coincidence events and bring to an incorrect reconstruction of the primary mass distribution. These events have been discarded by using a known kinematics method [109] based on the calculation of two velocity vectors from the ones of the detected fragments. The method can be more easily understood by referring to the velocity diagram in Fig. 4.3.

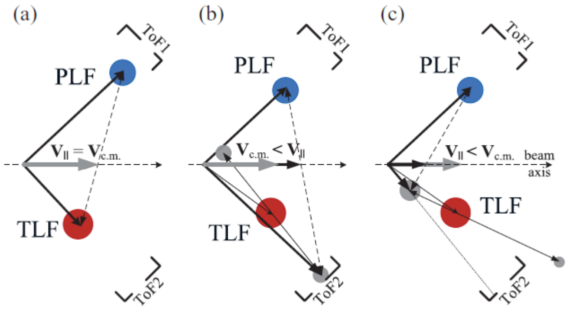

Figure 4.3: Velocity diagrams: (a) for binary events with full momentum transfer; (b) and (c) for the case of sequential fission of TLF (from [109]).

For full momentum transfer events, the velocity $V_{\parallel}$ as in Fig. 4.3 is computed event by event. For a true two-body process $V_{\parallel}$ should be equal to the center-of-mass velocity of the scissioning system $V_{\text{c.m.}}$ (cfr. Fig 4.3(a)). In the case of sequential fission of the TLF (target-

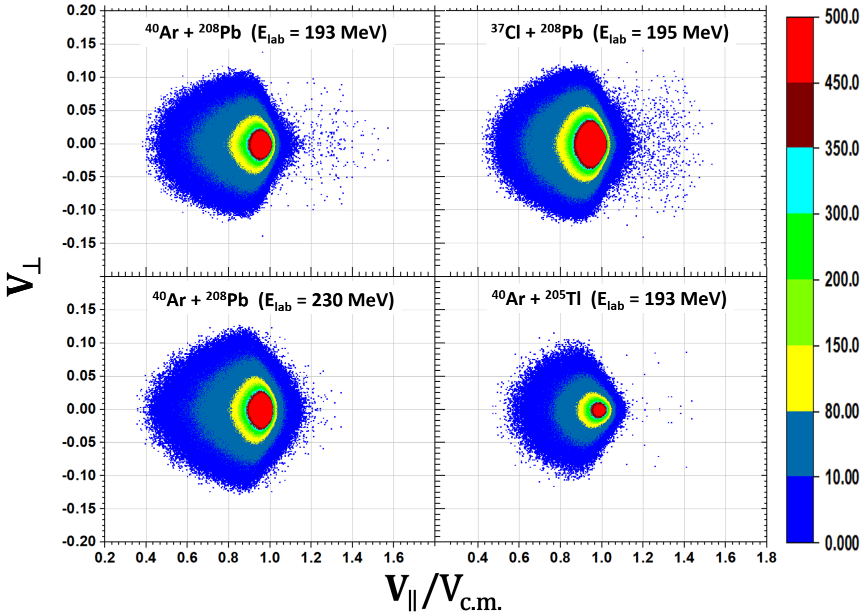

Figure 4.4: $V_{\perp}$ vs. $V_{\parallel}/V_{c.m.}$ distributions for all reactions.

like fragment), $V_{||}$ deviates from $V_{\text{c.m.}}$ and only two cases can occur. If the detected sequential fission fragment is the one that travels forward in the reference frame of the TLF, $V_{||}$ is larger than $V_{\text{c.m.}}$ (cfr. Fig 4.3(b)); if it is the one that travels backward, then $V_{||}$ is lower than $V_{\text{c.m.}}$ (cfr. Fig. 4.3(c)). The distribution of $V_{\perp}$ component of fragment velocity (projection of the fragment velocity vector onto the plane perpendicular to the beam axis) is expected to be symmetric around zero.

Fig. 4.4 illustrates the distribution of $V_{||}$ and $V_{\perp}$ for all the reactions. These plots make clear that with Arm0 in coincidence with Arm3 selects one main group of events, centered around $V_{c.m.}$ with long tail on lower values. As expected, the contribution of sequential fission increases with the bombarding energy confirming that the better conditions to benefit of the survival of the TLF is to be close enough to the Coulomb barrier.

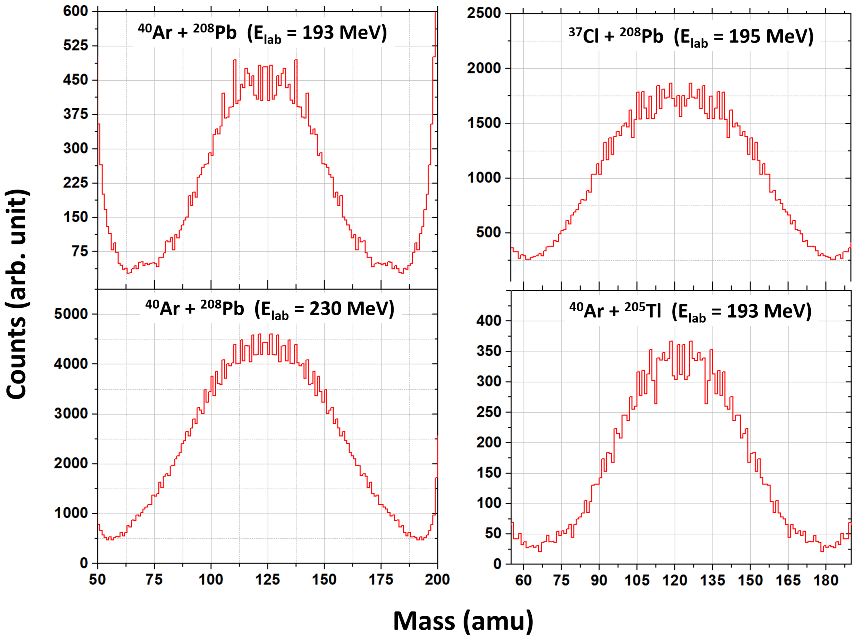

Figure 4.5: Mass distributions for all reactions.

In order to make not-full momentum transfer events negligible, the construction of the M-TKE distributions, for all reactions, was performed only for events within the limits

$0.93 < V_{\|}/V_{c.m.} < 1.1$ and -0.02 cm/ns $< V_{\perp} < 0.02$ cm/ns. In all reactions, the mass distributions are single humped as shown in Fig. 4.5. This indicates that they are mainly driven by a liquid drop potential. However, as shown in the projections on the TKE coordinate (Fig. 4.6), the average TKE distributions deviate from the trend expected from the Viola systematics [110] which represents a fusion-fission of a compound nucleus. The extent of the deviations depends on the entrance channel. Since the reactions in the same column should bring to the same compound nucleus (besides slight differences in excitation energies and angular momentum), from the trend observed it is likely that the abundance of events in the mass asymmetric region is due to the overlap between fusion-fission and quasifission processes, which is typical in the mass and energy regimes under study.

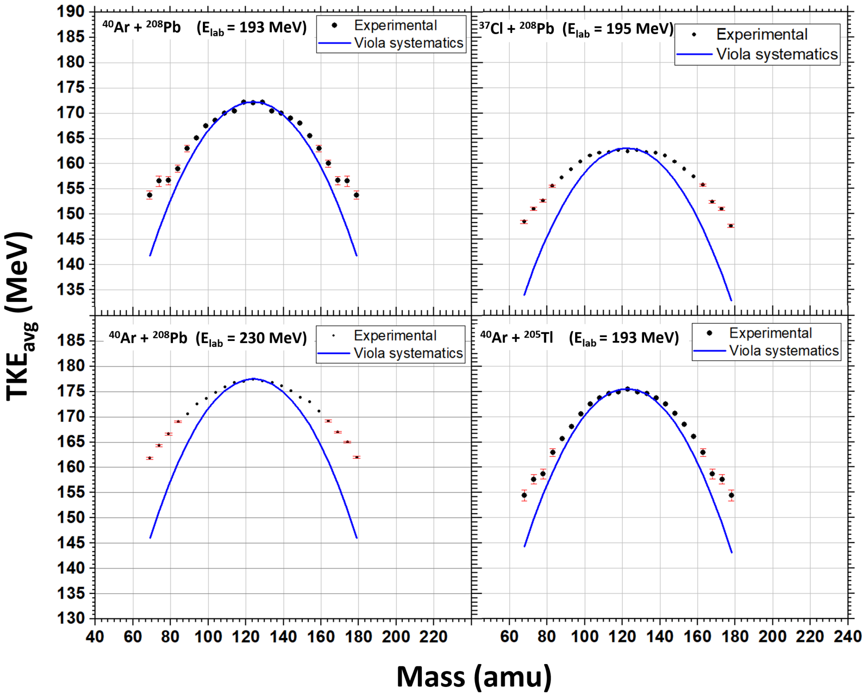

Figure 4.6: TKE distribution for all the reaction studied. The solid lines show the prediction from Viola systematics. The maximum values are normalized to the experimental values which are slightly different because of the energy resolution of the spectrometer.

4.2 Ternary Fission (Coincidences in Arm1 - Arm2): velocity distributions

In this section the coincidence events between Arm1 and Arm2 will be considered in detail as these are the main object of this thesis work.

Fig. 4.7 shows the 2D velocity plots for all reactions obtained after time and position calibrations. These matrices are substantially different than those ones for the case of Arm0-Arm3 coincidences and show some common features, but also some remarkable differences. The common features are the loci corresponding to events with the largest intensities, at low and high velocity, outside the dashed-line boxes. The areas within the boxes, that are of intermediate velocity, show very different patterns and the presence of events localized in clusters. It is important to note that the events in Fig. 4.7 have a strong correlation with the

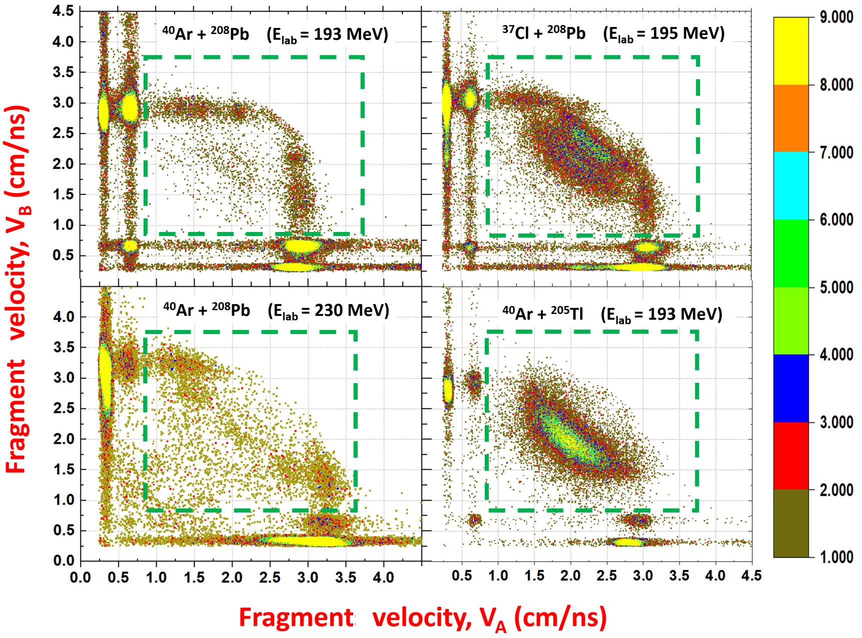

Figure 4.7: 2D velocity plot for coincidences between Arm1 and Arm2. V_A is the velocity in one arm and V_B in the other arm.

events in the $V_\perp$ vs. $V_{||}/V_{c.m.}$ plots which are shown in Fig. 4.8. These show three main $V_{||}$ windows (from this point on we refer to $V_{||}/V_{c.m.}$ as $V_{||}$ only), two of which are below the experimental value of 2.1 cm/ns. The third one is above. Only for the reaction $^{37}Cl + {}^{208}Pb$ there are also two distinct regions above 2.1cm/ns. None of the above regions are around the value $V_{||} \sim V_{cm}$, namely no events from full momentum transfer. Considering the velocity diagram considered earlier (Fig. 4.3), all the events with $V_{||} < 2.1$ are of sequential origin which give rise to a three-body sequential decay. If we remove them in the selection of the events, in the velocity plots in Fig. 4.8 only the events inside the dashed-line box survive. This selection is absolutely critical to investigate the origin of the clustered events that survive the sequential decay.

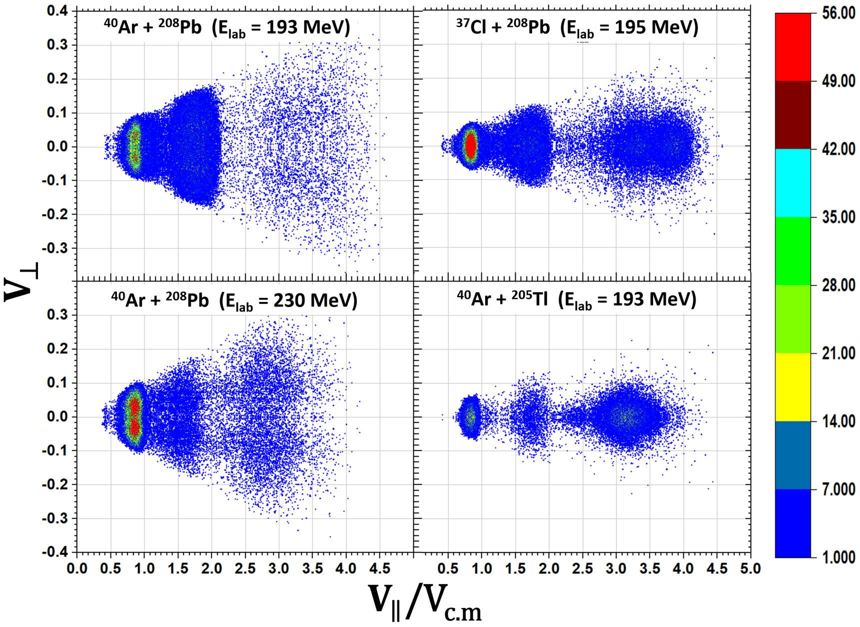

Figure 4.8: $V_\perp$ vs. $V_{||}/V_{c.m.}$ distributions for all reactions for coincidences between Arm1 and Arm2.

4.2.1 Three body channel: velocity plots

It is natural at this point to consider the events that survive such a strong set of conditions as a consequence of a direct ternary decay. The velocity loci occupied by two possible fragments coming from triple decays involving fragments having a magic number of protons, neutrons or both were compute. For these calculations, the main ingredients are the planar three-body kinematics model as developed in Appendix A, the Q values of the final states (cold fragments), and the detector geometry. The overall results are given as curves in Fig. 4.9.

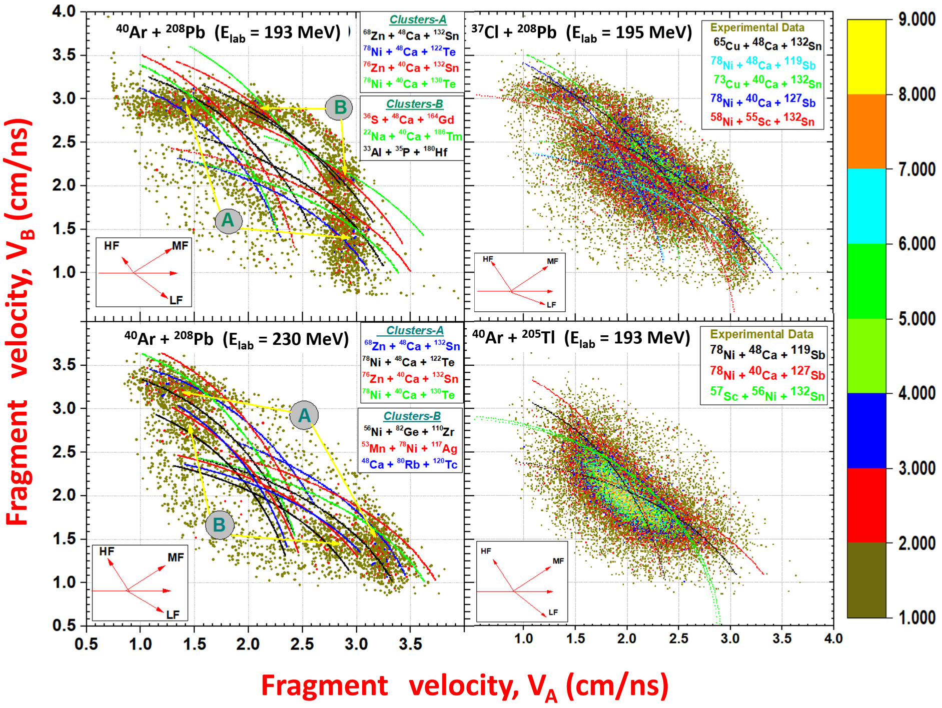

Figure 4.9: Velocity distributions for all reactions for coincidences between Arm1 and Arm2. The lines are the kinematics loci occupied by the selected tripartions in case of a TTF.

The calculated patterns are quite consistent with the positions of the clusters for all the reactions, and show that all the main tripartitions involve ^{132}Sn, ^{78}Ni, ^{48}Ca and ^{40}Ca. In all cases, the kinematics constraints are such that the clusters are consistent with the heaviest fragments emitted backward and the intermediate mass and the lightest emitted in the forward hemisphere. This is shown in the small lower left corner box.

It is important to stress that the computed lines are the results of only energy and momentum conservation laws. The appearance of the TTF in defined loci is the consequence of the cross section of the process. Other combinations not involving magic nuclei do not cross the experimental clusters. A more detailed analysis can be performed case by case.

4.2.2 Three body channel: $^{40}Ar + {}^{208}Pb$ system

In Fig. 4.10, a detailed highlight of the experimental two velocity maps and the overlap with the computed curves is shown. First of all, the experimental two-velocity (2V) patterns change drastically with a slight change of beam energy. If three bodies are indeed produced simultaneously, the different patterns are the consequence of accessing a different entrance point in the potential energy surface because of the higher interaction energy. As a consequence, different valleys in the potential can be accessed (this is true also for the binary case) and different combinations of fragments can be produced.

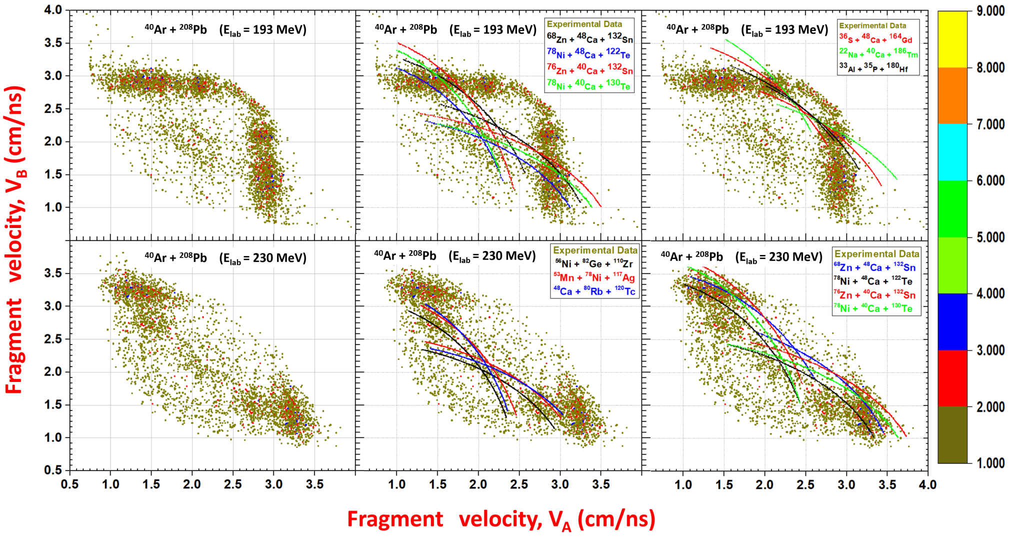

Figure 4.10: Velocity distributions for the reactions $^{40}Ar + {}^{208}Pb$ along with kinematics calculations for selected tripartitions.

Second, moving from lower to higher velocities in the two-velocity maps the combination of masses is such that fragment emitted at backward angles is the heaviest and the other two are lighter. This trend is verified for all the reactions and supports the overall interpretation. Finally, in all the three-body combinations selected there is at least a double magic nucleus, but the majority of the combinations have at least two magic nuclei. Furthermore, at higher excitation energy, the possible combinations with two lighter nuclei disappears. This can be interpreted as the consequence of the fact that the accessed valleys have higher barriers and is confirmed by the fact that there are some combinations that are accessed in both reactions while others are not.

In Table 4.2 we show which tripartition is accessed by both reactions and which are not. Furthermore, we also provide the expected laboratory energy of the third fragment to be detected in the most backward telescope. It is quite striking that, regardless of the entrance channel energy and of the different location of the clusters in the two-velocity maps, for the two reactions all the common tripartitions are composed by at least by two magic nuclei.

4.2.3 Three body channel: $^{37}Cl + {}^{208}Pb$ and $^{40}Ar + {}^{205}Tl$ systems

The case of these two reactions is particularly interesting because the same amount of protons and neutrons is colliding, but starting from a different asymmetry in the entrance channel. This means that the potential energy surface is the same but the access point in the potential surface is necessarily different. In Fig. 4.11 the progression of the patterns in the two reactions for different windows of the observable $V_{||}$ which have been chosen by looking at the pattern in Fig. 4.8 is shown. There are two well defined areas for $V_{||} > 3.0$ in the case of $^{37}Cl + {}^{208}Pb$ system, whereas for the case of $^{40}Ar + {}^{205}Tl$ the second area above 3.5 cm/ns is nearly borne. In particular, the locus for lower values of $V_{||}$ is slightly dislocated for the two reactions as a consequence of the slightly different center of mass velocity and Q value. Even though for the system $^{40}Ar + {}^{205}Tl$ the separation is not that clear, a two-velocity map for both reactions for events within the same $V_{||}$ window were built. The fact that similar

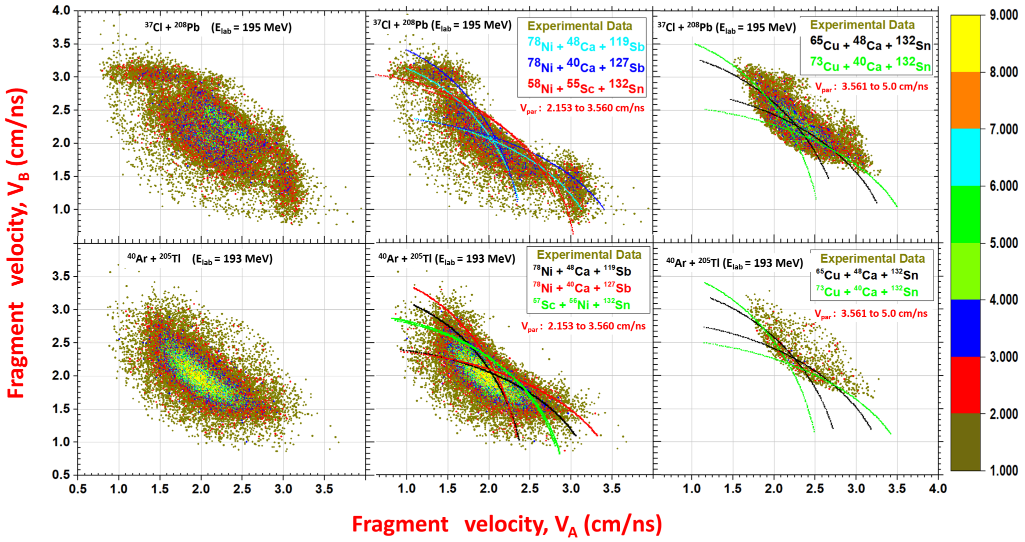

Figure 4.11: Velocity distributions for the reactions ^{37}Cl + ^{208}Pb (top row) and ^{40}Ar + ^{205}Tl at 195 MeV along with kinematics calculations for selected tripartitions.

loci are populated, but with different intensity, clearly means that the same potential is acting (it is not an artifact of each reaction) and that there might be identical tripartitions that can be accessed in both reactions, independently on the position of the access point in the potential surface. The confirmation of this interpretation comes from the fact that there are common tripartitions that can be populated in each reaction even though they occupy different loci in the two-velocity maps for the same window of $V_{||}$. In Table 4.3 it is shown which tripartition is accessed by both reactions and which is not. Furthermore, we also provide the expected laboratory energy of the third fragment to be detected by the most backward telescope. Also for these two reactions, regardless of the different entrance channel, all the common tripartitions are composed at least by two magic nuclei.

4.3 Data from ΔE-E telescopes

The bulk of the patterns discussed above constitutes by itself a first strong evidence of the occurred direct true ternary decay. However, the smoking gun of this interpretation would be the detection in coincidence of the third fragment via the ΔE-E telescopes. Six ΔE-E telescopes were indeed mounted in the backward hemisphere for this purpose. As discussed in the introduction, it is possible to identify the masses (necessarily with some experimental resolution) of the three fragments by detecting the position and TOF of two of them and the energy of the third one in a detector at a fixed backward angle. This method would eliminate the uncertainty of choosing *a priori* the tripartition as done in the previous sections. Unfortunately, at one point, the preamplifiers chosen did not work properly anymore as unexpectedly the output signal turned out to be quickly saturated by the energies released by the detected fragments. Consequently the fast amplifiers were not properly armed. Unfortunately there was no replacement available for the preamplifiers and the problem could not be fixed during the experimental run. Therefore, the whole coincidence scheme could not be effective. Nevertheless, few important observations on the detected single events can still be drawn to support the whole interpretation given above.

Cluster Tri-partition	^{40}Ar + ^{208}Pb (at 193 MeV)	^{40}Ar + ^{208}Pb (at 230 MeV)	E_3 (MeV) (at 193 MeV)	E_3 (MeV) (at 230 MeV)
^{68}Zn + ^{48}Ca + ^{132}Sn	Yes	Yes	21	22
^{78}Ni + ^{48}Ca + ^{122}Te	Yes	Yes	20	21
^{76}Zn + ^{40}Ca + ^{132}Sn	Yes	Yes	13	14
^{78}Ni + ^{40}Ca + ^{130}Te	Yes	Yes	12	13
^{56}Ni + ^{82}Ge + ^{110}Zr	-	Yes	-	28
^{48}Ca + ^{80}Rb + ^{120}Tc	-	Yes	-	19
^{53}Mn + ^{78}Ni + ^{117}Ag	-	Yes	-	26
^{36}S + ^{48}Ca + ^{164}Gd	Yes	-	15	-
^{22}Na + ^{40}Ca + ^{186}Tm	Yes	-	5	-
^{33}Al + ^{35}P + ^{180}Hf	Yes	-	1	-

Table 4.2: Table of the tripartitions accessed by the system ^{40}Ar + ^{208}Pb *at 193 and 230 MeV. The expected energy of the third (heaviest) fragment is also given for the lab angle* $\theta_{lab} = 154.5°$.

Cluster Tri-partition	$^{37}Cl + {}^{208}Pb$ (at 195 MeV)	$^{40}Ar + {}^{205}Tl$ (at 193 MeV)	E_3 (MeV) ($^{37}Cl + {}^{208}Pb$)	E_3 (MeV) ($^{40}Ar + {}^{205}Tl$)
$^{78}Ni + {}^{48}Ca + {}^{119}Sb$	Yes	Yes	23	29
$^{78}Ni + {}^{40}Ca + {}^{127}Sb$	Yes	Yes	25	22
$^{65}Cu + {}^{48}Ca + {}^{132}Sn$	Yes	Yes	23	25
$^{73}Cu + {}^{40}Ca + {}^{132}Sn$	Yes	Yes	29	25
$^{58}Ni + {}^{55}Sc + {}^{132}Sn$	Yes	-	23	-
$^{57}Sc + {}^{56}Ni + {}^{132}Sn$	-	Yes	-	18

Table 4.3: Table of the tripartitions accessed by the systems $^{37}Cl + {}^{208}Pb$ and $^{40}Ar + {}^{205}Tl$. The expected energy of the third (heaviest) fragment is also given for the angle $\theta_{lab} = 154.5°$.

Besides the expected trend for the energy of the ejectiles with increasing laboratory angle, namely, the appearance of the more dissipative component for laboratory angles larger than the grazing angle, there appears a large amount of events with energies above 20 MeV up to 60 MeV in the most backward telescope ($\theta_{lab} = 154.5°$) that cannot be originated by fission

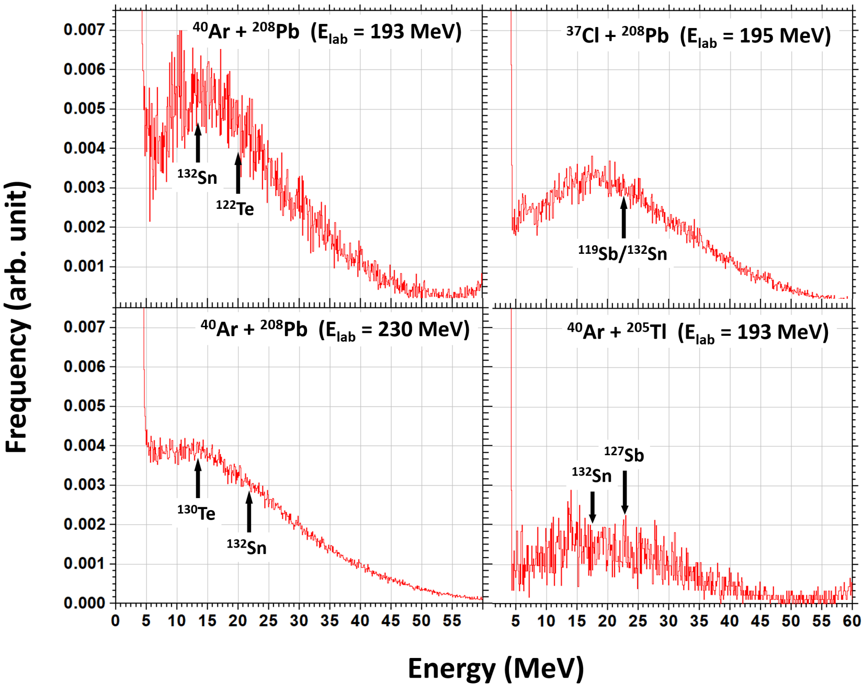

Figure 4.12: Energy spectra of the fragments stopping in the ΔE telescope at $\theta_{lab} = 154.5°$.

or quasifission two-body events because the center of mass motion would push all of them in the forward hemisphere. In particular, Fig. 4.12 shows the energy spectra of the ions stopping in the ΔE stage for the most backward telescope at θ_{lab} = 154.5°. We have indicated with an arrow the energy expected by the third fragment if our reconstruction of the possible mass tripartitions would hold. These spectra do not include protons or alpha particles since they are discarded via the gates on ΔE-E map. In each reaction the observed broad peak covers well the energy range of the third fragment as companion of the two fragments detected with Arm1 and Arm2 in the forward direction. This is particularly surprising for the case of the reaction ^{40}Ar + ^{208}Pb at 230 MeV because we would not expect such a large number of events by any known isotropic process for this reaction. We cannot of course compare directly the rate in the telescopes with the one assigned to ternary events detected by coincidence in Arm1/Arm2 because the energy spectra were detected in singles, but the energy range coverage could indicate that channels with large positive Q values give rise to such energetic events. This feature of the energy spectra, common to all reactions studied, gives confidence in the reconstruction of ternary events and motivations to run the same experiment again with more statistics and by replacing this malfunctioning part of the setup that is, at this point, crucial to provide the definitive proof of the occurrence of TTF.

4.4 Closing remarks

The main experimental evidence of this work is the presence of specific loci in the two-velocity maps for all the reactions investigated. The geometry of the setup was chosen so to constraint the detection of direct three-body decays. From a simple planar three-body kinematics it was possible to compute the angular correlations of the velocity vectors of the three fragments of chosen mass. With the hypothesis that three-body decay would have been favored by the shell closures, the prediction were focused on such specific tripartitions. It was not expected that the two-velocity maps would show specific cluster patterns. Indeed, such patterns have helped in searching for possible tripatitions. The support to the occurrence of the direct three-body decay lies on two main points: 1) the cluster patterns are reproduced for all the four reaction studied; 2) there is a consistent overlap between the tripartitions that reproduce the data in the companion reactions $^{37}Cl\ +\ ^{208}Pb$ and $^{40}Ar\ +\ ^{205}Tl$, and in the reactions $^{40}Ar\ +\ ^{208}Pb$ at 193 and 230 MeV.

Reactions	E_{lab} (MeV)	Ternary/Binary
$^{37}Cl + ^{208}Pb$	195	4.6±0.2
$^{40}Ar + ^{205}Tl$	193	2.1±0.1
$^{40}Ar + ^{208}Pb$	193	0.23±0.01
$^{40}Ar + ^{208}Pb$	230	0.033±0.003

Table 4.4: Ratio between Ternary and Binary events for each reaction.

Last but not least, we can compare the rate for binary and ternary decays, by simply calculating the ratio of the events corrected for the efficiency. Table 4.4 shows the computed ratio by taking all the events in the M-TKE map in between the quasielastic peaks, and all the event in the two-velocity maps assigned to ternary decays. These ratios are quite striking because in spontaneous fission the simultaneous ternary decay is several order of magnitude less abundant. In the case of $^{37}Cl\ +\ ^{208}Pb$ and $^{40}Ar\ +\ ^{205}Tl$, TTF is even from 2 to 4 times more abundant than binary fission. A larger cross section for TTF was indeed one of the expectation of the original proposal of this experiment. Clearly, further checks will be needed before considering these numbers as definitive. Nevertheless, the consistency of the reproduction of the cluster patterns in the two-velocity map gives confidence to the proposed interpretation.

Conclusions and Perspectives

In this work, four reactions were studied with the aim to populate channels of true ternary fission. The main idea is that if TTF is (expected to be) a very rare process in spontaneous fission, it could be much more probable in induced reactions if shell effects could be taken in considerations. To favor the occurrence of shell effects we have chosen entrance channels that would amplify shell effects, as the typical conditions that favor quasifission: reactions at Coulomb barrier energies and choice of magic or double magic partner nuclei.

The experimental setup was constrained on the possible tripartitions in magic and doubly magic nuclei by using a simple planar 3-body kinematics and Q values. It was unexpected that the velocity plots of two out of three fragments would show cluster patterns. It is even more surprising that a quite large set of tripartition is able to reproduce, consistently, all the velocity patterns for the four reactions, by even using the same tripartitions. This work constitutes the first evidence of the possibility of TTF in induced reactions.

Clearly, there are many steps forward that are at this point necessary to confirm the main results of this work. ΔE-E telescopes are needed to be replaced and it might be tried to cover a larger solid angle, even by covering out of plane angles to fully explore the three body decay over 4π. This can in principle be accomplished by running similar experiments with 4π detectors, one of which is the array 8πLP [111] at Laboratori Nazionali di Legnaro. Another step is to identify other nuclei for which tripartition composed of magic nuclei are allowed from the conservation of the number of protons and neutrons. Several of these cases were already identified and can be accessed with the available beams. These aspects will be investigated in future experiments.

Appendix A

Direct Ternary Fission

The kinematics of nuclear reactions having more than two particles in the final state has been shown by P.A. Assimakopoulos [112] in 1975. It is mentioned that for the complete specification of the final state, a large set of kinematics variables are needed which are the main difficulties in experimental studies of such reactions. From the knowledge of initial state and by applying energy and momentum conservation, it is possible to reduce the number of independent variables. Therefore for three known masses and measured first fragment energy (E_1), it possible to calculate the energies of other two fragments by using energy and momentum conservation laws.

Let us assume a nuclear reaction having projectile mass M_p, target mass M_t, three fragments having masses M_1, M_2, and M_3. These three fragments have energies E_1, E_2, and E_3. These three fragments are detected at angles θ_1, θ_2, and θ_3 with respect to beam direction. If we measure first fragment energy (E_1) and angles of two heavy fragments (θ_1, and θ_2), then we can calculate angle of third fragment (θ_3) and energies of second and third fragments (E_2, and E_3). For known energy of the first fragment, the velocity is:

$$V_1 = \sqrt{\frac{2E_1}{M_1}}. \tag{A.0.1}$$

Energy conservation for three body spontaneous decay allows to have velocity of the third fragment by the following way:

$$
\begin{aligned}
E_p &= E_1 + E_2 + E_3 - Q\,, \\
or,\ E_p &= \frac{1}{2}M_1 V_1^2 + \frac{1}{2}M_2 V_2^2 + \frac{1}{2}M_3 V_3^2 - Q\,, \\
or,\ V_3 &= \left[\frac{2(E_p + Q) - M_1 V_1^2 - M_2 V_2^2}{M_3}\right]^{1/2}. \qquad \text{(A.0.2)}
\end{aligned}
$$

Momentum conservation in beam direction becomes:

$$
\begin{aligned}
M_p V_p &= M_1 V_1\, Cos\theta_1 + M_2 V_2\, Cos\theta_2 + M_3 V_3\, Cos\theta_3\,, \\
or,\ Cos\theta_3 &= \frac{M_p V_p - M_1 V_1\, Cos\theta_1 - M_2 V_2\, Cos\theta_2}{M_3 V_3} \\
or,\ \theta_3 &= Cos^{-1}\left[\frac{M_p V_p - M_1 V_1\, Cos\theta_1 - M_2 V_2\, Cos\theta_2}{\sqrt{M_3\{2(E_p + Q) - M_1 V_1^2 - M_2 V_2^2\}}}\right].(by\, using\, equ.A.0.2) \qquad \text{(A.0.3)}
\end{aligned}
$$

Momentum conservation in perpendicular to the beam direction becomes:

$$
\begin{aligned}
0 &= M_1 V_1\, Sin\theta_1 + M_2 V_2\, Sin\theta_2 + M_3 V_3\, Sin\theta_3\,, \\
or,\ V_2 &= -\frac{M_1 V_1\, Sin\theta_1 + M_3 V_3\, Sin\theta_3}{M_2\, Sin\theta_2} \qquad \text{(A.0.4)}
\end{aligned}
$$

Applying equations A.0.2 and A.0.3 in equation A.0.4, we get the following solution for V_2

$$
V_2 = \frac{-B \pm \sqrt{B^2 - 4AC}}{2A}, \qquad \text{(A.0.5)}
$$

where,

$$
\begin{aligned}
A &= M_2(M_2 + M_3), \\
B &= 2\,\{M_1 M_2 V_1\, Cos(\theta_1 - \theta_2) - M_p M_2 V_p\, Cos\theta_1\}, \\
C &= M_p^2 V_p^2 + M_1^2 V_1^2 + M_1 M_3 V_1^2 - 2M_3 E_p - 2M_p V_p M_1 V_1\, Cos\theta_1 - 2M_3 Q.
\end{aligned}
$$

- The energy of third ($E_3 = M_3 V_3^2\,/\,2$) fragment can be calculated by using equations A.0.5 and A.0.1 in equation A.0.2.
- The energy of second ($E_2 = M_2 V_2^2\,/\,2$) fragment can be calculated by using equation A.0.5.
- The angle of third (θ_3) fragment can be calculated by using equations A.0.5 and A.0.1 in equation A.0.3.

Appendix B

Features of the Setup

Fragments produced by binary decays were detected by two CORSET arms placed at 65^0 of each side of beam direction. Fragments produced by ternary decays were detected by two CORSET arms placed at 40^0 at each side of beam direction and ΔE-E telescopes placed at the backward hemisphere, three on each side of the beam, to cover the angular range between 107^0 and 156.5^0 (Fig. 2.1 and 2.2)

B.1 CORSET arms

All major features of four CORSET arms are given in table B.1 (all parameters are also mentioned in Fig. 2.2).

The angular coverage by MCP of the stop detector are shown in Fig. B.1, where X denotes the horizontal and Y denotes the vertical position of the MCP. It is possible to say that MCP covers from 30^0 to 50^0 when centre are placed at 40^0 with beam direction.

The flight path covered by MCP of the stop detector are shown in Fig. B.2, where X denotes the horizontal and Y denotes the vertical position of the MCP. It is possible to say that MCP covers from 220 *mm* to 223.5 *mm* when centre to center are placed at 220 *mm*.

Parameters	arm-0	arm-1	arm-2	arm-3
Target-Start Detector (L_{st})	8 cm	8.5 cm	8.5 cm	8 cm
Target-Stop Detector (L_{sp})	26 cm	30.5 cm	30.5 cm	26 cm
Angular Positions (θ)	65^0	40^0	40^0	65^0
Flight Path (S)	18 cm	22 cm	22 cm	18 cm
Dimension of Start Detector	3×2.2 cm^2	2.2×2.2 cm^2	2.2×2.2 cm^2	3×2.2 cm^2
Dimension of Stop Detector	8.6×6.9 cm^2	8.6×6.9 cm^2	8.6×6.9 cm^2	8.6×6.9 cm^2
Current to Start Detector (μA)	147	160	150	150
Current to Stop Detector (μA)	227	155	180	160
Voltage to Start Detector (V)	2556	2338	2580	2420
Voltage to Stop Detector (V)	3022	2505	2640	2570

Table B.1: Main parameters of four CORSET arms.

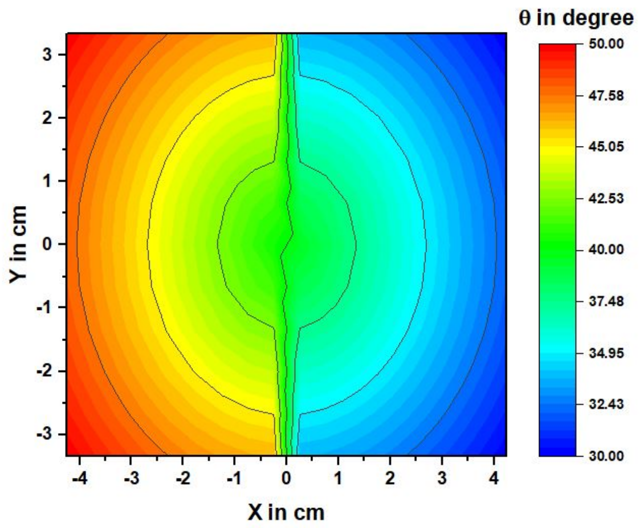

Figure B.1: Angle coverage in terms of beam direction on the stop detector from the target.

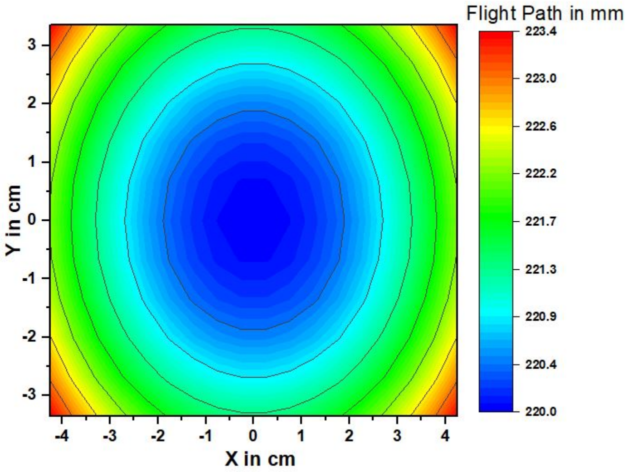

Figure B.2: Flight path of the fragments on the stop detector.

B.2 Telescopes

Six ΔE - E Telescopes (Fig. 2.6) were used in the backward hemisphere, in plane with the arms of the TOF spectrometer.

Three ΔE - E Telescopes were placed on each side of the beam. In one side (same side of CORSET arm-0 and arm-1), three telescopes cover the angular range between 107^0 and 147.7^0 and on the other side three telescopes cover the angular range between 116^0 and 156.5^0. Details on the parameters are shown in Fig. 2.2. The thicknesses with model number of the ΔE - E detectors used in the experiment, applied current and voltages to all detectors are shown in table B.2.

B.3 Monitors

Three detectors were placed at forward angles to monitor the quality of the beam. Three silicon detectors were used in the positions shown in Fig. 2.7. The centre of monitors detector plate are placed 64.5 cm away from the target and 8.64^0 (*MD0*), 8.64^0 (*MD1*), and 8.73^0 (*MD2*) are angles of three detectors in terms of beam line.

Telescopes	Detectors	Serial No.	Thickness (μm)	Current (μA)	Bias Voltage (V)
0	ΔE	26-421G	21.2	0.67	25.3
	E	1568-20	292	0.85	40
1	ΔE	26-416B	22	0.65	28
	E	1779-6	292	0.05	16
2	ΔE	26-421D	24.2	0.66	27
	E	1779-12	278	0.05	15
3	ΔE	26-256H	18.7	0.92	28.1
	E	1779-9	286	0.07	12
4	ΔE	22-067F	22.9	1.09	30.2
	E	1799-13	301	0.03	20
5	ΔE	22-700C	23.4	0.62	26.1
	E	1794-14	305	0.01	18

Table B.2: Major features of the E - ΔE Telescopes.

Monitors Detectors	Serial No.	Thickness (μm)	Current (μA)	Bias Voltage (V)
0	29-362G	47.8	0.15	33
1	29-417A	46.9	0.29	26.5
2	29-362H	47.6	0.16	24.1

Table B.3: Major features of the Monitor Detectors.

Aluminium foil having thickness of 20 microns were used as absorber in front of all monitor detectors. As all monitors are very close to beam line, elastically scattered particles get very high energy (close to beam energy) in such position and monitor detectors can not stop such particles. So, it was necessary to insert some absorber in front of the detectors.

Appendix C

Calibration Parameter

C.1 Position Calibration:

The correlation of different channel numbers corresponding to the known points mentioned in Fig. 3.1 are given in tables C.1, C.2 , and C.3 for three different reactions.

The calibration parameters (slopes and intercepts) are calculated by linear regression method for the values of the tables C.1, C.2, and C.3 and these are presented in table C.4. The expressions for calibrated positions are written in the following way:

$$\mathrm{X_{mcp}} = \mathrm{Slope\,(mm/ch)} \times \mathrm{Channel_X} + \mathrm{Intercept\,(mm)} \text{ and}$$
$$\mathrm{Y_{mcp}} = \mathrm{Slope\,(mm/ch)} \times \mathrm{Channel_Y} + \mathrm{Intercept\,(mm)}\,.$$

C.2 Time-of-Flight Calibration:

The calibration parameters (slops and intercepts) of CORSET arms are calculated for three different reactions by the process mentioned in section 3.1.2 of chapter 3. These parameters of four CORSET arms for three different reactions are presented in table C.5.

X_0		**Y_0**		**X_1**		**Y_1**	
Channel	mm	Channel	mm	Channel	mm	Channel	mm
854	-18	833	-19	822	-19	791	-19
854	-18	833	-19	822	-19	791	-19
1106	18	1033	19	1072	19	994	19
1106	18	1033	19	1072	19	994	19
1280	43	1118	34.5	1228	43	709	-34.5

X_2		**Y_2**		**X_3**		**Y_3**	
Channel	mm	Channel	mm	Channel	mm	Channel	mm
744	-19	917	-19.5	1024	-19	702	-19
744	-19	917	-19.5	1022	-19	702	-19
1010	19	1133	19.5	1287	19	928	19
1010	19	1133	19.5	1287	19	926	19
583	-43	837	-34.5	860	-43	1015	34.5

Table C.1: Position Calibration points of CORSET arms for Cl+Pb *reaction.*

X_0		**Y_0**		**X_1**		**Y_1**	
Channel	mm	Channel	mm	Channel	mm	Channel	mm
865	-18	833	-19	827	-19	788	-19
864	-18	833	-19	827	-19	788	-19
1110	18	1036	19	1071	19	992	19
1110	18	1036	19	1072	19	992	19
1281	43	1121	34.5	677	-43	705	-34.5

X_2		**Y_2**		**X_3**		**Y_3**	
Channel	mm	Channel	mm	Channel	mm	Channel	mm
746	-19	918	-19.5	1015	-19	706	-19
746	-19	918	-19.5	1015	-19	706	-19
1010	19	1133	19.5	1275	19	929	19
1010	19	1134	19.5	1277	19	929	19
585	-43	837	-34.5	850	-43	1020	34.5

Table C.2: Position Calibration points of CORSET arms for Ar+Tl *reaction.*

$\mathbf{X_0}$		$\mathbf{Y_0}$		$\mathbf{X_1}$		$\mathbf{Y_1}$	
Channel	mm	Channel	mm	Channel	mm	Channel	mm
865	-18	829	-19	819	-19	789	-19
865	-18	830	-19	819	-19	788	-19
1112	18	1035	19	1066	19	996	19
1112	18	1034	19	1066	19	994	19
1282	43	1122	34.5	660	-43	706	-34.5

$\mathbf{X_2}$		$\mathbf{Y_2}$		$\mathbf{X_3}$		$\mathbf{Y_3}$	
Channel	mm	Channel	mm	Channel	mm	Channel	mm
746	-19	915	-19.5	1019	-19	704	-19
746	-19	914	-19.5	1019	-19	704	-19
1011	19	1132	19.5	1280	19	927	19
1012	19	1132	19.5	1281	19	931	19
582	-43	836	-34.5	855	-43	1019	34.5

Table C.3: Position Calibration points of CORSET arms for Ar+Pb *reaction.*

	Cl+Pb		**Ar+Tl**		**Ar+Pb**	
	Slope (mm/ch)	*Intercept (mm)*	*Slope (mm/ch)*	*Intercept (mm)*	*Slope (mm/ch)*	*Intercept (mm)*
$\mathbf{X_0}$	0.1541	-152.3	0.1544	-152.3	0.1554	-153.7
$\mathbf{Y_0}$	0.1884	-175.1	0.1875	-174.18	0.1875	-175.2
$\mathbf{X_1}$	0.1474	-139.5	0.1474	-140.4	0.1514	-143.1
$\mathbf{Y_1}$	0.1793	-159.3	0.1780	-158.0	0.1793	-159.5
$\mathbf{X_2}$	0.1376	-120.5	0.1359	-119.0	0.1514	-143.1
$\mathbf{Y_2}$	0.1670	-170.5	0.1680	-171.4	0.1793	-159.5
$\mathbf{X_3}$	0.1397	-161.5	0.1400	-160.8	0.1408	-161.9
$\mathbf{Y_3}$	0.1655	-134.7	0.1669	-136.9	0.1669	-136.8

Table C.4: Position calibration parameters of four CORSET arms.

Reactions	Run	Parameter	TOF_0	TOF_1	TOF_2	TOF_3
Cl+Pb	1-13	Slope (ns/ch	-0.02638	-0.02623	-0.02372	-0.02516
		Intercept (ns)	109.7612	113.60483	102.60649	93.30345
	14-29	Slope (ns/ch	-0.026378	-0.02623	-0.02372	-0.02516
		Intercept (ns)	109.9220	113.83565	102.10555	96.9911
Ar+Tl	49-57	Slope (ns/ch	-0.02638	-0.02624	-0.02372	-0.02516
	60	Intercept (ns)	110.1241	113.7841	102.38638	94.73774
Ar+Pb	35-44	Slope (ns/ch	-0.026387	-0.02623	- 0.02372	-0.02516
		Intercept (ns)	109.9801	113.52465	102.37694	94.32345
	45-48	Slope (ns/ch	-0.02638	-0.02623	-0.02372	-0.02516
	58-59	Intercept (ns)	109.9801	113.66386	102.68107	94.32345

Table C.5: TOF calibration parameters of CORSET arms for three reactions.

Channel (arb. unit)	E (MeV)
143	1.129
173	2.374
194	3.135
255	5.397

Table C.6: Calibration points for E detector.

Channel (arb. unit)	ΔE (MeV)
191	2.253
181	2.815
175	3.076
164	3.621

Table C.7: Calibration points for ΔE detector.

C.3 Energy Calibration:

The energies at detectors with associated channel numbers are given in table C.6 and table C.7. The calibration parameters (slopes and intercept) are calculated by using linear regression method for the values of the table C.6 and C.7. The parameters are presented in table C.8 for two detectors of telescope 3.

	Slope (MeV/Ch)	Intercept (MeV)
E	0.03795286	-4.2630992
ΔE	0.05033237	-6.0016908

Table C.8: Calibration parameters for E and ΔE detectors.

Appendix D

Potential Energy Calculation: Three Cluster Model

Ternary fragmentation potential between the three (spherical) fragments in collinear and triangular (equatorial) geometry can be calculated by three cluster model (TCM) [54–61]. According to TCM, ternary fragmentation potential is the sum of the total Coulomb potential, the total nuclear potential, and the sum of the mass excesses of the ternary fragments. So, It can be written as:

$$V_{tot} = \sum_{i=1}^{3} \sum_{j>i}^{3} \left(m_x^i + V_{ij} \right), \tag{D.0.1}$$

where m_x^i are the mass excesses of the three fragments in energy units, taken from [113]. V_{ij} is the sum of coulomb and nuclear potential:

$$V_{ij} = V_{Cij} + V_{Pij}, \tag{D.0.2}$$

where V_{Cij} is the coulomb interaction potential and V_{Pij} is the proximity potential. The Coulomb interaction between the nuclei is defined as

$$V_{Cij} = Z_i Z_j e^2 / R_{ij}, \tag{D.0.3}$$

where R_x is the radius of the fragment. It is defined by,

$$R_x = 1.28\, A_x^{1/3} - 0.76 + 0.8\, A_x^{-1/3},$$

where x is taking the values of 1, 2, and 3 corresponding to fragments A_1, A_2, and A_3. R_{ij} is the distance between the centers of the interacting fragments, $R_{ij} = R_i + R_j$ is the center to center distance of nuclei A_i and A_j.

The proximity potential V_{Pij} is defined as

$$V_{Pij} = 4\pi\bar{R}\gamma b\phi(\xi). \tag{D.0.4}$$

The universal function $\phi(\xi)$ depends only on the distance between two nuclei and is independent of the atomic numbers of the two nuclei. It is given by

$$\phi(\xi) = -\frac{1}{2}(\xi - 2.54)^2 - 0.0852(\xi - 2.54)^3 \ when \ \xi < 1.2511$$

$$\phi(\xi) = -3.437\, exp(-\xi/0.75) \ when \ \xi \geq 1.2511$$

.

Here, $\xi = S_{ij}/b$. S_{ij} is the surface separation of nuclei A_i amd A_j and defined as:

$$S_{ij} = R_{ij} - R_i - R_j$$

. The function $\phi(\xi)$ is defined for three different values of S by the following way:

- For the overlap region between the nuclei, S is negative,
- For the separated configuration between the nuclei, S is positive, and
- For touching configuration between the nuclei, S is zero.

and b is the diffusivity parameter of the nuclear surface given by b = 0.99 fm. The specific nuclear surface tension γ is given by

$$\gamma = 0.9517\left[1 - 1.7826\left(\frac{N-Z}{A}\right)^2\right] MeV fm^{-2}. \tag{D.0.5}$$

The mean curvature radius, $\bar{R}$ has the form

$$\bar{R} = \frac{R_i R_j}{R_i + R_j}. \tag{D.0.6}$$

Nucleus	A_1	A_2	A_3	Q (MeV)	V_{total} (MeV)	
					Collinear	Equatorial
^{245}Es	^{132}Sn	^{65}Cu	^{48}Ca	254.4001	93.56	82.24
	^{119}Sb	^{78}Ni	^{48}Ca	234.197	108.2	98.27
	^{132}Sn	^{73}Cu	^{40}Ca	236.7457	110.3	102.37
	^{127}Sb	^{78}Ni	^{40}Ca	222.0439	121.57	114.19
	^{151}Eu	^{78}Ni	^{16}O	179.887	118.45	89.77
	^{181}Lu	^{48}Ca	^{16}O	160.1272	98.42	69.39
	^{132}Sn	^{56}Ni	^{57}Sc	217.5258	136.43	127.32
^{248}Fm	^{132}Sn	^{68}Zn	^{48}Ca	262.6742	97.71	86.97
	^{122}Te	^{78}Ni	^{48}Ca	240.5679	111.42	102.26
	^{132}Sn	^{76}Zn	^{40}Ca	245.592	114.13	106.74
	^{130}Te	^{78}Ni	^{40}Ca	228.2281	125.01	118.46
	^{154}Gd	^{78}Ni	^{16}O	184.4711	122.59	94.26
	^{184}Hf	^{48}Ca	^{16}O	162.362	104.22	75.49
	^{132}Sn	^{56}Ni	^{60}Ti	224.6775	141.71	134.43

Table D.1: Ternary fragmentation potential between the three fragments decaying in collinear and triangular (equatorial) configuration for ^{245}Es and ^{248}Fm nuclei.

Proximity potential was calculated by applying equations D.0.6, D.0.5, and the value of function $\phi(\xi)$ in equation D.0.4. Finally, by getting mass excess from [113] and using equations D.0.4 and D.0.3 in equation D.0.1, the ternary fragmentation potential between the three decaying fragments is calculated. Ternary fragmentation potential between the most provable ternary fragments decaying in collinear and triangular (equatorial) configuration for ^{245}Es and ^{248}Fm nuclei is shown in Tab. D.1.

Using the same method, the potential energy has been calculated for different arrangements of fragments for the ^{242}Cf. The minimization of potential energy of all the mass and charge asymmetries involved requires for understanding the potential energy landscape of ternary fission of ^{242}Cf. We consider the combinations of the fragments as $A_1 >= A_2 >= A_3$ for avoiding the repetitions. Figure D.1 is the potential energy surface plot in terms of charges where fragments are arranged in $A_1 + A_2 + A_3$ and $A_1 + A_3 + A_2$ way. It is possible to identify different deep minima in Potential energy surface. The minima correspond to stable configuration cluster. Among these, the deepest minima corresponds to (Sn, Ni, Ca). Another deep minima which corresponds to TTF is (Se, Ge, Ge) as labeled in the Fig.

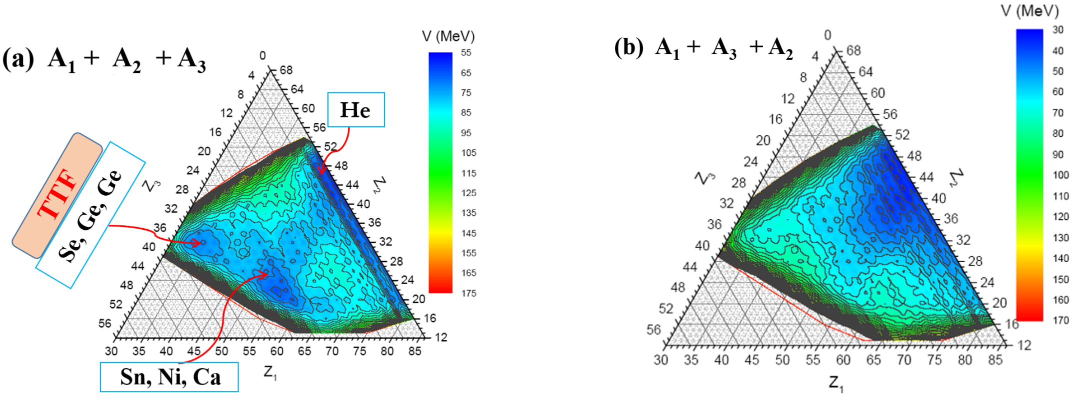

Figure D.1: Potential energy surface as a function of charge number of ternary fission of ^{242}Cf for two different arrangements.

D.1. The ^4He accompanied ternary fission remains the most favorable breakup as labeled.

Fig. D.2 shows the ternary interaction potential for some selected fragmentations as a function of the orientation angle starting from a collinear arrangement leading to a triangular arrangement and the angular momentum for of various three-body breakups of the ^{242}Cf nucleus. The structure of the potential is not significantly changing with the change in angular momentum. The potential is just shifted by changing the angular momentum. The solid line presents the potential when the value of angular momentum is $l = 0\hbar$ and dashed line reflects potential when the value of angular momentum is $l = 40\hbar$. The potential for the case when the fragments are arranged in the order of $A_1 + A_2 + A_3$ (equivalently $A_3 + A_2 + A_1$) is given in the first column (case-I) of Fig. D.2 . Similarly, the fragment arrangement corresponding to Case II and Case III is presented in second and third columns respectively. The touching angle and the corresponding potentials are marked with vertical and horizontal dotted lines for the triangular geometry of all the panels. For the three different arrangements considered, the potential corresponding to the touching configuration remains same . There is a preference for triangular geometry over collinear geometry for very light third fragments when the lightest fragment (A_3) is positioned at the end (keeping either A_2 or A_1 in the middle, Cases I and III). This preference indicated that collinear geometry starts to compete with the triangular geometry with the incensement of the third fragment mass.

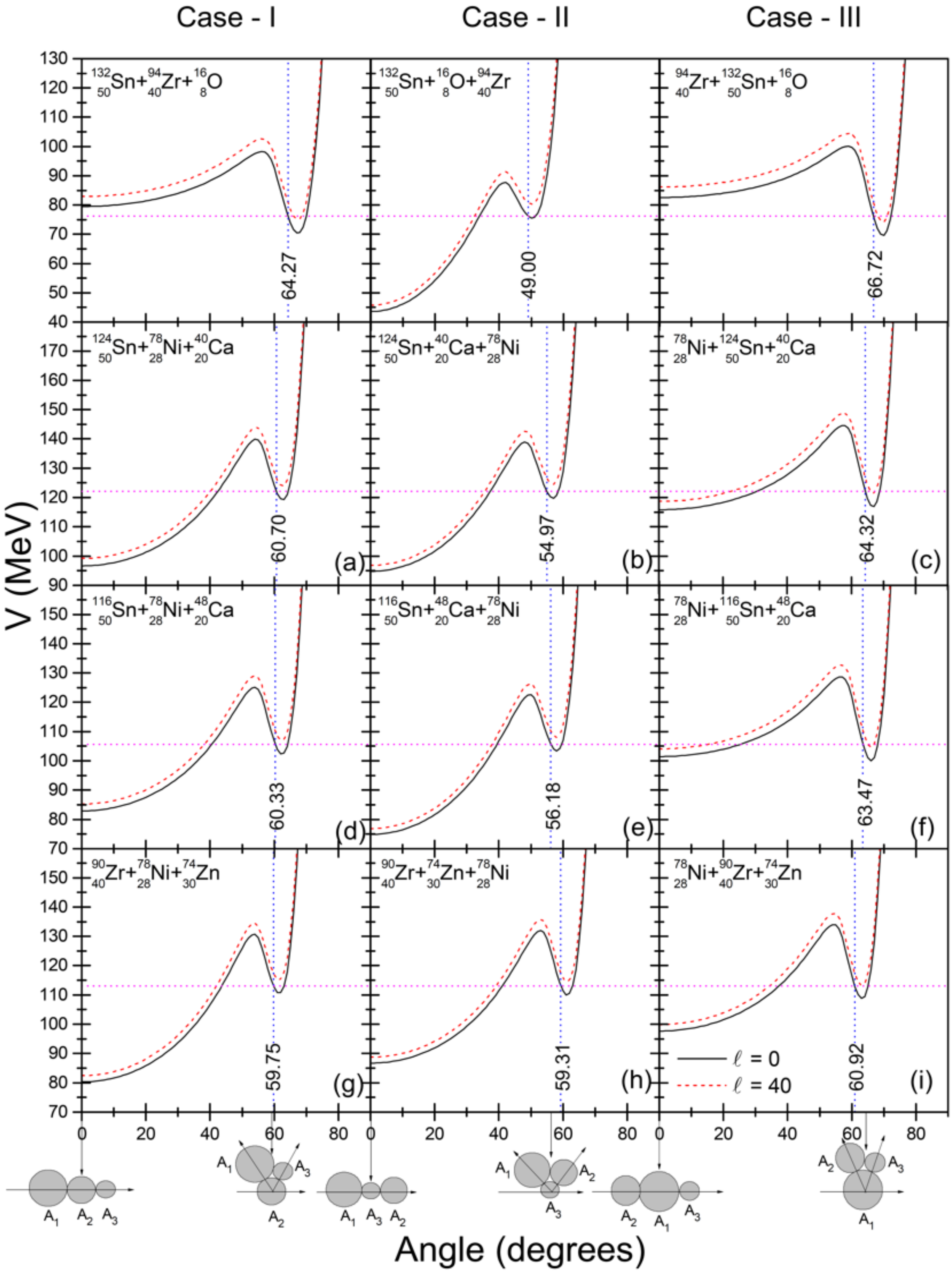

Figure D.2: (Color online) The total ternary fragmentation potential as a function of the orientation angle is presented for three different fragment combinations in three different arrangements for the angular momentum $l = 0\hbar$ and $40\hbar$.

Appendix E

Mass Distributions of Ternary Fission

We want to demonstrate that in a planner geometry, the masses of the three fragments can be calculated by knowing their angles of emission, the velocities of two of these, and the energy of the third one. Let us consider that in a ternary decay, three fragments having masses M_1, M_2, and M_3 are produced. These masses can be written by the following way:

$$\begin{aligned} M_1 &= M_1(\theta_1,\, \theta_2,\, \theta_3,\, V_1,\, V_2,\, E_3), \\ M_2 &= M_2(\theta_1,\, \theta_2,\, \theta_3,\, V_1,\, V_2,\, E_3), \text{ and} \\ M_3 &= M_3(\theta_1,\, \theta_2,\, \theta_3,\, V_1,\, V_2,\, E_3), \end{aligned}$$

where θ, V, and E are the emission angles, velocities and energies corresponding to masses M_1, M_2, and M_3 respectively.

Energy conservation law is:

$$\begin{aligned} &E_p = E_1 + E_2 + E_3 - Q\,, \\ &or,\ M_1(V_1^2 + 2) + M_2(V_2^2 + 2) + 2(E_3 - E_p - M_p - M_t + M_3) = 0. \end{aligned} \tag{E.0.1}$$

The momentum conservation along the perpendicular to the beam direction is:

$$\begin{aligned} &M_p V_p\, Sin\, 0^0 = M_1 V_1\, Sin\theta_1 + M_2 V_2\, Sin\theta_2 + M_3 V_3\, Sin\theta_3\,, \\ &or,\ M_1 = \frac{-M_2 V_2\, Sin\theta_2 - \sqrt{2M_3E_3} Sin\theta_3}{V_1\, Sin\theta_1}. \end{aligned} \tag{E.0.2}$$

The momentum conservation along the beam direction is:

$$M_pV_p = M_1V_1\,Cos\theta_1 + M_2V_2\,Cos\theta_2 + M_3\,\sqrt{\frac{2E_3}{M_3}}\,Cos\theta_3. \tag{E.0.3}$$

Now using equation E.0.2 in the equation E.0.3, we get the following expression of Mass M_2:

$$M_2 = \frac{M_pV_p\,Sin\theta_1 - \sqrt{2M_3E_3}Sin(\theta_1 - \theta_3)}{V_2\,Sin(\theta_1 - \theta_2)} \tag{E.0.4}$$

Now using equation E.0.4 into equation E.0.2, we get

$$M_1 = \frac{-M_pV_p\,Sin\theta_1\,Sin\theta_2 + \sqrt{2M_3E_3}Sin\theta_2\,Sin(\theta_1 - \theta_3) - \sqrt{2M_3E_3}Sin\theta_3\,Sin(\theta_1 - \theta_2)}{V_1\,Sin\theta_1\,Sin(\theta_1 - \theta_2)}. \tag{E.0.5}$$

Now using equation E.0.4 and E.0.5 into equation E.0.1, we get

$$M_3\,\alpha + \sqrt{M_3}\beta + \gamma = 0, \tag{E.0.6}$$

where,

$$\begin{aligned}
\alpha &= 2V_1V_2\,Sin\theta_1\,Sin(\theta_1 - \theta_2),\\
\beta &= \sqrt{2E_3}\,V_2(V_1^2 + 2)\{Sin\theta_2\,Sin(\theta_1 - \theta_3) - Sin\theta_3\,Sin(\theta_1 - \theta_2)\}\\
&\qquad - \sqrt{2E_3}\,V_1(V_2^2 + 2)\,Sin\theta_1\,Sin(\theta_1 - \theta_3),\\
\gamma &= M_p\,V_p\,Sin\theta_1\,\{V_1(V_2^2 + 2)\,Sin\theta_1 - V_2(V_1^2 + 2)\,Sin\theta_2\}\\
&\qquad +2V_1V_2Sin\theta_1\,Sin(\theta_1 - \theta_2)(E_3 - E_p - M_p - M_t).
\end{aligned}$$

The solution of equation E.0.6 is:

$$M_3 = \frac{\beta^2 - 2\alpha\gamma \pm \sqrt{\beta^4 - 4\alpha\beta^2\gamma}}{2\alpha^2}, \tag{E.0.7}$$

- M_1 is calculated from equation E.0.5 by using equation E.0.7.
- M_2 is calculated from equation E.0.4 by using equation E.0.7.
- M_3 is calculated equation E.0.7.

Appendix F

Sequential Ternary Fission

Let us consider that a compound nucleus formed by projectile and target collision, first breaks into two bodies (M_{23} and M_1). Then in second step M_{23} will decay into final two (M_2 and M_3) bodies. So at final stage we get three fragments like as M_1, M_2, and M_3. In the following we will discuss first initial two body decay, then secondary breakup of heavy fragment.

Total Kinetic Energy in the initial system:

$$\begin{aligned} E_{Lab} &= \frac{1}{2} M_p V_p^2 + \frac{1}{2} M_t V_t^2 , \\ or, \;\; V_p &= \sqrt{\frac{2E_{Lab}}{M_p}}. \;\; (V_t = 0) \end{aligned} \tag{F.0.1}$$

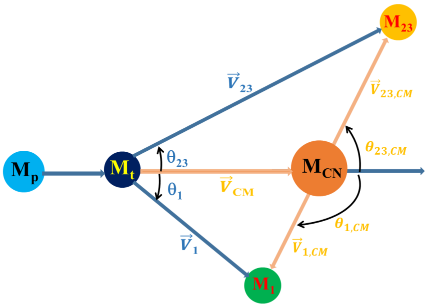

Figure F.1: Initial two body decay in the laboratory and centre of mass frame of reference.

Momentum conservation equation becomes:

$$\begin{aligned}(M_p + M_t)\, V_{CM} &= M_p V_p\,, \\ or,\ V_{CM} &= \frac{M_p\, V_p}{M_p + M_t}. \end{aligned} \tag{F.0.2}$$

In the centre-of-mass frame of reference, the centre-of-mass of the two colliding particle is at rest. It follows that:

$$\begin{aligned} M_p V_{p,CM} + M_t V_{t,CM} &= (M_p + M_t)\, V_{CM,CM}\,, \\ or,\ M_p V_{p,CM} &= -M_t V_{t,CM}.\ (V_{CM,CM} = 0) \end{aligned} \tag{F.0.3}$$

Velocity of centre of mass in Lab frame = - Velocity of target in Centre of mass frame,

$$V_{CM,lab} = -V_{t,CM}. \tag{F.0.4}$$

From equations F.0.4 and F.0.2,

$$-V_{t,CM} = \frac{M_p}{M_p + M_t}\, V_p\,,$$

$$or,\ V_{t,CM} = -\frac{M_p}{M_p + M_t}\, V_p\,, \tag{F.0.5}$$

$$or,\ V_{t,CM} = -\frac{\sqrt{2E_{Lab} M_p}}{M_p + M_t}. \tag{F.0.6}$$

From equations F.0.3 and F.0.5,

$$V_{p,CM} = -\frac{M_t}{M_p}\left[-\frac{M_p}{M_p + M_t}\, V_p\right],$$

$$or,\ V_{p,CM} = \frac{M_t}{M_p + M_t}\sqrt{\frac{2E_{Lab}}{M_p}}.\ (using\ F.0.1) \tag{F.0.7}$$

Projectile energy in centre of mass frame:

$$E_{p,CM} = \frac{1}{2} M_p V_{p,CM}^2\,,$$

$$or,\ E_{p,CM} = \frac{1}{2} M_p \left(\frac{M_t}{M_p + M_t}\right)^2 \frac{2E_{Lab}}{M_p}\,,\ (using\ F.0.7) \tag{F.0.8}$$

$$or,\ E_{p,CM} = \left(\frac{M_t}{M_p + M_t}\right)^2 E_{Lab}. \tag{F.0.9}$$

Target energy in centre of mass frame:

$$\begin{aligned}
E_{t,CM} &= \frac{1}{2} M_t V_{t,CM}^2\,, \\
or,\ E_{t,CM} &= \frac{1}{2} M_t \frac{2 E_{Lab} M_p}{(M_p + M_t)^2}\,, \quad (using\ F.0.6) \\
or,\ E_{t,CM} &= \frac{M_p M_t}{(M_p + M_t)^2}\, E_{Lab}.
\end{aligned} \tag{F.0.10}$$

In the initial centre of mass frame, The total Kinetic Energy:

$$\begin{aligned}
E_{i,CM} &= E_{p,CM} + E_{t,CM}\,, \\
or,\ E_{i,CM} &= \left(\frac{M_t}{M_p + M_t}\right)^2 E_{Lab} + \frac{M_p M_t}{(M_p + M_t)^2} E_{Lab}\,, \quad (using\ F.0.9\ and\ F.0.10) \\
or,\ E_{i,CM} &= \frac{M_t}{M_p + M_t}\, E_{Lab}.
\end{aligned} \tag{F.0.11}$$

The conservation of linear momentum require that the final system shall have no net linear momentum in the centre of mass frame of reference ($V_{CM,CM} = 0$). Thus

$$\begin{aligned}
(M_p + M_t)\, V_{CM,CM} &= M_1 V_{1,CM} + M_{23} V_{23,CM}\,, \\
or,\ V_{23,CM} &= -\frac{M_1}{M_{23}}\, V_{1,CM}.
\end{aligned} \tag{F.0.12}$$

After the interaction, the total kinetic energy available in the final centre of mass frame of reference is,

$$E_{f,CM} = E_{i,CM} + Q_1, \tag{F.0.13}$$

here Q_1 is the decay energy of the initial two body breakup.

$E_{f,CM}$ will be the sum of kinetic energies of the fragments in the centre of mass frame:

$$\begin{aligned}
E_{f,CM} &= \frac{1}{2} M_1 V_{1,CM}^2 + \frac{1}{2} M_{23} V_{23,CM}^2\,, \\
or,\ E_{i,CM} + Q_1 &= \frac{1}{2} M_1 V_{1,CM}^2 + \frac{1}{2} M_{23} V_{23,CM}^2, \quad (using\ equ.\ F.0.13) \\
or,\ \frac{1}{2} M_1 V_{1,CM}^2 + \frac{1}{2} M_{23} \left(\frac{M_1^2}{M_{23}^2} V_{1,CM}^2\right) &= E_{i,CM} + Q_1\,, \quad (using\ equ.\ F.0.12) \\
or,\ V_{1,CM} &= \left[\frac{2\, M_{23}}{M_1 (M_1 + M_{23})} \left(\frac{M_t\, E_{Lab}}{M_p + M_t} + Q_1\right)\right]^{1/2}. \quad (using\ equ.\ F.0.11)
\end{aligned} \tag{F.0.14}$$

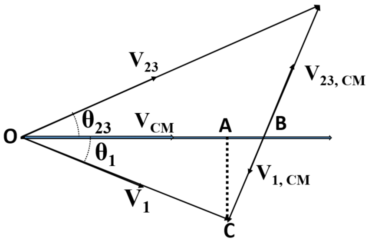

Figure F.2: Simplified initial two body decay in the laboratory and centre of mass frame of reference.

From the $\triangle$ $OAC, AC \;=\; V_1\, Sin\theta_1$ and $OA \;=\; V_1\, Cos\theta_1$.

From the $\triangle$ ABC,

$$V_{1,CM}^2 = (AB)^2 + (AC)^2\,,$$

$$or,\;\; V_{1,CM}^2 = V_{CM}^2 + V_1^2 - 2\, V_{CM}\, V_1\, Cos\theta_1, \tag{F.0.15}$$

Where,

$$V_1 \;=\; V_{CM}\, Cos\theta_1 \pm \sqrt{V_{1,CM}^2 - V_{CM}^2\, Sin_{\theta_1}^2}. \tag{F.0.16}$$

Energy of first fragment:

$$E_1 \;=\; \frac{1}{2} M_1 V_1^2. \tag{F.0.17}$$

Energy conservation:

$$E_{lab} = E_1 + E_{23} - Q_1\,,$$

$$or,\;\; E_{23} = E_{lab} + Q_1 - E_1. \tag{F.0.18}$$

Again,

$$E_{23} \;=\; \frac{1}{2} M_{23} V_{23}^2\,,$$

$$or,\;\; V_{23} \;=\; \sqrt{\frac{2\, E_{23}}{M_{23}}}. \tag{F.0.19}$$

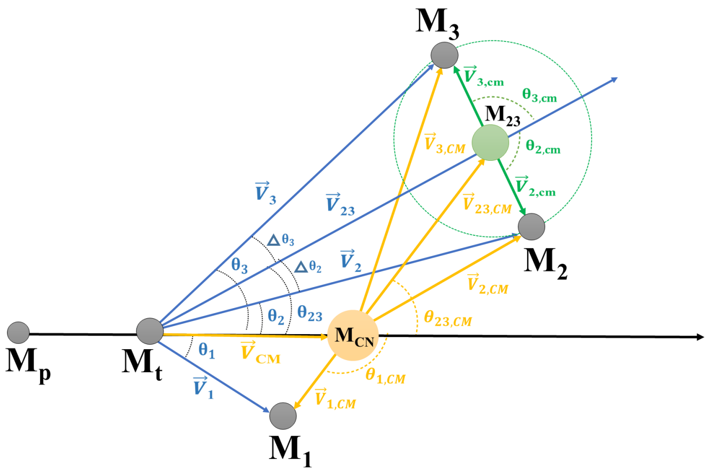

Figure F.3: Kinematics plot for 3 body sequential fission.

Momentum conservation in the beam direction is:

$$M_pV_p = M_1V_1\,Cos\theta_1 + M_{23}V_{23}\,Cos\theta_{23}\,,$$
$$or,\ \theta_{23} = \sqrt{\frac{M_pV_p - M_1V_1\,Cos\theta_1}{M_{23}V_{23}}}. \tag{F.0.20}$$

Figure F.3 is the kinematics plot for three body sequential fission. After forming the compound nucleus M_{CN}, first it breaks into 2 body M_{23} and M_1. At 2nd step, M_{23} will decay into M_2 and M_3 and the amount of energy released is Q_2.

Momentum conservation in second interacting system:

$$M_2V_{2,cm} = M_3V_{3,cm}\,,$$
$$or,\ V_{3,cm} = \frac{M_2V_{2,cm}}{M_3}. \tag{F.0.21}$$

Q Value equation becomes:

$$Q_2 = \frac{1}{2}M_2V_{2,cm}^2 + \frac{1}{2}M_3V_{3,cm}^2\,,$$
$$or,\ Q_2 = \frac{1}{2}M_2V_{2,cm}^2 + \frac{1}{2}M_3\,(\frac{M_2V_{2,cm}}{M_3})^2\,,\ (using\ F.0.21)$$
$$or,\ V_{2,cm} = \sqrt{\frac{2M_3Q_2}{M_2\,(M_2+M_3)}} = \sqrt{\frac{2M_3Q_2}{M_2\,M_{23}}}. \tag{F.0.22}$$

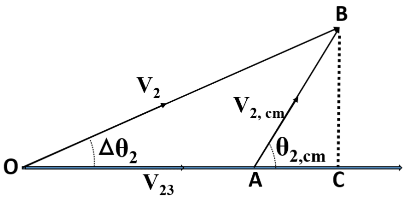

Figure F.4: Simplified centre of mass frame of reference of final interacting system for 2nd fragment.

From equation F.0.21,

$$\begin{aligned} V_{3,cm} &= \frac{M_2}{M_3}\sqrt{\frac{2M_3Q_2}{M_2\,M_{23}}}\,, \\ or,\;\; V_{3,cm} &= \sqrt{\frac{2M_2Q_2}{M_3\,M_{23}}}. \end{aligned} \tag{F.0.23}$$

Let us figure out the breakup of mass M_{23} into mass M_2 and M_3 separately.

Fig. F.4 shows the case of 2nd fragment and from the $\triangle\ OCB$ it is possible to write the following relation:

$$(OB)^2 = (OC)^2 + (BC)^2 = (OA + AC)^2 + (BC)^2. \tag{F.0.24}$$

From the $\triangle\ ABC$,

$$\begin{aligned} Cos\theta_{2,cm} &= \frac{AC}{BC}\,, \\ or,\;\; AC &= AB\ Cos\theta_{2,cm} = V_{2,cm}\ Cos\theta_{2,cm}, \end{aligned} \tag{F.0.25}$$

and,

$$\begin{aligned} Sin\theta_{2,cm} &= \frac{BC}{AB}\,, \\ or,\;\; BC &= AB\ Sin\theta_{2,cm} = V_{2,cm}\ Sin\theta_{2,cm}. \end{aligned} \tag{F.0.26}$$

Using equations F.0.25 and F.0.26 in equation F.0.24,

$$\begin{aligned} (OB)^2 = V_2^2 &= (V_{23} + V_{2,cm}\ Cos\theta_{2,cm})^2 + (V_{2,cm}\ Sin\theta_{2,cm})^2\,, \\ or,\;\; V_2 &= \sqrt{V_{23}^2 + V_{2,cm}^2 + 2\,V_{23}\,V_{2,cm}\,Cos\theta_{2,cm}}. \end{aligned} \tag{F.0.27}$$

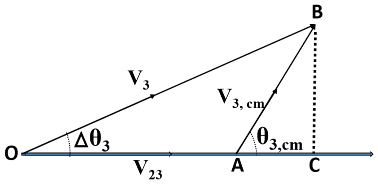

Figure F.5: Simplified centre of mass frame of reference of final interacting system for 3rd fragment.

From the $\triangle\, OBC$,

$$Tan\triangle\,\theta_2 = \frac{BC}{OC} = \frac{BC}{OA + AC},$$
$$or,\ Tan\triangle\,\theta_2 = \frac{V_{2,cm}\,Sin\theta_{2,cm}}{V_{23} + V_{2,cm}\,Cos\theta_{2,cm}},\ (using\ F.0.25\ and\ F.0.26)$$
$$or,\ \triangle\,\theta_2 = Tan^{-1}\left(\frac{V_{2,cm}\,Sin\theta_{2,cm}}{V_{23} + V_{2,cm}\,Cos\theta_{2,cm}}\right). \quad (F.0.28)$$

Therefore,

$$\theta_2 = \theta_{23} - \triangle\,\theta_2. \quad (F.0.29)$$

Similarly, from Fig. F.5 for the 3rd fragment we can deduce the following relations:

$$V_3 = \sqrt{V_{23}^2 + V_{3,cm}^2 + 2\,V_{23}\,V_{3,cm}\,Cos\theta_{3,cm}}, \quad (F.0.30)$$

and,

$$\triangle\,\theta_3 = Tan^{-1}\left(\frac{V_{3,cm}\,Sin\theta_{3,cm}}{V_{23} + V_{3,cm}\,Cos\theta_{3,cm}}\right). \quad (F.0.31)$$

Therefore,

$$\theta_3 = \theta_{23} + \triangle\,\theta_3. \quad (F.0.32)$$

- The energy of first ($E_1 = M_1 V_1^2\,/\,2$) fragment can be calculated by using equation F.0.16.
- The energy of second ($E_2 = M_2 V_2^2\,/\,2$) fragment can be calculated by using equation F.0.27.

- The angle of second (θ_2) fragment can be calculated from equation F.0.29 by using equations F.0.28 and F.0.20.

- The energy of second ($E_3 = M_3 V_3^2 / 2$) fragment can be calculated by using equation F.0.30.

- The angle of third (θ_3) fragment can be calculated from equation F.0.32 by using equations F.0.31 and F.0.20.

Bibliography

[1] O. Hahn and F. Strassmann. Uber den nachweis und das verhalten der bei der bestrahlung des urans mittels neutronen entstehenden erdalkalimetalle. *Naturwissenschaften*, 27(1):11 – 15, 1939. URL `https://doi.org/10.1007/BF01488241`.

[2] O. Hahn and F. Strassmann. Nachweis der entstehung aktiver bariumisotope aus uran und thorium durch neutronenbestrahlung; nachweis weiterer aktiver bruchstucke bei der uranspaltung; nachweis weiterer aktiver bruchstucke bei der uranspaltung. *Naturwissenschaften*, 27(6):89 – 95, 1939. URL `https://doi.org/10.1007/BF01488988`.

[3] L. Meitner and O.R. Frisch. Disintegration of uranium by neutrons: a new type of nuclear reaction. *Nature*, 143:239 – 240, 1939. URL `https://www.nature.com/nature/journal/v143/n3615/pdf/143239a0.pdf`.

[4] N. Bohr and J.A. Wheeler. The mechanism of nuclear fission. *Phys. Rev.*, 56(5):426 – 450, 1939. URL `https://doi.org/10.1103/PhysRev.56.426`.

[5] R. Brandt. Ternary fission. *Angew. Chem. internat. Edit.*, 10(12):890, 1971. URL `http://onlinelibrary.wiley.com/doi/10.1002/anie.197108901/full`.

[6] C. Wagemans. *Ternary Fission in The Nuclear Fission Process.* edited by Cyriel Wagemans (CRC Press, Boca Raton, FL), Chap. 12, 1991. URL `https://www.crcpress.com/The-Nuclear-Fission-Process/Wagemans/p/book/9780849354342`.

[7] F. Gönnenwein. Ternary and quaternary fission. *Nuclear Physics A*, 734:213 – 216, 2004. URL `https://doi.org/10.1016/j.nuclphysa.2004.01.037`.

[8] F. Gönnenwein, M. Mutterer, and Yu. Kopatch. The mechanism of nuclear fission. *Europhys. News*, 36(1):11, 2005. URL `https://doi.org/10.1051/epn:2005104`.

[9] F. Gönnenwein *et al.* Seminar on fission. page 59. World Scientific, Singapore, 1999.

[10] Yu.V. Pyatkov *et al.* Collinear cluster tri-partition of $^{252}Cf(sf)$ and in the $^{235}U(n_{th}, f)$ reaction. *Eur. Phys. J. A*, 45:29, 2010. URL `https://doi.org/10.1140/epja/i2010-10988-8`.

[11] Yu.V. Pyatkov *et al.* Collinear cluster tri-partition channel in reaction $^{235}U(n_{th}, f)$. *Phys. Atom. Nucl.*, 73(8):1309, 2010. URL `https://doi.org/10.1134/S1063778810080041`.

[12] Yu.V. Pyatkov *et al.* Presumable scenario of one of the collinear cluster tripartition modes. *Int. J. Mod. Phys. E*, 20(4):1008, 2011. URL `https://doi.org/10.1142/S0218301311019155`.

[13] Yu.V. Pyatkov *et al.* Collinear cluster tri-partition (CCT) of $^{252}Cf(sf)$: New aspects from neutron gated data. *Eur. Phys. J. A*, 48:94, 2012. URL `https://doi.org/10.1140/epja/i2012-12094-5`.

[14] H.G. Ortlepp *et al.* The 4π-fragment-spectrometer fobos. *Nucl. Instrum. Methods A*, 403(1):65, 1998. URL `https://doi.org/10.1016/S0168-9002(97)00777-8`.

[15] D.N. Poenaru *et al.* True ternary fission. *Romanian Reports in Physics*, 55(4):549, 2003. URL `http://www.rrp.infim.ro/2003_55_4/Poe.pdf`.

[16] D.N. Poenaru, R.A. Gherghescu, and W. Greiner. Complex fission phenomena. *Nucl. Phys. A*, 747(2-4):182, 2005. URL `https://doi.org/10.1016/j.nuclphysa.2004.09.104`.

[17] Yu.V. Pyatkov *et al.* Island of the high yields of $^{252}Cf(sf)$ collinear tripartition in the fragment mass space. *Rom. Rep. Phys.*, 59(2):569, 2007. URL `https://www.researchgate.net/profile/Yu_Pyatkov/publication/228643274_ISLAND_OF_THE_HIGH_YIELDS_OF_252Cf_sf_COLLINEAR_TRIPARTITION_IN_THE_FRAGMENT_MASS_SPACE/links/0deec51bc39c8dce07000000.pdf`.

[18] D.V. Kamanin and Yu.V. Pyatkov. Clusterization in ternary fission. *Lect. Notes Phys.*, 875:183, 2013. URL `https://doi.org/10.1007/978-3-319-01077-9_6`.

[19] Yu.V. Pyatkov *et al.* Proceeding of the international symposium on exotic nuclei EXON-2001, Baikal Lake. page 181, 2001.

[20] L. Rosen and A.M. Hudson. Symmetrical tripartition of U^{235}, by thermal neutrons. *Phys. Rev.*, 78(5):533, 1950. URL `https://doi.org/10.1103/PhysRev.78.533`.

[21] M.L. Muga, H.R. Bowman, and S.G. Thompson. Tripartition in the spontaneous fission decay of Cf^{252}. *Phys. Rev.*, 121(1):270, 1961. URL `https://doi.org/10.1103/PhysRev.121.270`.

[22] M.L. Muga. Proceedings of the IAEA symposium on physics and chemistry of fission, Salzburg (IAEA, Vienna). volume 2, page 409, 1965.

[23] M.L. Muga, C.R. Rice, and W.A. Sedlacek. Ternary fission of heavy nuclei. *Phys. Rev. Lett.*, 18(11):404, 1967. URL `https://doi.org/10.1103/PhysRevLett.18.404`.

[24] M.L. Muga and C.R. Rice. Proceedings of the second IAEA symposium on physics and chemistry of fission, Salzburg (IAEA, Vienna). page 107, 1969.

[25] M.L. Muga. Ternary fission of U^{235} induced by thermal neutrons. *Phys. Rev. Lett.*, 11 (3):129, 1963. URL `https://doi.org/10.1103/PhysRevLett.11.129`.

[26] M.L. Muga, C.R. Rice, and W.A. Sedlacek. Ternary fission of uranium-236* and -234. *Phys. Rev.*, 161(4):1266, I 1967. URL `https://doi.org/10.1103/PhysRev.161.1266`.

[27] R.L. Fleischer, P.B. Price, and R.M. Walker. Ternary fission of heavy compound nuclei in thorite track detectors. *Phys. Rev.*, 143(3):943, 1966. URL `https://doi.org/10.1103/PhysRev.143.943`.

[28] R.H. Iyer and J.W. Cobble. Ternary fission of ^{238}U induced by intermediate-energy helium ions. *Phys. Rev.*, 172(4):1186, 1968. URL `https://doi.org/10.1103/PhysRev.172.1186`.

[29] H.J. Becker *et al*. Ternary fission induced by 540 MeV Fe ions on uranium. *Phys. Lett. B*, 50(4):445, 1974. URL `https://doi.org/10.1016/0370-2693(74)90256-1`.

[30] P. Schall, P. Heeg, M. Mutterer, and J.P. Theobald. On symmetric tripartition in the spontaneous fission of ^{252}Cf. *Phys. Lett. B*, 191(4):339, 1987. URL `https://doi.org/10.1016/0370-2693(87)90619-8`.

[31] R.W. Stoenner and M. Hillman. Search for radiochemical evidence for ternary fission of ^{235}U by thermal neutrons. *Phys. Rev.*, 142(3):716 – 719, 1966. URL `https://doi.org/10.1103/PhysRev.142.716`.

[32] P. Vater and R. Brandt. Ternary fission of uranium induced by 414 MeV Ar-ions as studied with a hole detector. *Radiochimica Acta*, 21(3):191, 1974. URL `https://doi.org/10.1524/ract.1974.21.34.191`.

[33] R.D. Present and J.K. Knipp. On the dynamics of complex fission. *Phys. Rev.*, 57(8): 751, 1940. URL `https://doi.org/10.1103/PhysRev.57.751`.

[34] R.D. Present. Possibility of ternary fission. *Phys. Rev.*, 59:466, 1941.

[35] S.L. Whetstone and T.D. Thomas. Light charged particles from spontaneous fission of ^{252}Cf. *Phys. Rev.*, 154(4):1174, 1967. URL `https://doi.org/10.1103/PhysRev.154.1174`.

[36] G.M. Raisbeck and T.D. Thomas. Light nuclei emitted in the fission of ^{252}Cf. *Phys. Rev.*, 172(4):1272, 1968. URL `https://doi.org/10.1103/PhysRev.172.1272`.

[37] J.K. Hwang *et al.* ^{5}He ternary fission yields of ^{252}Cf and $^{235}U(n, f)$. *Phys. Rev. C*, 61 (4):047601, 2000. URL `https://doi.org/10.1103/PhysRevC.61.047601`.

[38] G.M. Ter-Akopian *et al.* Phys. at. nucl ^{252}Cf from the gammasphere facility. *Phys. At. Nucl.*, 67(10):1860, 2004. URL `https://doi.org/10.1134/1.1811191`.

[39] A.V. Daniel *et al.* Ternary fission of ^{252}Cf: 3368 KeV γ radiation from ^{10}Be fragments. *Phys. Rev. C*, 69(4):041305, 2004. URL `https://doi.org/10.1103/PhysRevC.69.041305`.

[40] V.P. Perelygin *et al.* Ternary fission produced in Au, Bi, Th and U with Ar ions. *Nucl. Phys. A*, 127(3):577, 1969. URL `https://doi.org/10.1016/0375-9474(69)91029-X`.

[41] F. Gönnenwein *et al.* Cold binary and ternary fission. *Nuovo Cimento A*, 110(9):1089, 1997. URL `https://doi.org/10.1007/BF03035950`.

[42] U. Köster *et al.* Ternary fission yields of $^{241}Pu(n_{th}, f)$. *Nucl. Phys. A*, 652(4):371, 1999. URL `https://doi.org/10.1016/S0375-9474(99)00115-3`.

[43] C.-M. Herbach *et al.* Search for mass-symmetric ternary fission in the reactions ^{14}N(53AMeV) $+^{197}$ Au and ^{232}Th. *Nucl. Phys. A*, 712(3):207, 2002. URL `https://doi.org/10.1016/S0375-9474(02)01242-3`.

[44] I. Tsekhanovich, Z. Buyukmumcu, M. Davi, H.O. Denschlag, F. Gonnenwein, and S.F. Boulyga. Ternary fission yields in ^{252}C$f(n_{th}, f)$. *Phys. Rev. C*, 67(3):034610, 2003. URL `https://doi.org/10.1103/PhysRevC.67.034610`.

[45] W.J. Swiatecki. 2nd un intern. conf. on the peaceful uses of atomic energy. volume 15, page 248, Geneva, 1958.

[46] H. Diehl and W. Greiner. Theory of ternary fission in the liquid drop model. *Nucl. Phys. A*, 229(1):29, 1974. URL `https://doi.org/10.1016/0375-9474(74)90673-3`.

[47] J. Maruhn and W. Greiner. The asymmetrie two center shell model. *Z. Phys. A*, 251 (5):431, 1972. URL `https://doi.org/10.1007/BF01391737`.

[48] A.R. Degheidy and J.A. Maruhn. A three-center shell model for ternary fission. *Z. Phys. A*, 290(2):205, 1979. URL `https://doi.org/10.1007/BF01408116`.

[49] A.V. Karpov and A. Adel. Ternary clusterization of heavy nuclear systems. 4th S*outh* A*frica* - JINR SYMPOSIUM*:* F*ew to Many Body Systems: Models, Methods and Applications*, page 109, 2015.

[50] A.V. Karpov. Ternary fission of a heavy nuclear system within a three-center shell model. *Phys. Rev. C*, 94(6):064615, 2016. URL `https://doi.org/10.1103/PhysRevC.94.064615`.

[51] I.V. Panov, E. Kolbe, B. Pfeiffer, T. Rauscher, K.L. Kratz, and F.K. Thielemann. Calculations of fission rates for r-process nucleosynthesis. *Nucl. Phys. A*, 747(2):633, 2005. URL `https://doi.org/10.1016/j.nuclphysa.2004.09.115`.

[52] G. Royer and J. Moignen. Binary and ternary fission of hot and rotating nuclei. *J. Phys. G: Nucl. Part. Phys.*, 18(11):1781–1792, 1992. URL `https://doi.org/10.1088/0954-3899/18/11/011`.

[53] V.I. Zagrebaev and Walter Greiner. Giant nuclear systems of molecular type. *Clusters in Nuclei, Lecture Notes in Physics, 818*, 1:267 – 315, 2010. URL `http://www.springer.com/in/book/9783642138980`.

[54] K. Manimaran and M. Balasubramaniam. Ternary fission fragmentation of ^{252}Cf for all possible third fragments. *Eur. Phys. J. A*, 45:293, 2010. URL `https://doi.org/10.1140/epja/i2010-11000-7`.

[55] K. Manimaran and M. Balasubramaniam. All possible ternary fragmentations of ^{252}Cf in collinear configuration. *Phys. Rev. C*, 83(3):034609, 2011. URL `https://doi.org/10.1103/PhysRevC.83.034609`.

[56] K.R. Vijayaraghavan, W. von Oertzen, and M. Balasubramaniam. Kinetic energies of cluster fragments in ternary fission of ^{252}Cf. *Eur. Phys. J. A*, 48:27, 2012. URL `https://doi.org/10.1140/epja/i2012-12027-4`.

[57] K. Manimaran and M. Balasubramaniam. Three-cluster model for the α-accompanied fission of californium nuclei. *Phys. Rev. C*, 79(2):024610, 2009. URL `https://doi.org/10.1103/PhysRevC.79.024610`.

[58] K. Manimaran and M. Balasubramaniam. Deformation and orientation effects in the ternary fragmentation potential of the ^{4}He- and ^{10}Be-accompanied fission of the ^{252}Cf nucleus. *J. Phys. G: Nucl. Part. Phys.*, 37:045104, 2010. URL `https://doi.org/10.1088/0954-3899/37/4/045104`.

[59] K.R. Vijayaraghavan, M. Balasubramaniam, and W. von Oertzen. Collinear versus triangular geometry: A ternary fission study. *Phys. Rev. C*, 90(2):024601, 2014. URL `https://doi.org/10.1103/PhysRevC.90.024601`.

[60] M. Balasubramaniam, K.R. Vijayaraghavan, and C. Karthikraj. Ternary fission. *Pramana-J.Phys.*, 85(3):423 – 43, 2015. URL `https://doi.org/10.1007/s12043-015-1057-x`.

[61] K.R. Vijayaraghavan, M. Balasubramaniam, and W. von Oertzen. True ternary fission. *Phys. Rev. C*, 91(4):044616, 2015. URL `https://doi.org/10.1103/PhysRevC.91.044616`.

[62] M.G. Itkis, E. Vardaci, I.M. Itkis, G.N. Knyazheva, and E.M. Kozulin. Fusion and fission of heavy and superheavy nuclei (experiment). *Nucl. Phys. A*, 944:204, 2015. URL `https://doi.org/10.1016/j.nuclphysa.2015.09.007`.

[63] V.I. Zagrebaev, A.V. Karpov, and W. Greiner. True ternary fission of superheavy nuclei. *Phys. Rev. C*, 81(4):044608, 2010. URL https://doi.org/10.1103/PhysRevC.81.044608.

[64] J. Péter *et al.* Quasi-fission and other strongly damped collisions between ^{63}C*u* ions and ^{197}A*u* nuclei. *Nucl. Phys. A*, 279(1):110, 1977. URL https://doi.org/10.1016/0375-9474(77)90424-9.

[65] M.G. Itkis *et al.* Proc. int. conf. on fusion dynamics at the extremes (dubna). page 93. World Scientific, 2001.

[66] M.G. Itkis *et al.* Shell effects in fission and quasi-fission of heavy and superheavy nuclei. *Nucl. Phys. A*, 734:136 – 147, 2004. URL https://doi.org/10.1016/j.nuclphysa.2004.01.022.

[67] R. Bock *et al.* Dynamics of the fusion process. *Nucl. Phys. A*, 388(2):334, 1982. URL https://doi.org/10.1016/0375-9474(82)90420-1.

[68] J. Tōke *et al.* Quasi-fission the mass-drift mode in heavy-ion reactions. *Nucl. Phys. A*, 440(2):327, 1985. URL https://doi.org/10.1016/0375-9474(85)90344-6.

[69] W.Q. Shen *et al.* Fission and quasifission in U-induced reactions. *Phys. Rev. C*, 36(1): 115, 1987. URL https://doi.org/10.1103/PhysRevC.36.115.

[70] M.G. Itkis *et al.* The process of fusion-fission of superheavy nuclei. *Internat. J. Mod. Phys. E*, 16(4):957, 2007. URL https://doi.org/10.1142/S0218301307006423.

[71] V.V. Volkov. Reactions of deep-inelastic transfer (moscow: Energoatomizdat). *(in Russian)*, 1984.

[72] W.J. Swiatecki. The dynamics of nuclear coalescence or reseparation. *Phys. Scr.*, 24 (1B):113 – 122, 1981. URL https://doi.org/10.1088/0031-8949/24/1B/007.

[73] H. Abe. *KEK Preprint 8-26, KEK TH-128.* 1986.

[74] R. du Rietz *et al.* Mapping quasifission characteristics and timescales in heavy element formation reactions. *Phys. Rev. C*, 88(5):054618, 2013. URL https://doi.org/10.1103/PhysRevC.88.054618.

[75] R. Bass. Fusion of heavy nuclei in a classical model. *Nucl. Phys. A*, 231(1):45 – 63, 1974. URL `https://doi.org/10.1016/0375-9474(74)90292-9`.

[76] D.J. Hinde, M. Dasgupta, J.R. Leigh, J.C. Mein, C.R. Morton, J.O. Newton, and H. Timmers. Conclusive evidence for the influence of nuclear orientation on quasifission. *Phys. Rev. C*, 53(3):1290 – 1300, 1996. URL `https://doi.org/10.1103/PhysRevC.53.1290`.

[77] J.C. Mein, D.J. Hinde, M. Dasgupta, J.R. Leigh, J.O. Newton, and H. Timmers. Precise fission fragment anisotropies for the ^{12}C + ^{232}Th reaction: Supporting the nuclear orientation dependence of quasifission. *Phys. Rev. C*, 55(3):R995 – R998, 1997. URL `https://doi.org/10.1103/PhysRevC.55.R995`.

[78] D.J. Hinde *et al.* Fusion-fission versus quasifission: Effect of nuclear orientation. *Phys. Rev. Lett.*, 74(8):1295 – 1298, 1995. URL `https://doi.org/10.1103/PhysRevLett.74.1295`.

[79] A. Stefanini *et al.* Fusion-evaporation cross-sections for coulomb barrier ^{48}Ca + ^{154}Sm near the coulomb barrier. *Eur. Phys. J. A*, 23:473 – 480, 2005. URL `https://doi.org/10.1140/epja/i2004-10109-6`.

[80] G.N. Knyazheva *et al.* Quasifission processes in ^{40,48}Ca + ^{144,154}Sm reactions. *Phys. Rev. C*, 75(6):064602, 2007. URL `https://doi.org/10.1103/PhysRevC.75.064602`.

[81] K. Nishio *et al.* Evidence for quasifission in the sub-barrier reaction of ^{30}Si + ^{238}U. *Phys. Rev. C*, 82(4):044604, 2010. URL `https://doi.org/10.1103/PhysRevC.82.044604`.

[82] K. Nishio *et al.* Evidence of complete fusion in the sub-barrier ^{16}O + ^{238}U reaction. *Phys. Rev. Lett.*, 93(16):162701, 2004. URL `https://doi.org/10.1103/PhysRevLett.93.162701`.

[83] K. Nishio *et al.* Effects of nuclear orientation on the mass distribution of fission fragments in the reaction of ^{36}S + ^{238}U. *Phys. Rev. C*, 77(6):064607, 2008. URL `https://doi.org/10.1103/PhysRevC.77.064607`.

[84] K. Nishio *et al.* Nuclear orientation in the reaction ^{34}S + ^{238}U and synthesis of the new isotope ^{268}H*s*. *Phys. Rev. C*, 82(2):024611, 2010. URL `https://doi.org/10.1103/PhysRevC.82.024611`.

[85] A.Ya. Rusanov *et al.* Properties of mass-energy distributions of fission fragments and gamma-ray multiplicity in ^{18}O + ^{208}P*b* reaction. Proceedings of the 2nd International Conference on Current Problems in Nuclear Physics and Atomic Energy (NPAE-Kyiv2008), June 9 to June 15, 2008, Kyiv, Ukraine. URL `http://www.kinr.kiev.ua/NPAE_Kyiv2008/proceedings/`.

[86] A.Yu. Chizhov *et al.* Unexpected entrance-channel effect in the fission of ^{216}R*a*. *Phys. Rev. C*, 67(1):011603, 2003. URL `https://doi.org/10.1103/PhysRevC.67.011603`.

[87] V.I. Zagrebaev and W. Greiner. Unified consideration of deep inelastic, quasi-fission and fusion-fission phenomena. *J. Phys. G: Nucl. Part. Phys.*, 31(7):825 – 844, 2005. URL `https://doi.org/10.1088/0954-3899/31/7/024`.

[88] M.G. Itkis *et al.* The processes of fusion-fission and quasi-fission of superheavy nuclei. *Nucl. Phys. A*, 787:150 – 159, 2007. URL `https://doi.org/10.1016/j.nuclphysa.2006.12.026`.

[89] D.J. Hinde *et al.* Neutron multiplicities in heavy-ion-induced fission: Timescale of fusion-fission. *Nucl. Phys. A*, 452(3):550–572, 1986. URL `https://doi.org/10.1016/0375-9474(86)90214-9`.

[90] G.N. Knyazheva, I.M. Itkis, and E.M. Kozulin. The time scale of quasifission process in reactions with heavy ions. *J. Phys. Conf. Ser.*, 515:012009, 2014. URL `https://doi.org/10.1088/1742-6596/515/1/012009`.

[91] E.M. Kozulin *et al.* Investigation of the reaction ^{64}N*i* + ^{238}U being an option of synthesizing element 120. *Phys. Lett. B*, 686:227 – 232, 2010. URL `https://doi.org/10.1016/j.physletb.2010.02.041`.

[92] I.M. Itkis *et al.* Fission and quasifission modes in heavy-ion-induced reactions leading to the formation of Hs. *Phys. Rev. C*, 83(6):064613, 2011. URL `https://doi.org/10.1103/PhysRevC.83.064613`.

[93] http://nrv.jinr.ru/nrv/.

[94] U. Brosa, S. Grossmann, and A. Muller. Nuclear scission. *Phys. Rep.*, 197(4):167 – 262, 1990. URL `https://doi.org/10.1016/0370-1573(90)90114-H`.

[95] E. Williams *et al.* Evolution of signatures of quasifission in reactions forming curium. *Phys. Rev. C*, 88(3):034611, 2013. URL `https://doi.org/10.1103/PhysRevC.88.034611`.

[96] C. Wagemans *et al.* Triton and alpha emission in the thermal-neutron-induced ternary fission of ^{233}U, ^{235}U, ^{239}P*u*, and ^{241}P*u*. *Phys. Rev. C*, 33(3):943, 1986. URL `https://doi.org/10.1103/PhysRevC.33.943`.

[97] P. Jesinger *et al.* Angular correlations in ternary fission induced by polarized neutrons. *Physics of Atomic Nuclei,*, 65(4):630, 2002. URL `https://doi.org/10.1134/1.1471264`.

[98] P. Dhondt *et al.* Energy distributions and absolute yields of the charged light particles emitted during the thermal neutron induced ternary fission of ^{235}U. *Nucl. Phys. A*, 346 (3):461, 1980. URL `https://doi.org/10.1016/0375-9474(80)90480-7`.

[99] C. Guet *et al.* A detailed investigation of the thermal neutron induced ternary fission of ^{235}U. *Nucl. Phys. A*, 314(1):1, 1979. URL `https://doi.org/10.1016/0375-9474(79)90551-7`.

[100] G. Rémy *et al.* Cross sections for binary and ternary fission induced by high-energy protons in uranium and lead. *Nucl. Phys. A*, 163(2):583, 1971. URL `https://doi.org/10.1016/0375-9474(71)90511-2`.

[101] H.W. Schmitt *et al.* Mass distribution and kinetics of U^{235} thermal-neutron-induced three-particle fission. *Phys. Rev. Lett.*, 9(10):427, 1962. URL `https://doi.org/10.1103/PhysRevLett.9.427`.

[102] S.A. Karamyan *et al. Sov. J. Nucl. Phys.*, 5:559, 1967.

[103] E.M. Kozulin *et al.* The CORSET Time-of-Flight spectrometer for measuring binary products of nuclear reactions. *Instrum. Exp. Tech.*, 51(1):44 – 58, 2008. URL `https://doi.org/10.1134/S0020441208010041`.

[104] C. Budtz-Jorgensen, H.-H. Knitter, Ch. Straede, F.-J. Hambsch, and R. Vogt. A twin ionization chamber for fission fragment detection. *Nucl. Phys. A*, 258(2):209 – 220, 1987. URL `https://doi.org/10.1016/0168-9002(87)90058-1`.

[105] F. Gönnenwein. Recent developments of experimental techniques. *Nucl. Phys. A*, 502:159, 1989. URL `https://doi.org/10.1016/0375-9474(89)90660-X`.

[106] W. Starzecki, A.M. Stefanini, S. Lunardi, and S. Signorini. A compact time-zero detector for mass identification of heavy ions. *Nucl. Instrum. Methods Phys. Res.*, 193(3):499, 1982. URL `https://doi.org/10.1016/0029-554X(82)90242-7`.

[107] S.E. Sobottka and M.B. Williams. Delay line readout of microchannel plates. *IEEE Trans. Nucl. Sci.*, 35(1):348, 1988. URL `https://doi.org/10.1109/23.12740`.

[108] M. Marouli *et al.* Direct measurement of alpha emission probabilities in the decay of ^{226}*ra. Applied Radiation and Isotopes*, 125:196, 2017. URL `https://doi.org/10.1016/j.apradiso.2017.04.029`.

[109] E.M. Kozulin *et al.* Mass distributions of the system $^{136}\mathrm{X}e$ + $^{208}\mathrm{P}b$ at laboratory energies around the coulomb barrier: A candidate reaction for the production of neutron-rich nuclei at N = 126. *Phys. Rev. C*, 86:044611, 2012. URL `https://doi.org/10.1103/PhysRevC.86.044611`.

[110] V.E. Viola, K. Kwiatkowski, and M. Walker. Systematics of fission fragment total kinetic energy release. *Phys. Rev. C*, 31(4):1550, 1985. URL `https://doi.org/10.1103/PhysRevC.31.1550`.

[111] G. Prete *et al.* The 8πlp project at lnl. a detection system for light charged particles with deexcitation channel selection. *Nucl. Inst. Meth. in Phys. Res. A*, 422:263, 1999. URL `https://doi.org/10.1016/S0168-9002(98)00954-1`.

[112] P.A. Assimakopoulos. Kinematics of three body reaction. *Computer Physics Communicatons*, 10(6):385, 1975. URL `https://doi.org/10.1016/0010-4655(75)90042-9`.

[113] M. Wang *et al.* The AME2012 atomic mass evaluation. *Chinese Physics C*, 36(12):1603, 2012. URL `https://doi.org/10.1088/1674-1137/36/12/003`.

Scientific activities and products during the PhD training

International publications

E. Vardaci, P. N. Nadtochy, A. di. Nitto, A. Brondi, G. La rana, R. Moro, P. K. Rath, **M. Ashaduzzaman** *et.al.*, *Fission Dynamics of intermediate-fissility systems: A study within a stochastic three-dimensional approach*, Phys. Rev. C **92**, 034610 (2015). DOI: 10.1103/PhysRevC.92.034610

P.K. Rath, **M. Ashaduzzaman** *et.al.*, *Cluster structure effect of projectile in* $^7Li +^{208} Pb$ *reaction*, 11^{th}, IOP Conf. Series: Journal of Physics: Conf. Series **863**, 012030 (2017). DOI: 10.1088/1742-6596/863/1/012030

P.K. Rath, E. Vardaci *et.al.*, *Breakup phenomena study in* $^7Li +^{208} Pb$ *reaction using 8PLP*, 11^{th}, EPJ Web of Conf. **86**, 00037 (2015). DOI: 10.1051/epjconf/20158600037

I.M. Harca, E. Kozulin, E. Vardaci, **M. Ashaduzzaman** *et.al.* *The Reaction* $^{34}S + {}^{197}Au$ *near the interaction barrier*, Proceedings of the International Symposium on Exotic Nuclei EXON-2016, Kazan, Russia, 4 - 10 September 2016, World Scientific Publishing- Exotic Nuclei: pp. 236-242 (2017). DOI: 10.1142/9789813226548_0035

E. Vardaci, A. Di Nitto, P.N. Nadtochy, G. La Rana, M. Cinausero, G. Prete, N. Gelli, E. M.Kozulin, G.N. Knyazheva, I.M. Itkis, **M. Ashaduzzaman** *et.al.*, Is nuclear viscosity dependent on temperature?, 6th Workshop on Nuclear Fission and Spectroscopy of Neutron Rich Nuclei, 20-24 March 2017, Chamrousse, France.

P.K. Rath, E. Vardaci, L. Campajola, G. Larana, **M. Ashaduzzaman**, *Development of the beam line for n production using* $D(d,n)^3He$, Proceedings of the DAE-BRNS Symp. on Nucl. Phys. **60**, 938 (2015).

E. Vardaci, L. Campajola, P.K. Rath, G. Larana, **M. Ashaduzzaman** *et.al.*, *PRIN - A Facility for neutron production using Accelerator*, Proceedings of the DAE-BRNS Symp. on Nucl. Phys. **61**, 952 (2016).

P.K. Rath, E. Vardaci, **M. Ashaduzzaman**, *Projectile break-up mechanism in* $^7Li+^{208}Pb$ *reaction around the Coulomb barrier*, Proceedings of the DAE-BRNS Symp. on Nucl. Phys. **61**, 350 (2016). .

Poster Presentations

1. **M. Ashaduzzaman**, *Three body decay in* $^{238}U+^{238}U$ *using CORSET*, Euroschool on Exotic Beams, 30 August - 5 September 2015, Dubrovnik, Croatia.
2. **M. Ashaduzzaman**, *Clustering effect in ternary fission of heavy and Superheavy Nuclear Systems*, Terzo Incontro Nazionale di Fisica Nucleare INFN2016, 14 - 16 November, 2016, Laboratori Nazionali di Frascati, Rome, Italy.
3. P. K. Rath, E. Vardaci, L. Campajola, F. Di Capua, G. La Rana, **M. Ashaduzzaman**, D. Quero, B. De Canditiis, *A beam line for production of a neutron beam using* $D(d,n)^3He$ *reaction at the 3 MV Tandem accelerator*, Terzo Incontro Nazionale di Fisica Nucleare INFN2016, 14 - 16 November, 2016, Laboratori Nazionali di Frascati, Rome, Italy.

Oral Presentations

1. **M. Ashaduzzaman**, *Three body decay in* $^{238}U+^{238}U$ *using CORSET*, Euroschool on Exotic Beams, 30 August - 5 September 2015, Dubrovnik, Croatia.
2. **M. Ashaduzzaman**, *Ternary Fission of Superheavy Nuclear Systems*, National Conference on Physics - 2017, 05 - 07 January, 2017, Atomic Energy Centre, Dhaka, Bangladesh.

Attended Nuclear Experiments

1. Study of three body clusterizations of Superheavy Nuclear systems. 28 - 29 May, 2015, GANIL, Caen, France.

2. TANDEM-ALPI-PIAVE ACCELERATOR: Investigation of decay modes of Argon isotopes formed in fusion-evaporation reactions, GARFIELD + RCo. 27 November - 05 December, 2015, Laboratori Nazionali di Legnaro, Legnaro, Padova, Italy.

3. The study of shape coexistence for Hg isotopes through a average lifetime using GALILEO + Plunger + EUCLIDES. 17 - 24 March, 2016, Laboratori Nazionali di Legnaro, Legnaro, Padova, Italy.

4. Prompt γ-rays as a probe of nuclear dynamics. 27 June - 4 July, 2016, Institut de Physique Nucleaire d'Orsay, 91406 Orsay, France.

5. Study of the ternary decay channel induced by shell effects via the reactions ^{34}S + ^{208}Pb and ^{37}Cl + ^{205}Tl. 22 - 30 June, 2017, Department of Physics, University of Jyv$\ddot{a}$skyl$\ddot{a}$, Finland.

Professional Training:

Scientific Schools

1. Euroschool on Exotic Beams, 30 August - 5 September 2015, Dubrovnik, Croatia.

2. 3rd International Geant4 and GPU Programming School, 9 - 13 November 2015, Catania, Italy.

Conferences

1. 11th International Conference on Clustering Aspects of Nuclear Structure and Dynamics, 23 - 27 May, 2016, Napoli, Italy.

2. Terzo Incontro Nazionale di Fisica Nucleare INFN2016, 14 - 16 November, 2016, Laboratori Nazionali di Frascati, Rome, Italy.

3. National Conference on Physics - 2017, 05 - 07 January, 2017, Atomic Energy Centre, Dhaka, Bangladesh.

Workshops, Seminars & Meetings

1. Active Target and Time Projection chamber (ACTAR TPC) Collaboration Workshop, 18 - 20 November, 2015, GANIL, Caen, France.

2. 5th Series of Majorana Lectures, by J.W. Gibbs (Yale University, USA), 14 - 16 March, 2016, University of Naples Federico II, Napoli, Italy.
3. Collaboration meeting about ^{238}U+^{238}U experiment, 16 - 20 November, 2015, GANIL, Caen, France.

Membership

1. Member of Local Organizing Committee, 11th International Conference on Clustering Aspects of Nuclear Structure and Dynamics, 23 - 27 May, 2016, Napoli, Italy. IOP Conf. Series: Journal of Physics: Conf. Series **863**, 011002 (2017) DOI: 10.1088/1742-6596/863/1/011002